INFORMATION TO USERS

UNIVERSITY OF CALIFORNIA
Santa Barbara

Current Injection in
Semi-Insulating Indium Phosphide

A dissertation submitted in partial satisfaction
of the requirements of the degree of

Doctor of Philosophy

in

Electrical and Computer Engineering

by

Patricia J. Corvini

Committee:
   Professor John E. Bowers, chairman
   Professor Larry A. Coldren
   Professor Arthur C. Gossard
   Professor Herbert Kroemer

November 1995

UMI Number: 9617646

Copyright 1995 by
Corvini, Patricia J.
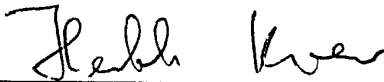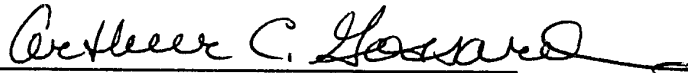
The dissertation of Patricia J. Corvini
is approved:
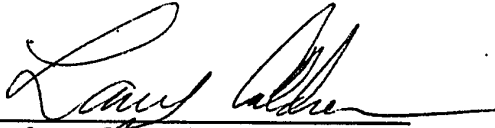
_____
Professor Herbert Kroemer
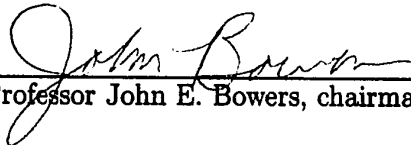
_____
Professor Arthur C. Gossard

_____
Professor Larry A. Coldren

_____
Professor John E. Bowers, chairman

December 1995

ii

Current Injection in
Semi-Insulating Indium Phosphide

Department of Electrical and Computer Engineering
University of California, Santa Barbara
Santa Barbara, California 93106

Acknowledgements

iv

To the memory of

Edmund J. Corvini
1913 – 1991

and

Rudolph L. Corvini
1914 – 1993

Vita

1958   Born 14 September at Ithaca, New York

1978–1980   Electronics technician
Department of Mechanical and Aerospace Engineering
Princeton University, Princeton, New Jersey

1983   B.S.E., Electrical Engineering and Computer Science
Princeton University

1983–1988   Senior Technical Associate, Member of Technical Staff
Electrophotonics Research Department
AT&T Bell Laboratories, Holmdel, New Jersey

1988   M.S., Materials Science
Stevens Institute of Technology, Hoboken, New Jersey

1990–1995   Research assistant
Department of Electrical and Computer Engineering
University of California, Santa Barbara

1995   Ph.D., Electrical and Computer Engineering
University of California, Santa Barbara

Publications

1. P. Corvini, A. Kahn, and S. Wagner, "Surface order and stoichiometry of sputter-cleaned and annealed $CuInSe_2$," *J. Appl. Phys.* 57, 2967 (1985).

2. A. Kahn, P. Corvini, S. Wagner, and K. J. Bachmann, "First investigation of the atomic structure of (112) and ($\overline{112}$) $CuInSe_2$ surfaces," *Solar Cells* 16, 123 (1986).

3. T. L. Koch, L. A. Coldren, T. J. Bridges, E. G. Burkhardt, P. J. Corvini, and D. P. Wilt, "1.55 μm high speed vapor phase transported buried heterostructure lasers (VPTBH)," *Electron. Lett.* 20, 856 (1984).

4. T. L. Koch, L. A. Coldren, T. J. Bridges, E. G. Burkhardt, P. J. Corvini, and D. P. Wilt, "1.5 μm monolithic shallow-groove coupled-cavity vapor phase transported buried heterostructure lasers," *Electron. Lett.* 20, 1001 (1984).

5. T. L. Koch, T. J. Bridges, E. G. Burkhardt, R. A. Logan, L. F. Johnson, R. F. Kazarinov, R. T. Yen, L. A. Coldren, P. J. Corvini, R. A. Linke, and W. T. Tsang, "1.55 μm InGaAsP distributed feedback vapor phase transported buried heterostructure lasers," *Appl. Phys. Lett.* 47, 12 (1985)

6. T. L. Koch and P. J. Corvini, "Studies of high-bit-rate dispersive optical fiber transmission using single-frequency lasers," paper TUF-3, Conference on Optical Fiber Communication, Atlanta, 1986.

7. P. J. Corvini and T. L. Koch, "Computer simulation of high-bit-rate optical fiber transmission using single frequency lasers," *IEEE J. Lightwave Tech.* LT-5, 1591 (1987).

8. P. J. Corvini and T. L. Koch, "Asymmetry of calculated chirp-induced dispersion penalty for wavelength variations about 1.3 μm," unpublished (1987).

9. T. L. Koch and P. J. Corvini, "Semiconductor laser chirping-induced dispersive distortion in high-bit-rate optical fiber communications systems," summary for invited talk at ICC '88, Philadelphia. In: IEEE International Conference on Communications '88: Digital Technology— Spanning the Universe. Conference Record, vol. 2, p. 584; IEEE, New York, 1988.

10. T. L. Koch, P. J. Corvini, G. D. Boyd, M. A. Duguay, and W. T. Tsang, "Line-narrowed 1.55 μm VPT-DFB lasers using vertically self-aligned Si-SiO$_2$ ARROW cavities," paper I-4, Tenth IEEE International Semiconductor Laser Conference, Kanazawa, Japan, 1986.

11. T. L. Koch, U. Koren, G. D. Boyd, P. J. Corvini, and M. A. Duguay, "Anti-resonant reflecting optical waveguides for III-V integrated optics," *Electron. Lett.* 23, 244 (1987).

12. T. L. Koch, W. T. Tsang, and P. J. Corvini, "Spectral dependence of propagation loss in InP/InGaAsP anti-resonant reflecting optical waveguides grown by chemical beam epitaxy," *Appl. Phys. Lett.* 50, 307 (1987).

13. T. L. Koch, E. G. Burkhardt, F. G. Storz, T. Sizer, W. T. Tsang, U. Koren, and P. J. Corvini, "Interlayer directionally grating-coupled ARROW structures for III-V integrated optoelectronics," paper TUC1, Topical Meeting on Semiconductor Lasers, Albuquerque, 1987.

14. T. L. Koch, P. J. Corvini, W. T. Tsang, U. Koren, and B. I. Miller, "Wavelength-selective interlayer-directionally grating-coupled InP/ InGaAsP waveguide photodetection," *Appl. Phys. Lett.* 51, 1060 (1987).

15. P. J. Corvini, L. Eichner, and A. B. Piccirilli, "HBr:HNO₃:H₂O etching characteristics for holographic gratings," unpublished (1986).

16. T. L. Koch, P. J. Corvini, and W. T. Tsang, "Anisotropically etched deep gratings for InP/InGaAsP optical devices," *J. Appl. Phys.* 62, 3461 (1987).

17. B. I. Miller, U. Koren, and P. J. Corvini, "InGaAs/InP quantum boxes and wires through use of atmospheric OMVPE and holographic photolithography," poster paper 1-17, Third International Conference on Superlattices, Microstructures & Microdevices, Chicago, 1987.

18. B. I. Miller, A. Shahar, U. Koren, and P. J. Corvini, "Quantum wires in InGaAs/InP fabricated by holographic photolithography," *Appl. Phys. Lett.* 54, 188 (1989).

19. U. Koren, T. L. Koch, P. J. Corvini, B. I. Miller, G. Eisenstein, R. S. Tucker, Y. K. Su, and R. J. Capik, "High power high speed single mode SIPBH-DFB lasers at 1.3 micron," *J. Appl. Phys.* 64, 4785 (1988).

20. G. Eisenstein, U. Koren, A. H. Gnauck, T. L. Koch, R. S. Tucker, P. J. Corvini, B. I. Miller, and Y. K. Su, "Spectral and modulation properties of 1.3-μm SIPBH DFB lasers," *Appl. Phys. Lett.* 53, 1905 (1988).

21. T. L. Koch, P. J. Corvini, U. Koren, and W. T. Tsang, "Wavelength uniformity of 1.3 μm GaInAsP/InP distributed Bragg reflector lasers with hybrid beam/vapour epitaxial growth," *Electron. Lett.* 24, 822 (1988).

22. F. S. Choa, W. T. Tsang, R. A. Logan, R. P. Gnall, U. Koren, T. L. Koch, C. A. Burrus, M. C. Wu, Y. K. Chen, P. F. Sciortino, A. M. Sergent, and P. J. Corvini, "Very high sidemode-suppression-ratio distributed-Bragg-reflector lasers grown by chemical beam epitaxy," *Electron. Lett.* 28, 1001 (1992).

23. P. J. Corvini, M. M. Hashemi, S. P. DenBaars, and J. E. Bowers, "Fe-doped semi-insulating InP grown by atmospheric pressure MOCVD using tertiarybutylphosphine, trimethylindium, and ferrocene," paper P4, Electronic Materials Conference, Boston, 1992.

24. M. P. Mack, C. M. Reaves, P. J. Corvini, S. P. DenBaars, M. S. Leonard, M. Mondry, and J. L. Merz, "Growth of high quality $In_xGa_{1-x}As/InP$ quantum wells with tertiarybutylarsine and tertiarybutylphosphine," paper J2, Electronic Materials Conference, Boston, 1992.

25. M. M. Hashemi, J. B. Shealy, P. J. Corvini, S. P. DenBaars, and U. K. Mishra, "High performance InP JFETs grown by metalorganic chemical vapor deposition using tertiarybutylphosphine (TBP) as the phosphorus source," *J. Electron. Mat.* 23, 233 (1994).

26. P. J. Corvini and J. E. Bowers, "Avalanche breakdown in semi-insulating Fe:InP," post-deadline paper PDB3, Sixth International Conference on Indium Phosphide and Related Materials, Santa Barbara, 1994.

27. P. J. Corvini and J. E. Bowers, "Modeling of DC current injection in semi-insulating Fe:InP," ARPA Optoelectronics Technology Center external seminar, San Diego, 1995.

Abstract

Current Injection in
Semi-Insulating Indium Phosphide

by
Patricia J. Corvini

Steady-state current injection in planar n-SI-n Fe:InP is modeled both numerically and with the simplified theory of Lampert and Mark. The predicted I-V characteristics for various layer thicknesses are compared with experimental results from material grown by non-hydride metalorganic chemical vapor deposition (MOCVD).

The simplified theory, which is based on electron drift only, fails to explain several of the observed phenomena—most notably a destructive breakdown at voltages below the trap-filled limit. The two-carrier numerical model can predict these phenomena, by allowing the inclusion of such processes as carrier diffusion, impact ionization, recombination through traps, field emission from traps, and nonlinear velocity-field relations. The mechanisms are added to the model one at a time, so as to clarify the effect of each on the progress of trap filling and on the I-V characteristics.

For comparison of theories with experiment, we define a critical voltage as that at which the current reaches 1 A/cm^2, which would be an appropriate performance criterion for current blocking in many lasers. Critical voltages predicted by the numerical model are significantly lower than those of the simplified theory at both ends of the thickness range, and are in good agreement with the experimental results. Performance is dominated by carrier diffusion at the interfaces in the case of thin layers and low trap densities, and by avalanche injection in the case of thick layers and high trap densities. In the latter case, a positive feedback mechanism accounts for the experimentally observed destructive breakdown.

Current Injection
in
Semi-Insulating
Indium Phosphide

Contents

Symbols and abbreviations

With the exception of B, C, D, G, R, and v as noted below, the following symbols are used consistently throughout this work to designate the quantities indicated:

L	thickness of SI layer
x	position (z in Appendix E)
q	electron charge (magnitude)
m_0	free electron mass
m_e	effective mass, electrons
m_h	density-of-states effective mass, holes
N_C	effective density of states, conduction band
N_V	effective density of states, valence band
ϵ	permittivity
k	Boltzmann constant
T	temperature
ξ_C, ξ_V	conduction and valence band edges
ξ_F	Fermi level
ξ_{Fn}	electron quasi-Fermi level
ξ_t	trap level
ξ_a	ionization energy, $\xi_C - \xi_t$
g	degeneracy factor for trap
ψ	electrostatic potential
E	electric field
R	net SRH recombination rate†
G	generation rate by impact ionization†
J_n, J_p, J	electron, hole, total current densities
D_n, D_p	electron, hole diffusivities†
μ_n, μ_p	electron, hole mobilities (field-dependent)
μ_{no}, μ_{po}	low-field electron & hole mobilities (constant)

v_n, v_p	electron, hole velocities†
v_{sn}, v_{sp}	electron, hole saturation velocities†
v_{th_n}, v_{th_p}	electron, hole thermal velocities†
σ_{cn}, σ_{cp}	electron, hole capture cross sections
e_n, e_p	electron, hole emission probabilities
τ_{n0}, τ_{p0}	background SRH time constants
α_n, α_p	band-to-band impact ionization coefficients
B	radiative recombination coefficient†
V_X	ohmic-to-SCL crossover voltage
V_{TFL}	trap-filled-limited voltage
V_{cr}	critical voltage
C	capacitance (per unit area)
Q	charge (per unit area)
θ	n/n_t (see §3.1)
χ	SCL-current prefactor (see §3.1)

CONCENTRATIONS:

N_t	total traps (deep acceptors)
N_d	fully-ionized donors
n, p	free electrons, holes
n_0	thermal free electrons
n_t	trapped electrons (filled traps)
n_{t_0}	filled traps at equilibrium
p_{t_0}	empty traps at equilibrium
n_i	intrinsic carrier concentration
n_1	free electrons when $\xi_F = \xi_t$
p_1	holes when $\xi_F = \xi_t$ ($p_1 = n_i^2/n_1$)

Additional symbols are defined in the text as needed. These should be considered as "local" to the discussions in which they occur. For example, we hope that no ambiguity arises from the momentary use of the symbol E_0 to designate a scaling field in Appendix C, when we have already used the constants E_{0n} and E_{0p} to describe the field dependence of the impact ionization coefficients in Chapter 5 and E_0 to describe the velocity-field relation

in Chapter 4. Similarly:

†The B, C, D, G, R, and v used in Appendix C are in the notation of Lampert and Mark [1] and bear no relation to any B, C, D, G, R, and v used elsewhere in the present document. While we thus occasionally re-use a symbol, we have taken care that any given physical quantity is represented by a single symbol throughout this work. In particular, we use n_1 to designate the quantity that Lampert and Mark call N, and g for the quantity that Lampert and Mark would call $1/g$.

ABBREVIATIONS:

SI	semi-insulating
SCL	space-charge-limited
TFL	trap-filled-limited
NDR	negative differential resistance
SRH	Shockley-Read-Hall
I-V	current-voltage
J-V	current(density)-voltage
C-V	capacitance-voltage
DLTS	deep level transient spectroscopy
FTIR	Fourier transform infrared
ESR	electron spin resonance
SIMS	secondary ion mass spectroscopy
VPE	vapor-phase epitaxy
MOCVD	metalorganic chemical vapor deposition
CBE	chemical beam epitaxy
APD	avalanche photodiode

Chapter 1

Introduction

Resistors are often pictured as linear circuit elements obeying Ohm's Law. This dissertation is about the I-V characteristics of a resistor that should not be pictured this way.

The resistor described here is a planar layer of InP made semi-insulating by being intentionally doped with iron. This technologically important resistor exhibits highly nonlinear behavior, some of which cannot be explained by the theory that has traditionally been applied.

A semi-insulating Fe:InP layer typically exhibits a regime of very high resistance followed at larger biases by a rapid rise in current as a function of voltage. (An I-V characteristic for such a layer is shown in Figure 1.1.) The high resistance is a result of deep acceptors that lower the thermal carrier concentration and also trap injected electrons, creating a negative space charge that opposes further electron injection. The rapid rise in current is normally attributed to the filling of these deep acceptor traps. Space-charge-limited current flow and trap filling by injected electrons have been well described by Lampert and Mark [1], and it is their approach that has traditionally been applied to the analysis of Fe:InP.

We find, however, that this approach fails to explain our experimental results. While the rapid rise in current predicted by the traditional theory is smooth and reversible, we also observe an abrupt and destructive breakdown, which has not been previously reported in Fe:InP and which we attribute to avalanche injection of holes. In this case, the rapid increase in current occurs while most of the traps are still empty—and therefore at much lower voltages than the traditional theory would predict. The catastrophic nature of this breakdown and the comparatively low voltages at which it occurs make it a serious concern for device design. The present work develops a model
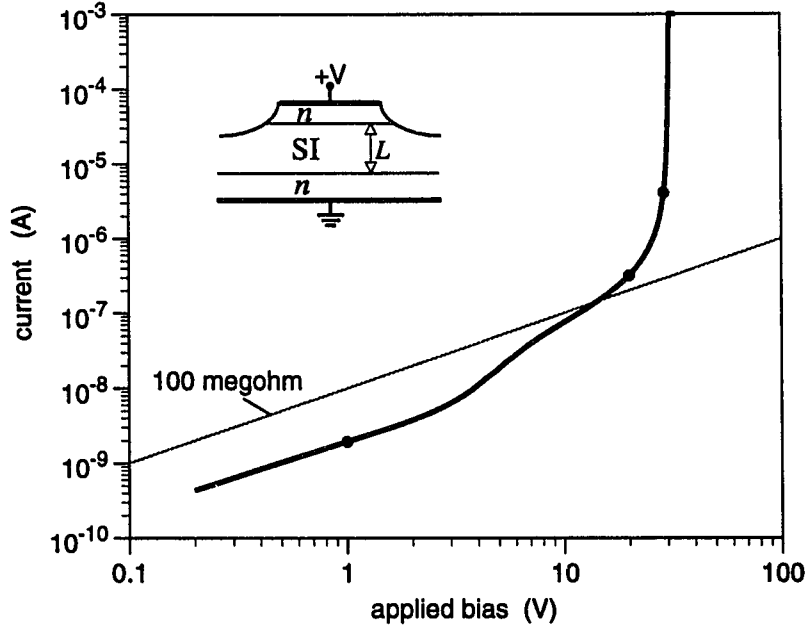
Figure 1.1:   Typical *I-V* curve for Fe:InP under electron injection from *n*-contact.   Sample is a planar *n*-SI-*n* structure as shown in inset, grown by non-hydride MOCVD under conditions listed in Chapter 6. The SI layer is 3.6 μm thick, with a 90-μm-diameter top contact. Current was externally limited to 1 mA. Resistivity, defined as $(A/L)(V/I)$ where A is the contact area and L the thickness of the SI layer, is 10^8 Ω-cm at 1 V, 10^7 Ω-cm at 20 V, and 10^6 Ω-cm at 29 V (points marked by dots.) The *I-V* curve for an ideal 100-MΩ resistor is shown for comparison.

that allows us to predict both the nature of the rapid rise in current and the voltage at which it occurs. In the course of developing this model, we examine the contributions of several physical mechanisms to the current-voltage characteristics of Fe:InP.

Semi-insulating (SI) Fe:InP is used for current blocking in numerous optoelectronic devices, including lasers, detectors, and modulators. In these applications, it provides current confinement as well as good thermal conductivity, reduced surface leakage, and favorable waveguiding properties.

Typical examples are the in-plane lasers shown in Figure 1.2. In these structures, Fe:InP layers provide a high-resistance path that allows for a broad-

(a)

(b)
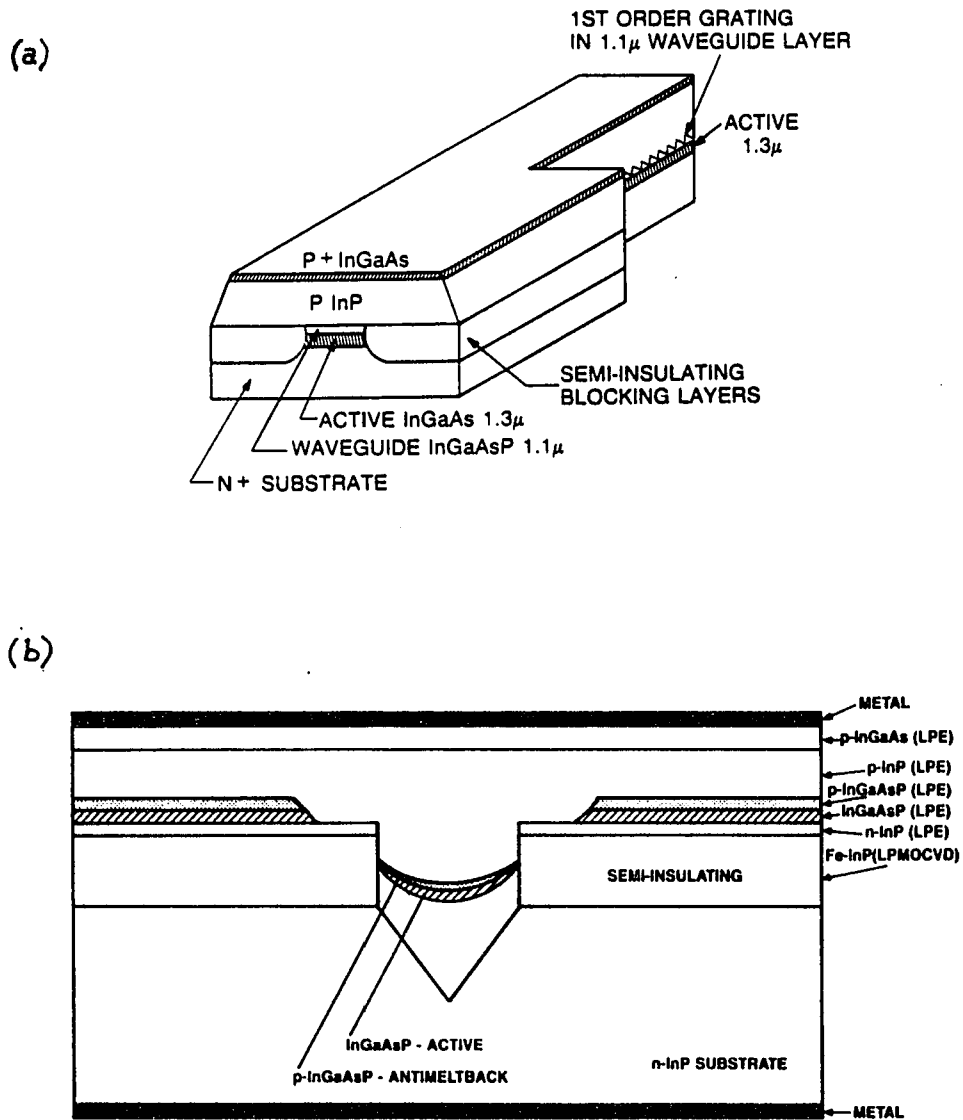
Figure 1.2: Lateral cross-section of in-plane laser structures using Fe:InP blocking layers: (a) SIPBH (semi-insulating blocked planar buried heterostructure) [2]; (b) buried crescent [3].
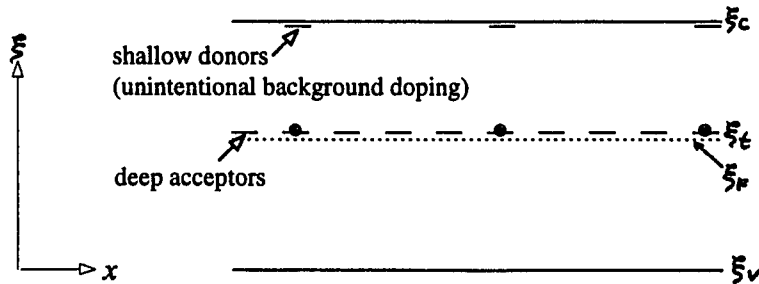
Figure 1.3:   Band diagram for bulk Fe:InP at thermal equilibrium.

area top contact while confining current to the active region.

SI Fe:InP has also been used successfully in electron devices, such as field-effect transistors [4], and is the basis of inter-device isolation for InP-based electronic and optoelectronic integrated circuits.

All of these applications rely on the ability of the semi-insulating material to maintain a high resistance over some range of biasing conditions. Because the resistance of an Fe:InP layer is strongly dependent on the biasing conditions, an understanding of the electrical behavior of this material is essential for device and circuit design.

In a simple resistor obeying Ohm's Law, the number of carriers is constant, i.e. unaffected by the applied bias. The carriers are all free to move, and they drift in the applied field.

In semi-insulating InP, the situation is more complicated. The number of carriers is not constant, and the carriers are not all free to move.

The semi-insulating nature of Fe:InP is due to a deep acceptor. This deep acceptor compensates the usual n-type background, so that for a bulk sample at thermal equilibrium the Fermi level is near the center of the bandgap, as illustrated in Figure 1.3. This means that the thermal carrier concentrations are small, and the resistance is high.

Under an applied bias, however, extra carriers can enter the semi-insulating material. Because the thermal carrier concentrations are so low, only a small applied bias is needed to substantially increase the carrier concentrations. The added carriers result in a decrease in the resistance.

If the added carriers are electrons, initially most of them are trapped by unoccupied acceptors—that is, localized in the vicinity of Fe atoms—so that the increase in the free carrier concentration under bias is much smaller than it would be in an intrinsic material. The trapped electrons contribute a negative

space charge that influences the field in which the free carriers drift. When the traps fill up, the current rises rapidly and the layer behaves as if it were composed of intrinsic material.

The processes we have just described are those that are included in the traditional analysis, that is, in the well-known "simplified theory" of Lampert and Mark [1]. This theory describes current injection in trap-controlled insulators under the assumption that single-carrier drift is the dominant transport mechanism and that carrier generation/recombination in the semi-insulating material can be neglected. This approach provides an excellent framework for thinking about the problem, but fails to adequately predict the behavior of Fe:InP for device applications.

For design, we want to know at what voltage the current through the SI layer will exceed that which is acceptable for our device, and we want to know how to design the layer so as to maximize this "critical" voltage. In the simplified theory, the critical voltage is attributed solely to filling of the traps by injected electrons, and is therefore a simple function of the layer thickness and of the initial concentration of empty traps. Experimental results suggest that something else is going on. In the present work, we demonstrate that both diffusion of carriers from adjacent n-layers and generation of electron-hole pairs by impact ionization in the SI layer strongly affect the critical voltage. In the presence of impact ionization, phenomena that would otherwise not affect the critical voltage—such as nonlinear velocity-field relations and Shockley-Read-Hall generation/recombination—also become significant.

Since none of these additional phenomena can readily be treated analytically, in this work we develop a numerical model and use it to explore the effects of mechanisms that are ignored by the simplified theory. As noted above, we find that some of these are very important for Fe:InP, so that the numerical model provides a more accurate description of the material's behavior. We retain the philosophy of the simplified approach, however, in keeping the problem as simple as possible at each stage, so as to isolate and thereby understand the effects of each mechanism.

For this reason, we focus on the one-dimensional steady-state problem. The insights gained from this case can then be applied to more complex geometries and to the time-dependent problem, and can be used as a basis for the study of other physics.

We also restrict our attention to n-SI-n structures. Because Fe in InP is an acceptor and an electron trap [5], Fe:InP is not well suited to blocking hole

current. Additionally, interdiffusion of Fe with p-dopants has been a problem [6]. To prevent hole injection or dopant interdiffusion, an n-layer is commonly inserted between Fe:InP and any neighboring p-layers (see Figure 1.2). The n-SI-n structure is thus of great technological significance, and the prediction of current-voltage (I-V) characteristics for n-SI-n InP is of value for device design as well as for material characterization.

Previous work. Iron-doped InP has been under investigation for twenty years. The material has been prepared by ion implantation [7] and in bulk as well as by vapor-phase epitaxy (VPE) [8], metalorganic chemical vapor deposition (MOCVD) [9, 10, 11], non-hydride MOCVD [12, 13], and chemical beam epitaxy (CBE) [14], and has been analyzed by a wide variety of techniques. Of particular interest for the present work are studies concerning the nature of the Fe impurity in InP and its contribution to the semi-insulating behavior of the material.

Electron spin resonance (ESR) data [5, 15] have established that Fe in InP occurs as a substitutional impurity on Group III sites. The free atom has electronic configuration $3d^6 4s^2$; on an In site, three of these electrons participate in bonding, leaving a $3d^5$ (Fe^{3+}) configuration for the neutral center. The substitutional Fe acts as a deep acceptor, capable of trapping a single electron to form a $3d^6$.(Fe^{2+}) ionized configuration. It is this property which is responsible for the semi-insulating nature of Fe:InP.

There is a wealth of spectroscopic data regarding internal transitions of the occupied acceptor Fe^{2+}, which exhibits excited states in the bandgap [15, 16, 17, 18]. Internal transitions of the neutral acceptor Fe^{3+} have been reported as well [19]. Crystal field theory has been applied to the calculation of the positions of the various levels [15, 18, 20].

The electrical properties of SI Fe:InP have also been widely studied. I-V characteristics of n-SI-n InP have been measured and analyzed by Cheng et al. [7] and Sugawara et al. [21], among others.

Because SI Fe:InP is a trap-controlled insulator, much of its behavior can be understood in the framework of existing theory. As we indicated above, the general problem of current injection in insulators has been thoroughly analyzed by Lampert and Mark [1]. Their approach emphasizes analytic solution through simplification of the problem, and yields simple expressions describing the I-V characteristics. These results have frequently been applied to the interpretation of measurements made on Fe:InP [7, 21].

It has also been recognized that mechanisms other than simple trap fill-

ing may be responsible for some of the observed behavior of Fe:InP. Kitagawa *et al.* [22] have described surface breakdown by a mechanism similar to that which we propose for the bulk. Turki *et al.* [23] have proposed a field-dependent trapping mechanism to explain their results.

Current injection in SI InP has been analyzed by numerical techniques as well. The general problem of numerical analysis of semiconductor devices has been treated extensively. The approach used here—simultaneous solution of the Poisson and continuity equations by the method of finite differences—is discussed by, for example, Kurata [24] and Selberherr [25]. Asada *et al.* [26] used this method to analyze planar and two-dimensional current flow in several SI InP blocking structures, with a model that included recombination through the trap.

Similar numerical analyses have been carried out for other materials. The GaAs literature, in particular, treats many of the same issues that we address here. Both one-dimensional [27] and two-dimensional [28] geometries have been studied. The importance of bandbending at interfaces has been recognized [27], as has the importance of carrier generation by impact ionization [29, 30]. The nature of the traps is different in GaAs, however, so the GaAs results do not necessarily apply directly to Fe:InP.

Current instabilities in the presence of negative differential resistance of the type caused by impact ionization have also been studied [31].

This work. The emphasis in this work is on understanding the contribution of various physical processes to the electrical characteristics of n-SI-n InP structures, as a means to accurate prediction of those characteristics. To this end, we bring together several threads from the previous work. We draw on the basic studies of the nature of the trap and its energy levels to give us accurate parameters for use in the model. We explore the full implications of the simplified theory for a trap of this type, to show the basis of the problem in trap filling and electron drift.

Using standard solution techniques, we then develop a one-dimensional numerical model. This allows us to easily examine spatial variations of the electric field, carrier concentrations, trapped charge, etc., and thereby to gain more insight into the effects of various processes than would be provided by the terminal characteristics alone. By including them successively in the model, we show the separate effects (on trap filling and on the I-V characteristics) of carrier diffusion, nonlinear velocity-field relations, field emission from traps, Shockley-Read-Hall (SRH) recombination/generation, and carrier generation

by impact ionization.

We have already mentioned some experimental results as motivation for the present work. We also perform a series of experiments specifically to confirm the main predictions of our model. The focus here is on the critical behavior—that is, the regime in which the current rises steeply as a function of voltage—since this is important for device design. Our thesis is that several mechanisms can contribute to a steep rise in current, in addition to simple trap filling by injected carriers. In particular, we verify the importance of interface effects for thin layers and of avalanche injection for thicker layers. In the latter case we predict and observe destructive breakdown at voltages well below the trap-filled limit.

Overview of dissertation. In this introduction, we have argued for the value of an accurate model of one-dimensional, steady-state current injection in n-SI-n InP. The next chapter gives an overview of the models presented in this work, and shows in what ways they differ from each other and in what ways they are the same.

In Chapter 3 we present the simplified theory of Lampert and Mark, and apply this theory to Fe:InP. We extend the previous work in this area by showing the spatial distribution of occupied traps predicted by this model, as a function of bias level. A brief comparison with published experimental results indicates the inadequacy of the simplified theory for predicting the behavior of Fe:InP.

In Chapters 4 and 5 we present the numerical model for n-SI-n InP. Single-carrier effects are treated in Chapter 4, in which we demonstrate that diffusion from the n contacts dominates the behavior of thin SI layers.

Two-carrier effects are treated in Chapter 5. Here we show that, in the presence of carrier generation due to impact ionization, a positive feedback mechanism for avalanche breakdown results in lower breakdown voltages than a simpler theory might predict. We show that, in this situation, recombination through the traps also becomes important.

In Chapter 6 we compare the predictions of the simplified and numerical models with experiment, with particular emphasis on the critical behavior. We show that the numerical model gives better agreement, both as to the critical voltages and as to the manner of breakdown. Discrepancies with regard to the behavior below breakdown still remain, however.

In Chapter 7 we examine the sensitivity of the predicted critical voltage to several design and materials parameters for the SI layer. Together with the

experimental results, these calculations yield useful design rules.

Chapter 8 gives a summary of the results, with emphasis on the importance of various physical mechanisms in different regimes of trap density and layer thickness. We mention some implications of these results for device design, and propose further modeling and experimental work on Fe:InP. We also propose using the model to study other traps and other materials.

The values of various constants used in the calculations are given in Appendix A, together with a discussion of how some of them were chosen. This discussion draws on an occupation function derived in Appendix B. Appendices C and D present mathematical detail for the simplified theory and numerical model respectively. (The implementation of the numerical model has been relegated to a separate document.) Appendix E contains mathematical detail specific to the treatment of field emission in the numerical model. Appendix F presents a numerical calculation of the carrier concentrations in a p-n junction under reverse bias, which we find helpful for understanding the n-SI-n situation. Appendix G contains notes on the construction of the design curves shown in Chapters 7 and 8, and mentions a phenomenon we call "avalanche-assisted trap filling" which is not discussed elsewhere in the dissertation. (It is the opinion of the author that appendices do not necessarily comprise "dull stuff", but rather contain material that, while relevant and even interesting, does not belong to the main flow of the discussion.)

A list of symbols and abbreviations follows the table of contents.

Chapter 2

Overview of models

While applications aspects of this work emphasize prediction and verification of the critical behavior, one of the central aims of the dissertation is to present a comprehensive picture of steady-state current injection in Fe:InP, indicating the contributions due to various physical processes. To this end, an exposition of several different and successively more complicated models is presented in Chapters 3, 4, and 5. (Chapters 6, 7, and 8 compare some of the predictions with experiment, and show the implications of the theory for various design situations.)

All of these models are based on simultaneous solution of the Poisson and continuity equations, and all share certain assumptions about the nature of the trap, as well as other limitations. In this chapter, we give an overview of the various models, in order to make clear the relations among them. We first list the features common to all, then summarize the different approaches, and finally discuss the value and applicability of each.

2.1 Common features

The semi-insulating nature of Fe:InP is attributed to the presence of a partially ionized deep acceptor that acts as an electron trap and compensates the typical n-type background due to unintentional shallow donors. This deep acceptor trap promotes large resistivity at low bias by lowering the thermal carrier concentration, and blocks current at higher bias by trapping a negative charge which opposes further electron injection.

In all of the models discussed here, the deep acceptor is taken to be a single-electron trap characterized by an ionization energy $\xi_C - \xi_t$ and a de-

generacy factor g. (In the numerical model, we also allow for recombination through this trap, characterized by two cross sections.) When the acceptor is unoccupied, it is neutral with respect to the lattice; when occupied by an electron, it carries a charge $-q$. For the reason mentioned in the introduction, the neutral charge state is referred to as Fe^{3+} and the $-q$ charge state as Fe^{2+}. As also mentioned in the introduction, the Fe^{2+} configuration (that is, the occupied trap) exhibits excited states in the bandgap.

For a dynamic model, the nature of the transitions among the various states of the occupied trap, and the associated transition rates, would be important. For the steady-state situation, however, only the population of the various levels matters. In Appendix B, we derive an occupation function for a deep acceptor with excited states, and show that the effect of including the excited states is to produce a temperature-dependent change in the degeneracy factor for the acceptor level. (Our analysis assumes that the excited states affect the problem only through the occupation function; if the spatial extent of the excited states were large enough to promote tunneling between the traps, this would not be the case.)

The ionization energy $\xi_C - \xi_t$ (Figure 1.3) refers to the position of the lowest energy level of the occupied acceptor—that is, the one referred to in the literature [15, 18] as the Γ_1 level of the ^5E manifold. A number of experimental techniques have been used for the determination of this energy, with varying results. As discussed in Appendix A, we have scaled the 4.2-K value of Thonke and Pressel [18] to obtain $\xi_C - \xi_t = 0.59$ eV at room temperature.

The degeneracy factor g is the ratio of the degeneracy of the unoccupied (neutral, Fe^{3+}) state of the trap to that of its occupied (ionized, Fe^{2+}) state. For an acceptor, g enters the occupation function (that is, the probability f_t that the trap is occupied by an electron) as

$$f_t = \frac{1}{1 + g \exp[-(\xi_F - \xi_t)/kT]} \tag{2.1}$$

where the trap level ξ_t and the Fermi level ξ_F are counted positive with respect to some lower energy, such as the valence band edge. The value of g for Fe in InP has been variously taken as 4 [16], 1 [26, 32], and 2/5 [33]. Using the occupation function derived in Appendix B, a precise temperature-dependent degeneracy factor can be obtained if the degeneracies of the individual excited states of the occupied trap are known. On the assumption that the five ^5E levels of the Fe^{2+} configuration are all nondegenerate, and that the Fe^{3+} configuration carries a two-fold spin degeneracy, we calculate in Appendix A a

degeneracy factor $g = 0.45$ at room temperature.

We have carried g explicitly in our equations, rather than incorporating it as an equivalent shift in energy, so that the implications of using a different value (when a reliable number is available) can be clearly seen.

For the calculations shown in Chapters 3–5, we have assumed a background donor concentration N_d of 1×10^{15} cm^{-3}; for semi-insulating behavior, we assume that the concentration of deep traps is larger than this. For many of these calculations, we have assumed a trap concentration N_t of 8×10^{16} cm^{-3}, corresponding to the solubility limit of Fe in InP at a growth temperature of 650 °C [34]. (Epitaxial Fe:InP with approximately this trap concentration has been reported by Nakai *et al.* [11] and by Wolf *et al.* [34].) We also consider cases of smaller trap densities.) In all cases, we assume that the traps are uniformly distributed in space, that is, that N_t is constant across the SI layer. Values of other constants used are shown in Tables A.1–A.3 of Appendix A.

In all of the models discussed here, only the occupation of the trap level is treated with Fermi-Dirac statistics. Background donors are assumed to be fully ionized. Occupation of the conduction and valence bands is treated using Boltzmann statistics and an effective density of states. A single temperature describes the entire problem. (We have used $T = 300$ K.)

We assume that there is no hopping conduction or tunneling between traps, so that current flow is due to free carriers only. All of the models are one-dimensional and describe steady-state operation. (Because of the one-dimensionality, we use the term "*J-V*" rather than "*I-V*" to designate the current-voltage characteristics calculated in Chapters 3–5.)

2.2 Interrelation of models

Having said what all our models have in common, we now differentiate them from each other. The motivation for bothering with several different models is addressed in the next section; here we simply focus on what they are. That is, we here summarize the assumptions that define the various models, and introduce the terminology by which we will refer to them.

This section is intended as both introduction and roadmap to the discussion in Chapters 3–5. The reader may thus profit from returning to it during and after the reading of those chapters. On the other hand, the reader may agree with one distinguished commentator that this section is best skipped entirely. While Chapters 3–5 can indeed be read without Section 2.2, reading 2.2

will show the reader ahead of time how the various models fit together—which may be a great help in understanding any one of them.

The models fall into two categories, which we shall refer to as "simplified" and "numerical". Various degrees of sophistication are possible in both categories, but all of the models are based on simultaneous solution of the Poisson and continuity equations. In the simplified approach, we begin with these equations and then proceed to ignore various aspects of the physics (such as carrier diffusion and recombination), until the resulting problem can be solved analytically. In the numerical approach, we retain the exact equations, solve them numerically, and then proceed to add terms in order to describe more complicated physics. (The assumptions included in the various models are summarized in Table 2.1 on p. 16. Schematic band diagrams for the simplified and numerical problems, representing some of the main features of each, are compared in Figure 2.1.)

The mathematical formulation of the drift-diffusion problem is familiar. Therefore, in this section we state the general ("numerical") problem first, and then formulate the simplified theories in that context. The detailed discussion in Chapters 3, 4, and 5 follows roughly the opposite order, beginning with the simplest case and working though to the more complicated ones.

Numerical models. For our problem of a deep acceptor with a background of fully-ionized shallow donors, the Poisson equation for the electrostatic potential ψ is

$$\frac{\partial^2 \psi}{\partial x^2} = -\frac{q}{\epsilon}(N_d + p - n - n_t) \tag{2.2}$$

where n and p are the free carrier concentrations and $n_t = n_t(N_t, n, p \ldots)$ is the concentration of trapped electrons, or occupied deep acceptors. (A list of symbols follows the table of contents.) For the n-SI-n problem, we vary N_d and N_t as functions of position, to define the layer structure. Each of the carrier concentrations is also a function of position. The steady-state continuity equations are

$$\frac{\partial n}{\partial t} = \frac{1}{q}\frac{\partial J_n}{\partial x} - R + G = 0 \tag{2.3}$$

$$\frac{\partial p}{\partial t} = -\frac{1}{q}\frac{\partial J_p}{\partial x} - R + G = 0 \tag{2.4}$$
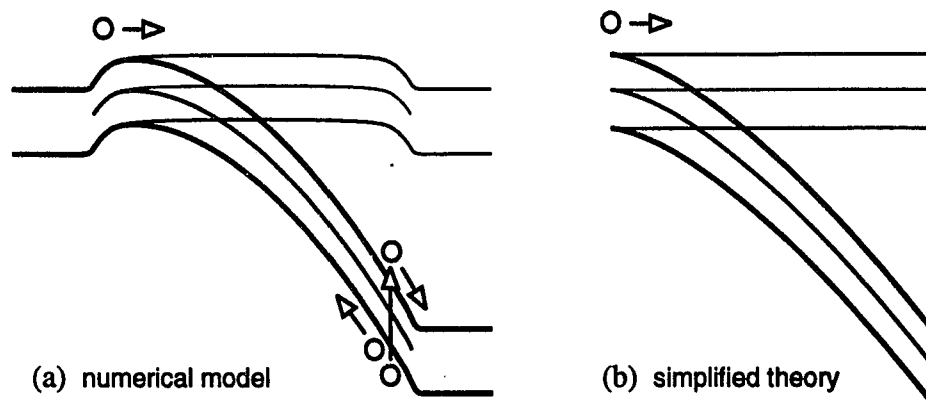
Figure 2.1: Schematic band diagrams for simplified and numerical models, showing injection mechanisms available in each. Drawings represent conduction & valence band edges and trap level as functions of position, with and without applied bias.

where the electron and hole current densities are given by

$$J_n = qD_n\frac{\partial n}{\partial x} - qn\mu_n\frac{\partial \psi}{\partial x} \tag{2.5}$$

$$J_p = -qD_p\frac{\partial p}{\partial x} - qp\mu_p\frac{\partial \psi}{\partial x} . \tag{2.6}$$

Discretized forms of these equations constitute the basis of the numerical model. Successive refinements are possible, depending on what processes we include in the recombination and generation rates R and G, what form we assume for the concentration of occupied traps n_t, what velocity-field relations we include in the mobilities μ_n and μ_p, and so on. (The diffusivities D_n and D_p are derived from μ_n and μ_p according to the Einstein relation $D = \mu kT/q$.) Various versions of the numerical model, along with the results they predict, are discussed in Chapters 4 and 5 below (and are summarized in the lower half of Table 2.1.) A schematic band diagram showing the problem as it appears in the numerical model is given in Figure 2.1a.

Simplified models. In order to treat the problem analytically, and thus to gain more insight than can be had from the numerical solutions alone, some simplifying assumptions must be made. The traditional approach is that of

	further simplifications:	in [1]	here	V_{cr}†	SCL‡	*advantages*
SIMPLIFIED: • single carrier • drift only • no recomb. • ideal contacts (SI only)	PARAMETRIC SOLUTION • constant mobility	Ch.4	§3.2		≥ 2	– implicit analytic JV
	REGIONAL APPROX. + • one class of e^-/region	Ch.4	—	trap filling (TF)	≥ 2	– spatial variations
	EXTENDED PHENOM. + • one class of e^-/regime	—	§3.2	(TF)	≥ 2	– piecewise explicit JV
	PHENOMENOLOGICAL + • constant $n(x), n_t(x), \theta$	Ch.2	§3.1		2	

	additional physics:	*here*	V_{cr}†	SCL‡	*advantages*
NUMERICAL: • two carrier • drift+diffusion • SRH recomb. • n-SI-n	— (constant mobility)	§4.2		≥ 2	– accurate treatment of thin layers & prediction of critical behavior
	• velocity saturation	§4.3		≥ 1	
	+ • negative differential mobility	§4.3	trap filling (TF)	> 0	
	+ • field emission from traps	§4.4		> 0 (incl.2)	
	without field emission: + • recombination through traps	§5.1		> 0	
	+ • impact ionization	§5.2	TF and/or avalanche breakdown	> 0	
	+ • radiative recombination				

Table 2.1: Summary of attributes of models discussed in this work. + indicates that the simplification(complexity) so marked applies *in addition to* all of above simplifications(complexities) within the simplified(numerical) approach.
† mechanism of steep rise in current
‡ slope of log J vs. log V in space-charge-limited regime below steep rise.
This summary is provided for handy reference; the meanings of the columns marked with † and ‡ will be made clear in Chapters 3–5.

Lampert and Mark [1] (and it is their terminology that we are following in our use of the terms "simplified" and, below, "phenomenological"). In the simplified theory, the problem is rendered tractable by restricting it to single-carrier drift current and by considering the insulating layer only. That is, we ignore holes, recombination/generation, and carrier diffusion, and we assume ideal contacts. We also assume that the trapped electrons are in quasi-thermal equilibrium with the free electrons, and that no large-field effects (such as velocity saturation) are present. A schematic band diagram for the resulting problem is given in Figure 2.1b.

Because the simplified models involve only one carrier type (electrons, in our case), in order to maintain charge neutrality at equilibrium we now must count the thermal and injected carriers separately. We have four classes of carriers: thermal free electrons (n_0), thermal trapped electrons (n_{t_0}), injected free electrons $(n - n_0)$, and injected trapped electrons $(n_t - n_{t_0})$. The thermal electrons are balanced by an equal number of positive charges; only the injected electrons contribute a net space charge. The Poisson equation (2.2) thus becomes

$$-\frac{\partial^2 \psi}{\partial x^2} = \frac{dE}{dx} = -\frac{q}{\epsilon} \cdot [(n - n_0) + (n_t - n_{t_0})] \qquad (2.7)$$

where we have introduced the electric field $E = -d\psi/dx$. If the trapped electrons are in quasi-thermal equilibrium with the free electrons, the total concentrations n_t and n are related by

$$n_t = \frac{N_t}{1 + g \exp[-(\xi_{Fn} - \xi_t)/kT]} = \frac{N_t}{1 + gn_1/n} , \qquad (2.8)$$

where we define $n_1 \equiv N_C \exp[-(\xi_C - \xi_t)/kT]$. The ionized donor concentration N_d enters the Poisson equation only through n_0 and n_{t_0}.

With the simplifying assumptions of neglecting holes, recombination/generation, and diffusion current, the continuity equations (2.3–2.6) reduce to

$$J = J_n = nq\mu_n E = \text{constant.} \qquad (2.9)$$

Neglecting diffusion current also implies that we are injecting electrons from an ideal cathode, with $E(x = 0) = 0$.

Parametric solution. The set of equations (2.7–2.9) can be solved analytically, but the solution is unwieldy and does not yield an explicit *J-V* characteristic. That is, both the position and the potential are expressed in

terms of the electric field, which becomes a parameter for the solution. We refer to this as the full or parametric solution to the simplified problem. Further simplifications are possible, as follows:

Regional approximation. A less unwieldy solution can be obtained by splitting the layer up into regions according to which class of carriers is the most numerous in each, and assuming that, in a given region, one class of carriers controls the problem. The solution in each region is carried out subject to the condition that the field and the carrier concentrations be continuous across the boundaries of the regions. Piecewise implicit solutions for the J-V characteristic can be obtained, depending on which regions are present for a given bias level. This technique is treated extensively by Lampert and Mark, and will not be discussed here.

Phenomenological approach. The most drastic simplification is to assume that a single class of carriers dominates the behavior of the entire sample, and possibly also that the carrier concentrations are constant everywhere. (In the latter case, the electrostatics is brought into the problem through a capacitance.) The J-V characteristic is divided into regimes of operation, according to which class of carriers dominates; the result is a four-section straight-line approximation to the $\log J$ - $\log V$ characteristic, which yields considerable insight.

Extended phenomenological approach. As an intermediate step between the phenomenological and full parametric solutions, we propose some simple extensions that can be grafted onto the phenomenological solution to yield a more accurate J-V characteristic. These extensions are best described in the context of a detailed exposition of the phenomenological approach, so we will not attempt to summarize them here. The phenomenological and extended phenomenological approaches, as well as the parametric solution to the simplified problem, are discussed in more detail in Chapter 3 (and are summarized in the upper half of Table 2.1.)

2.3   Why all these models?

Our goal with both the simplified and the numerical models is to understand and predict the electrical characteristics of Fe:InP as a function of the material properties, such as the doping levels. The various models offer different contributions toward that goal.

At one extreme, we have the phenomenological approach, which yields

simple expressions describing a piecewise approximation to the *J-V* curve. This approach, in which only the most basic physics is retained, does not describe everything we experimentally observe, but is necessary for understanding any more complicated model that does. At the other extreme is the numerical model, with many physical processes included. The numerical model gives greater accuracy and is valid over a broader range of doping levels and operating conditions, but by itself is difficult to understand and yields useful trends only after repeated calculations.

In this work, we present results from both the simplified and numerical models, because we believe that each adds value to the other. The numerical results are more readily understood on the basis of the insight gained from the simplified model. Furthermore, by building up the numerical model in stages, we can identify the influence of various physical processes. We demonstrate the effect of carrier diffusion by comparing the results of the simplest numerical case to those of the full simplified theory, and then go on to include other processes that cannot be handled analytically. By first thoroughly understanding the drift-only problem, we use the simplified theory to inform our interpretation of the numerical results.

On the other hand, the numerical results also inform our application of the simplified theory, by allowing us to evaluate the validity of the simplifying assumptions under various circumstances. The simplified theory is familiar to many and forms the traditional framework for discussion; therefore, it is important that we know its limitations and be able to judge the accuracy of its approximations. In addition to providing a more accurate picture, the numerical model gives us a good understanding of the range of applicability of the simplified theory.

We present several versions of the numerical model, in order to show the effects of various physical processes. These include carrier diffusion (Section 4.2), drift velocity saturation and negative differential mobility (Section 4.3), field emission from the traps (Section 4.4), recombination through the traps (Section 5.1), and band-to-band impact ionization (Section 5.2).

We present several versions of the simplified theory, as an aid to understanding. The parametric solution (Section 3.2) to the simplified problem provides a bridge between the insight gained from the phenomenological theory (Section 3.1) and the accuracy gained from the numerical model; that is, we understand the parametric solution on the basis of the phenomenological theory, and we understand the numerical results by comparing them with the parametric solution. The extended phenomenological approach (also in

Section 3.2) offers an intermediate step between the phenomenological theory and the parametric solution. It does not have the analytic simplicity of the phenomenological approach, but is still conceptually simple and easy to grasp, while yielding results that agree well with the parametric solution.

That the numerical model is not merely a small correction to the simplified theory can be seen in Figure 2.2. Here we show the critical voltage calculated in the two models, as a function of the thickness of the SI layer, for two different trap densities. (The critical voltage, an important performance criterion, can be loosely defined as the voltage at which the current starts to rise steeply, or the voltage below which the current density is satisfactory for a particular application. For this work, it has been taken as the voltage above which the current density exceeds 1 A/cm^2.) As we will see in Chapter 6, the numerical model is in much better agreement with experiment. The simplified theory gives a good estimate of the critical voltage only when the layer is thick enough that interface effects do not dominate, yet not so thick that field effects become important before most of the traps are filled. For a low trap density, there may be a large range of thicknesses over which the simplified theory gives a good estimate of the critical voltage; for a high trap density, there is hardly any thickness for which this is so.

We emphasize that, although its simplifying assumptions fail for both thin and thick layers, the simplified theory forms a valuable basis for further understanding and for identifying the processes that dominate the operation in regimes for which it fails. Similarly, regardless of whether a given experimental result can be explained on the basis of the numerical models discussed here, these models provide a basis for understanding what is going on. By showing the implications of the various physical processes that they do treat, the models may allow us to conclude that other processes must be responsible for some observed behavior, and aid in the identification of those other processes.
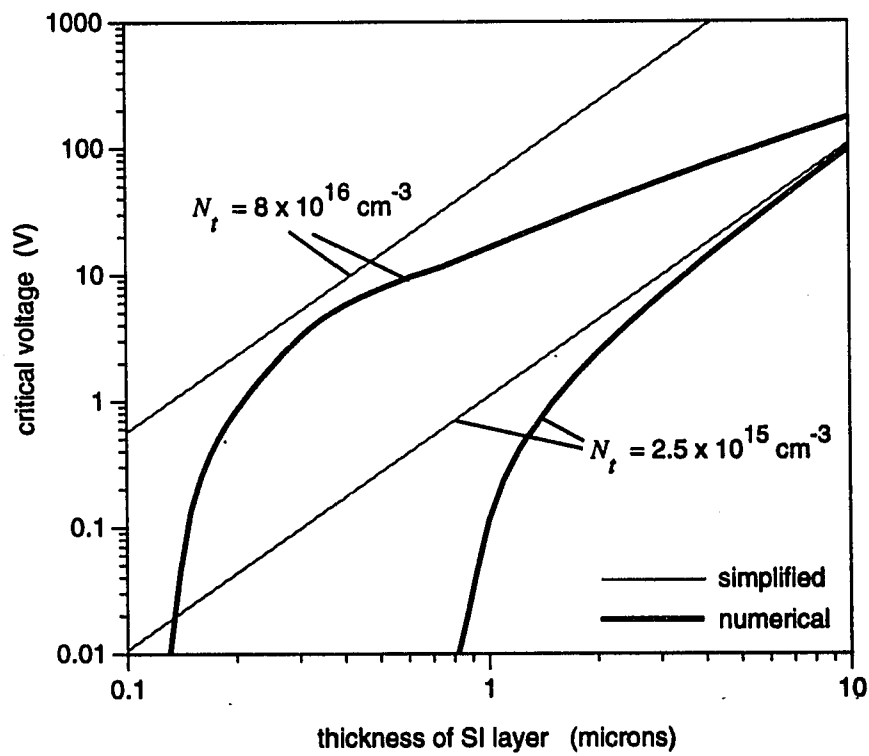
Figure 2.2: Critical voltage as a function of SI layer thickness, for large and small trap densities, comparing numerical results with simplified theory. Numerical model includes carrier diffusion, nonlinear velocity-field characteristics, SRH generation/recombination, and impact ionization.

Chapter 3

Simplified theory

In their classic work *Current Injection in Solids* [1], Lampert and Mark expound a simplified theory of current injection in trap-controlled insulators. This theory forms the basis of our understanding, so we review it here. In later chapters we will be referring to regimes of operation whose meaning is made clear in the framework of the simplified theory. In the present chapter, we apply the simplified theory to the case of Fe in InP, and calculate the spatial distribution of filled traps, as a function of bias level, predicted by this theory.

The assumptions underlying the simplified theory were mentioned in Chapter 2. To repeat, these include:

- Holes can be neglected (for our case of electron injection).
- Carrier diffusion can be neglected.
- Recombination/generation can be neglected.
- Free and trapped carriers are in quasi-thermal equilibrium.
- Carrier mobility is constant.

In Section 2.2, we gave a mathematical statement of the problem based on these simplifying assumptions, showing how the equations of the simplified theory (2.7–2.9) relate to the standard Poisson and continuity equations (2.2–2.6). We then mentioned several ways in which the simplified problem can be made even simpler, so as to yield more insight at the price of some accuracy. In this chapter, we discuss three approaches to the simplified theory: the phenomenological approach, which is easiest to understand; the full parametric solution, which has the greatest accuracy; and an extended phenomenological approach, as an intermediate step connecting the accuracy to the understanding. The phenomenological approach and the full solution are discussed by

Lampert and Mark; we propose the extended phenomenological approach as an alternative to the technique of regional approximation. Since computational resources are now readily available, the value of the intermediate approaches is today primarily pedagogical. For this purpose, the extended phenomenological theory adequately explains the J-V characteristics while retaining the conceptual simplicity of the phenomenological approach.

3.1 Phenomenological approach

Recall that we can divide the carriers into four classes: thermal free electrons, thermal trapped electrons, injected free electrons, and injected trapped electrons. The essence of the phenomenological approach is the assumption that, in each operating regime, one of these classes of carriers dominates the behavior of the entire sample, so that the other carriers may be ignored for purposes of solving the Poisson equation.

The relative populations of carriers in the four operating regimes are shown schematically in Figure 3.1. These are actually bar charts indicating the number of free, trapped, thermal, and injected electrons. The suggestion of a band diagram is used only to show which carriers are free and which are trapped. Open circles represent thermal carriers, and filled circles represent injected carriers.

As we increase the injection level, we encounter in sequence the ohmic, shallow-trap space-charge-limited (SCL), trap-filled-limited (TFL), and trap-free SCL regimes. The ohmic regime (Figure 3.1a) is so called because here the number of thermal electrons is larger than the number of injected electrons; the premise of Ohm's Law is that the applied bias does not change the free carrier concentration. At somewhat higher injection levels, the number of injected carriers exceeds the number of thermal carriers, and we enter the shallow-trap SCL regime (Figure 3.1b). Here the injected trapped carriers are the most numerous class, and they dominate the space charge. So long as most of the traps are still empty, the ratio of the concentrations of free and trapped electrons remains constant. While this remains true, the number of free carriers remains proportional to the space charge, and this gives SCL current flow. (The ratio of the concentrations of free and trapped carriers in the ohmic and shallow-trap SCL regimes is governed by Boltzmann statistics. This ratio is drawn in Figure 3.1 as 1:2, but is actually around $1:10^9$. The reason for the designation "shallow-trap" is discussed below.)

thermal
↓ ┌ injected
⊙ ◖   ◄── free

⊙⊙◕ ___ ◄── trapped

(a) ohmic regime

⊙●●

⊙⊙●●●● ___
            ～ empty traps

(b) shallow-trap SCL regime

⊙●●●●●

⊙⊙●●●●●●

(c) TFL regime

⊙●●●●●●●●●●

⊙⊙●●●●●●

(d) trap-free SCL regime
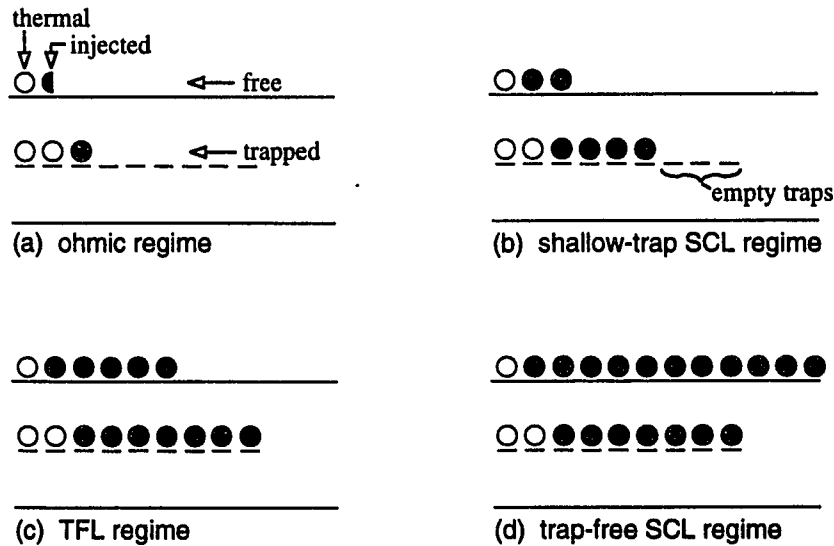
Figure 3.1:   Relative carrier populations under various injection conditions. Open circles represent carriers that are present at thermal equilibrium; filled circles represent additional carriers injected under bias.

At still higher injection levels (Figure 3.1c), empty traps become scarce. In this trap-filled-limited regime, the injected trapped carriers are still the most numerous and still dominate the space charge, but now the number of injected free electrons starts to rise rapidly, and so does the current. Finally, at the highest injection levels, the injected free electrons outnumber the injected trapped electrons, so that free electrons dominate the space charge (Figure 3.1d). Then we are back to a situation in which the number of free carriers is proportional to the space charge, so we again have SCL current flow. This regime is termed "trap-free" because here the trapped charge can be neglected with respect to the free charge.

As we mentioned above, the phenomenological approach is based on ignoring all but the most numerous class of carriers for the solution of the Poisson equation in each regime. The result is a piecewise approximation to the J-V characteristic, as shown for example by the dashed line in Figure 3.2. Current-voltage relations describing the various regimes are developed below, as are expressions for the distribution of occupied traps in the various regimes. The ohmic, shallow-trap SCL, and trap-free SCL regimes are all treated by simultaneous solution of the Poisson and continuity equations; we have $J = nq\mu_n E$
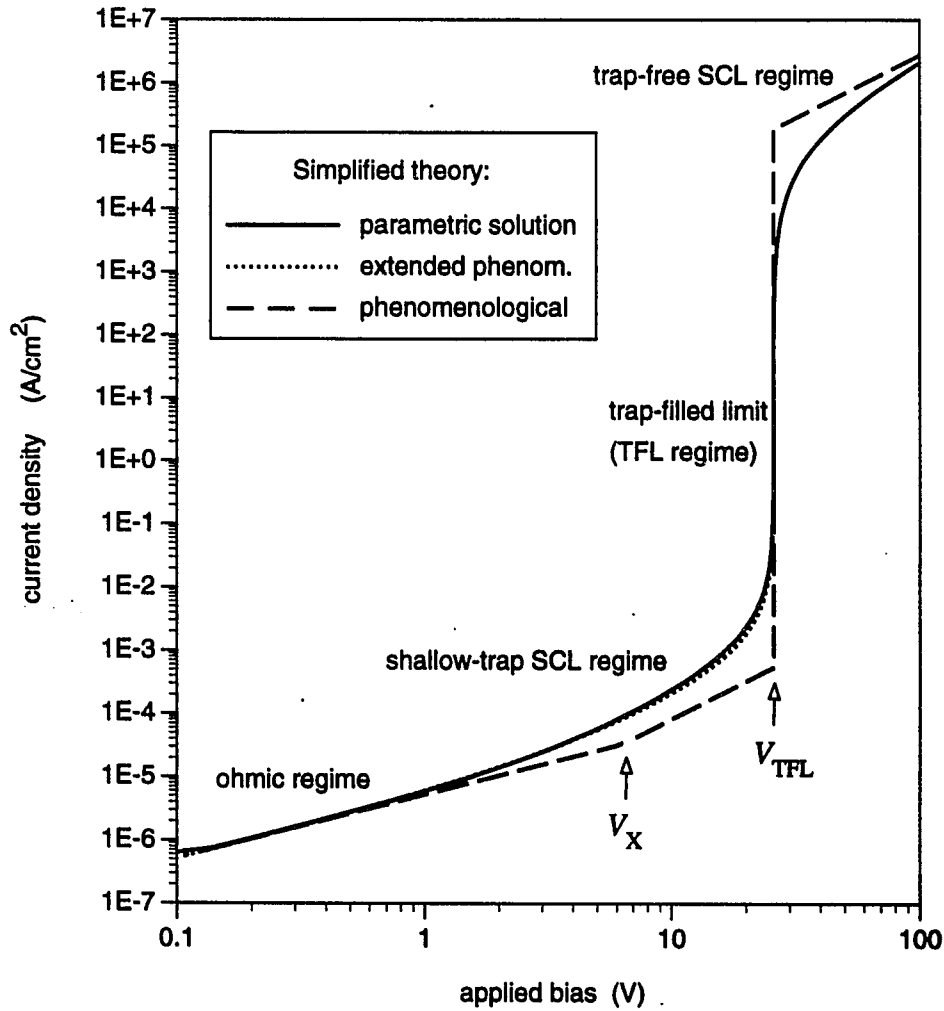
Figure 3.2: J-V curves in various versions of simplified theory: (i) phenomenological, (ii) parametric solution, (iii) extended phenomenological treatment. $N_t = 1 \times 10^{16}$ cm^{-3}, $N_d = 1 \times 10^{15}$ cm^{-3}, $L = 2$ μm, $\mu_n = 2000$ cm^2/V-s. In the SCL regimes, the phenomenological curves shown are those that result from assuming a constant carrier concentration and approximating the electrostatics with $Q = CV = \epsilon V/L$.

in all three cases, with the differences coming in the forms of n and E. The TFL regime is treated differently. Because of this, and because it is most easily understood as a transition between the two SCL regimes, we treat the TFL regime last.

Ohmic regime. Here at the lowest biases, the thermal carriers dominate. Since there is no space charge associated with these, we have $Q = \rho L = 0$ and $dE/dx = 0$. Only the free carriers contribute to current flow. We invoke $J = nq\mu_n E$ (where $n = n_0$ is the concentration of thermal free carriers) to obtain

$$J = n_0 q \mu_n V/L \;, \tag{3.1}$$

where L is the thickness of the SI layer. Since the field is constant and the carrier concentration is independent of bias level, $J(V)$ is linear, and the slope of $\log J$ vs. $\log V$ in this regime is 1. The concentration of occupied traps is uniform by assumption, and equal to the bulk equilibrium value n_{t_0}. If $N_d \gg n_i$, then $n_{t_0} = N_d$. Also, from (2.8) we have $n_0 = gn_1 n_{t_0}/(N_t - n_{t_0}) = gn_1 N_d/(N_t - N_d)$. Thus, the current density in the ohmic regime is proportional to gn_1, which is a characteristic of the trap, as well as to the carrier mobility μ_n.

Shallow-trap SCL regime. At higher biases, the number of injected trapped electrons $(n_t - n_{t_0})$ becomes large compared to that of both thermal free and thermal trapped electrons, so we neglect the thermal carriers in the solution of the electrostatics problem and have $dE/dx = qn_t/\epsilon$. The trapped electrons do not contribute to current flow, but we can relate the free electron concentration to the trapped electron concentration, since the two populations are assumed to be in quasi-thermal equilibrium. If the trap is shallow enough (i.e. at high enough energy) with respect to the quasi-Fermi level in this regime, the Boltzmann approximation can be applied to the occupation statistics for the trap as well as to the occupation statistics for the conduction band, and the ratio θ of the free carrier concentration to the trapped carrier concentration is approximately independent of bias level:

$$\theta \equiv n/n_t = n(1 + gn_1/n)/N_t \cong gn_1/N_t \tag{3.2}$$

using (2.8). Note that θ is a small number, on the order of 10^{-9}. Then, still using $J = nq\mu_n E$ (where now $n = \theta n_t$ is the concentration of injected free electrons), we have for the J-V characteristic

$$J = \chi \cdot \theta \epsilon \mu_n V^2/L^3. \tag{3.3}$$

Here $\chi = 9/8$ from the solution of the Poisson equation. As in the ohmic regime, the current density is proportional to gn_1. Here, however, $J(V)$ is quadratic, and the slope of $\log J$ vs. $\log V$ is 2. The quadratic current-voltage relation arises from the fact that the free carrier concentration depends on the bias level.

The latter point can be most easily seen by taking a slightly different approach to the derivation, making an even stronger simplification. What we have done so far is to neglect all but one class of carriers (namely the injected trapped electrons) in the solution of the Poisson equation; we have still allowed these carriers to be non-uniformly distributed in space. As developed by Lampert and Mark, the phenomenological approach also neglects spatial variation of the carrier densities. With this added assumption, the Poisson equation is not solved directly; rather, using the relation $Q = CV$, the electrostatics is brought into the problem through the capacitance C, whose form we assume we know. (We refer to this as the "pure" phenomenological approach; we will use it again in treating the TFL regime below.) In the regimes of SCL current flow, we take the parallel-plate form $C = \epsilon/L$. Thus $Q = qn_tL = CV = \epsilon V/L$, and $n = \theta n_t = \theta CV/qL = \theta \epsilon V/qL^2$. In $J = nq\mu_n E$, therefore, both n and E are proportional to V, giving a quadratic current-voltage relation.

Solution of the Poisson equation for this regime shows that the spatial distribution of occupied traps is non-uniform: $n_t(x) = [\epsilon J/2q^2\theta\mu_n]^{1/2}x^{-1/2}$. Much of the negative charge is near the cathode ($x = 0$), justifying the phenomenological approximation $C \cong \epsilon/L$. The error introduced in (3.3) by the latter approximation is just the geometric factor χ: the purely phenomenological approach gives $\chi = 1$, whereas the exact solution to the Poisson equation (still subject to the condition that one class of carriers dominates everywhere) gave us $\chi = 9/8$.

In designating this the "shallow-trap SCL" regime, we are following Lampert and Mark in the use of the term "shallow". In the context of our work, which deals with deep acceptor traps, by a "shallow trap" we simply mean one that lies far enough above the quasi-Fermi level to allow the use of the Boltzmann approximation for its occupation statistics. Whether a particular trap is "shallow" at a given temperature thus depends on the doping densities and on the injection level as well as on the ionization energy of the trap. As we shall see, in many common situations the Fe acceptor in InP cannot properly be treated as a "shallow trap".

Trap-free SCL regime. At extremely high biases, the number of injected free electrons becomes large compared to the number of injected trapped

electrons, so for the electrostatics problem we ignore all but the injected free electrons and have $dE/dx = qn/\epsilon$, which with $J = nq\mu_n E$ (where n is again the concentration of injected free electrons) gives

$$J = \chi \cdot \epsilon\mu_n V^2/L^3 \ . \tag{3.4}$$

Here again $\chi = 9/8$, or for the purely phenomenological approach we can take $Q = qnL = CV$ so that $\chi = 1$. All of the traps are filled in this regime, so the concentration of occupied traps is uniform and equal to N_t.

Comparison of (3.4) with (3.3) might suggest that $\theta = 1$ for the trap-free SCL regime, and this is true in the sense that (for the shallow-trap SCL regime) θ represents the ratio of the number of electrons that carry current to the number of electrons that contribute to the space charge. In the trap-free SCL regime, in which we consider only the injected free electrons, every electron contributes both to the current and to the space charge. However, as defined in the discussion above, θ relates the concentrations of free and trapped electrons, and (3.3) is derived under the assumption that this ratio is a constant, independent of bias level. This is not the case in the trap-free SCL regime, so the comparison of (3.4) with (3.3) using the strict definition of θ is invalid. In fact, the trap-free-SCL assumption that the trapped carriers can be neglected corresponds to $\theta \gg 1$. (We will consider the dependence of θ on injection level when we take up the extended phenomenological approach in Section 3.2.)

TFL regime. The trap-filled-limited (TFL) regime forms the transition between the shallow-trap SCL regime and the trap-free SCL regime. (We are assuming here that enough traps are present in relation to thermal carriers for the shallow-trap SCL regime to appear at all; it is also possible to have a TFL transition directly from ohmic to trap-free SCL behavior.) In the shallow-trap SCL regime, the space charge is dominated by injected trapped electrons, and the current is carried by injected free electrons which number a constant (and small) fraction of the trapped ones. In the trap-free SCL regime, the space charge is dominated by injected free electrons, and the current is carried by those same free electrons. In both cases, the number of free electrons is proportional to the number of electrons that are responsible for the space charge; it is this fact that gives rise to the square-law J-V characteristic in these regimes (under the assumption of constant mobility).

In the TFL regime, by contrast, the space charge is dominated by trapped electrons (as in the shallow-trap SCL regime), but the current is carried by injected free electrons whose number is not a constant fraction of the number of

trapped electrons (as in the trap-free SCL regime). As the traps fill up, injected electrons are no longer apportioned between the traps and the conduction band in the ratio of Boltzmann factors, but go instead increasingly into the conduction band. So long as the injected trapped electrons outnumber the free ones, however, the electrostatics is still dominated by the trapped charge. The result is that, since a given increment of injected charge may represent an insignificant change in the total space charge and still cause a large change in the free charge, a tiny increase in applied voltage can produce a large increase in the current.

The TFL regime is characterized in the phenomenological theory by a fixed voltage corresponding to the space charge of the injected trapped electrons, whose number is equal to the number of empty traps at thermal equilibrium, p_{t_0}. Since the charge is uniformly distributed through the layer (assuming the concentration of traps is constant), the capacitance per unit area is $C = 2\epsilon/L$. (Unlike the parallel-plate approximation that we used for the SCL regimes, this expression is exact.) The charge per unit area is $Q = q p_{t_0} L$, so that the trap-filled-limited voltage is given by

$$V_{\mathrm{TFL}} = \frac{Q}{C} = \frac{q p_{t_0} L^2}{2\epsilon} . \tag{3.5}$$

This expression, derived under the assumptions of the phenomenological theory, applies equally to the steep section of the J-V curve as calculated from the full parametric solution to the simplified problem (see below). Note that the simplified theory predicts a quadratic dependence of V_{TFL} on thickness.

The phenomenological approach yields simple expressions for $J(V)$ in the various regimes of operation, allowing us to relate the J-V characteristics to the properties of the material. It thus suggests the possibility of extracting information about those properties from the J-V characteristics. For example, we saw in (3.5) how the trap-filled-limited voltage V_{TFL} depends on the layer thickness and on the equilibrium density of empty traps. Similarly, the crossover voltage V_{X} between the ohmic and shallow-trap SCL regimes depends on the background donor concentration: by equating the current densities in these two regimes, we find

$$V_{\mathrm{X}} = \frac{q N_d L^2}{\chi \epsilon} . \tag{3.6}$$

Thus, if the thickness of the layer and the permittivity are known, the doping

levels can be obtained from the corner voltages in the *J-V* curve:

$$N_d = \frac{9}{8} \frac{\epsilon}{qL^2} \cdot V_{\mathrm{X}} \tag{3.7}$$

$$N_t = \frac{\epsilon}{qL^2} \left(2V_{\mathrm{TFL}} + \frac{9}{8} V_{\mathrm{X}} \right) . \tag{3.8}$$

Since the current density in both the ohmic and shallow-trap SCL regimes is proportional to the product of g and μ_n, it is not possible from a *J-V* curve alone to determine these quantities independently. (We will return to this point in Chapter 8.) However, if one is known—as, for example, the mobility from a time-of-flight measurement—then the other can be determined from the *J-V* curve, assuming that the energy level of the trap can be had from spectroscopic techniques.

The *J-V* characteristics could thus provide a useful method for determining materials properties in a semi-insulating layer. We shall see, however, that we encounter a number of difficulties in trying to apply this method to Fe:InP. One of these is evident from the exact solution to the simplified problem, and is addressed in the next section.

The phenomenological approach to the simplified problem gives considerable insight into the current-voltage behavior in a trap-controlled insulator, at the price of some accuracy. To see exactly what is implied in the original equations (2.7–2.9) describing the simplified problem, we next consider the full solution to this problem.

3.2 Parametric solution and extended phenomenological approach

The phenomenological *J-V* characteristic was derived under the assumption that, for a given injection level, one class of carriers dominates the electrostatics problem everywhere in the sample. Making no such assumptions about the carrier concentrations, we return to the original simplifying assumptions (single carrier, drift only, no generation/recombination, etc.) as formulated in Equations 2.7–2.9. (These are repeated as 3.9–3.11 below.) In this section we present the results of the exact (parametric) solution of the simplified problem, and also discuss some extensions to the phenomenological approach. These extensions can be used to improve the accuracy of the phenomenological approximation to the *J-V* characteristic, while retaining the conceptual

simplicity of the phenomenological approach; and they serve as a means of explaining the detailed form of the parametric J-V curve.

Once again, the statement of the simplified problem is:

$$\frac{dE}{dx} = -\frac{q}{\epsilon} \cdot [(n - n_0) + (n_t - n_{t_0})] \tag{3.9}$$

$$n_t = \frac{N_t}{1 + gn_1/n} \tag{3.10}$$

$$J = nq\mu_n E = \text{constant} \tag{3.11}$$

with the boundary condition

$$E(x = 0) = 0. \tag{3.12}$$

This set of equations can be solved analytically for $V(J, E)$ and $x(J, E)$ [1]. The technique is to substitute $n = J/q\mu_n E$ in the Poisson equation, leaving

$$\frac{dE}{dx} = \mathcal{F}(J, E) \tag{3.13}$$

so that

$$x = \int dx = \int (dx/dE)\, dE = \int \mathcal{F}^{-1}(J, E)\, dE \tag{3.14}$$

$$V = \int E\, dx = \int E\, (dx/dE)\, dE = \int E\, \mathcal{F}^{-1}(J, E)\, dE\ . \tag{3.15}$$

These are integrated using the method of partial fractions; the solution is shown in Appendix C. In all cases the integration runs from zero field at the cathode boundary up to the value of the field at the position of interest. As noted, the solution does not yield an explicit current-voltage relation for a given layer thickness L; rather, it yields the position x and the voltage V at that position as functions of the field E and the current density J. To obtain the J-V curves shown in this work, J was taken as the independent variable, and $x(J, E) = L$ was inverted by iteration to give $E(J)$ at position L. This was then inserted into $V(J, E)$ to yield $V(J)$ at position L, the desired result. An example is plotted as the solid line in Figure 3.2.

The discrepancy between the parametric solution and the results of the phenomenological approach below the trap-filled limit can be understood mainly in terms of two effects. First, the phenomenological approach neglects the contribution to the total current of injected carriers in the ohmic regime and

of thermal carriers in the SCL regime; but in fact these two contributions add in both regimes. This effect tends to obscure the ohmic-to-SCL transition and increases the current in both regimes above that predicted by the phenomenological theory. Second, the energy level of Fe in InP is near enough to the equilibrium Fermi level that the shallow-trap approximation is not very good over most of the "shallow-trap" SCL regime. That is, enough of the traps are filled that the Boltzmann approximation fails to describe the occupation probability for the trap, and θ is no longer independent of bias level.

We can assess these effects by including them as extensions to the phenomenological theory. The dotted curve in Figure 3.2 was calculated using the phenomenological approach and (a) including the factor $\chi = 9/8$ that results from exact solution of the Poisson equation in the shallow-trap SCL regime, (b) adding the current contributions from thermal and injected free carriers in the ohmic and shallow-trap SCL regimes, as well as (c) assuming a bias-dependent $\theta(V)$ in the shallow-trap SCL regime. For the latter, the shallow-trap SCL square law (3.3) is derived as usual, and then $\theta(V)$ is inserted into the result. $\theta(V)$ is defined by

$$\theta(V) = \frac{n}{n_t} = \frac{n(V) + gn_1}{N_t} , \qquad (3.16)$$

where $n(V)$ is taken from the phenomenological relation

$$Q = qL \left[(n - n_0) + \left(\frac{N_t}{1 + gn_1/n} - n_{t_0} \right) \right] = CV . \qquad (3.17)$$

We have used $C = 2\epsilon/L$ because the charge is approximately uniformly distributed in the regime for which this correction becomes important. We find

$$n = \frac{1}{2} \left(-b + \sqrt{b^2 - 4c} \right) \qquad (3.18)$$

where

$$b \equiv gn_1 + N_t - n_0 - n_{t_0} - 2\epsilon V/qL^2 \qquad (3.19)$$

$$c \equiv gn_1(-n_0 - n_{t_0} - 2\epsilon V/qL^2) . \qquad (3.20)$$

This technique saves computation time over the parametric solution for the J-V curve, and yields results which agree well with the parametric solution below the trap-filled limit. It is simpler in form than either the parametric solution

or the regional approximation, and is valuable as an aid to understanding, in the spirit of the phenomenological approach. It does not, however, provide a way of calculating the spatial distribution of the field and the trapped charge.

Note that for the doping levels used in Figure 3.2, neither the full solution nor the extended phenomenological solution exhibits an extended regime in which the slope of $\log J$ vs. $\log V$ is 2. Rather, the slope changes gradually throughout the "shallow-trap" SCL regime, indicating a variation in θ with injection level and thus a failure of the shallow-trap approximation. The transition from ohmic to SCL conduction is very smooth, without an easily-identifiable crossover voltage. Thus, while the "pure" phenomenological approach suggests that the doping levels can be readily extracted from the J-V curve according to (3.7–3.8), the full solution shows that such an extraction can be very difficult in practice. (The full solution does predict a well-defined V_{TFL}, from which the difference $N_t - N_d$ can be obtained. Another approach to the extraction of doping information from J-V curves is mentioned in Chapter 8.)

We have discussed the parametric solution to the simplified problem for two reasons. First, it gives us a standard by which to judge the adequacy of the phenomenological solution as an approximation for the simplified problem. Indeed, we saw that (with certain extensions) the phenomenological approach can be made to yield a very good approximation; so our understanding of the simplified problem as based on the phenomenological approach is sound. Second, the parametric solution shows us exactly what is implied in the formulation describing the simplified problem, so that we may more easily understand which of the effects observed experimentally and/or predicted by a more complicated model are due to other physics and which are due simply to the physics contained in the simplified problem: electrostatics and single-carrier drift combined with Fermi-Dirac statistics for the occupation of the trap. For later comparison, we show in Figure 3.3 the J-V characteristics predicted by the simplified theory for several layer thicknesses, for a trap density of 8×10^{16} cm^{-3}.

The parametric solution also allows us to calculate the spatial variation of the field and of the carrier concentrations. The distribution of trapped carriers (occupied traps) is plotted in Figure 3.4 for $L = 2$ μm and the same doping as in Figure 3.3. The biases for which $n_t(x)/N_t$ is shown in Figure 3.4 are indicated by the filled circles in Figure 3.3. Although the progress of trap-filling in a sample is often described [7] in spatial terms, with the edge of a region of filled traps progressing across the sample (in effect, a regional
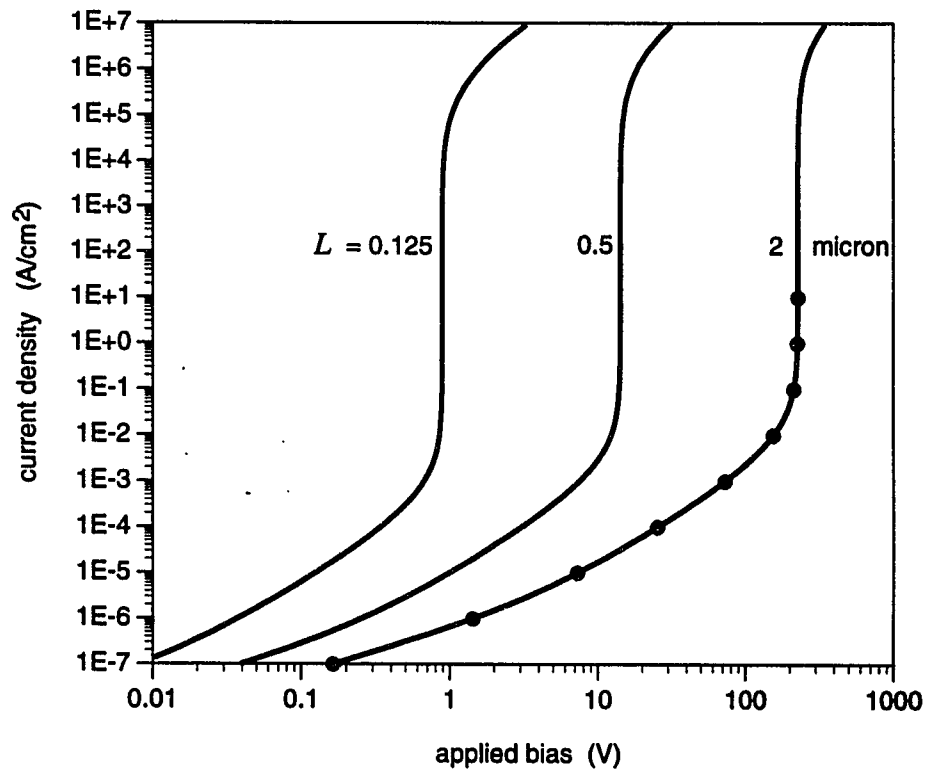
Figure 3.3: Simplified J-V characteristics for $L = 0.125$, 0.5, and 2 μm, from parametric solution, using $N_t = 8 \times 10^{16}$ cm^{-3}, $N_d = 1 \times 10^{15}$ cm^{-3}, $\mu_n = 2000$ cm^2/V-s. Filled circles on $L = 2$ μm curve indicate bias levels for Figure 3.4.
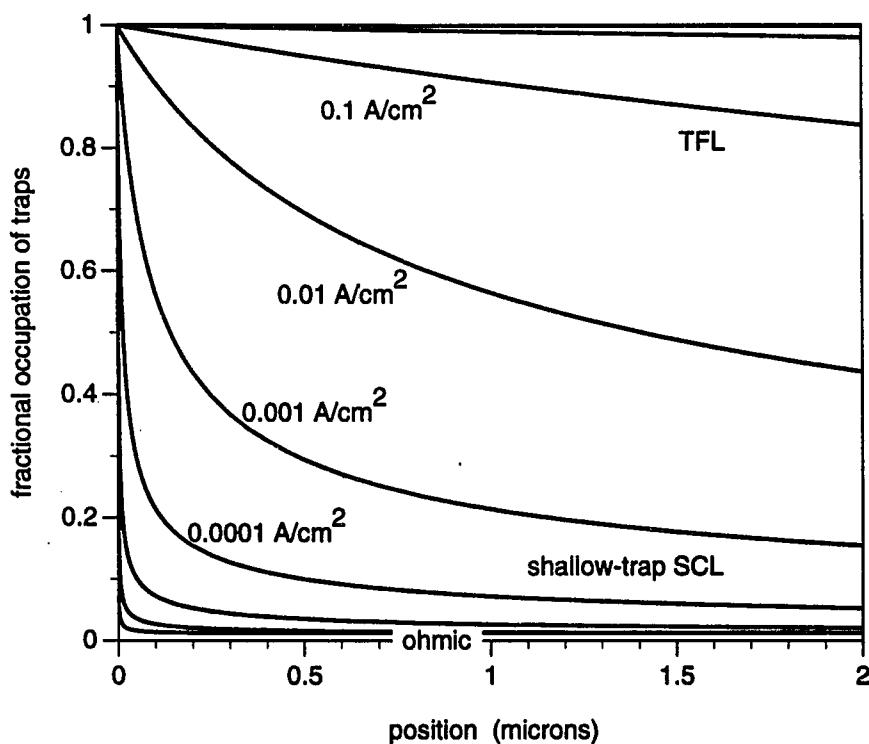
Figure 3.4:   Spatial distribution of occupied traps in simplified theory, for $L = 2$ μm, $N_t = 8 \times 10^{16}$ cm^{-3}, $N_d = 1 \times 10^{15}$ cm^{-3}, $\mu_n = 2000$ cm^2/V-s. Bias levels are 10^{-7}, 10^{-6}, 10^{-5}, 10^{-4}, 10^{-3}, 10^{-2}, 10^{-1}, 1, and 10 A/cm^2, as indicated by filled circles in Figure 3.3.

approximation), we see that it can be as well described in "phenomenological" terms, with a quasi-Fermi level progressing upwards in energy and describing the occupation of the traps over a large region of the sample. (This is the reason that the extended phenomenological approach works as well as it does.)

3.3 Difficulties with the simplified theory

The simplified theory predicts a quadratic dependence of critical voltage on layer thickness over the entire range of layer thicknesses. As can be seen from the family of simplified J-V curves in Figure 3.3, this simplified approach would suggest that (for the trap density shown) a 0.125-μm layer could still maintain $J < 1$ A/cm^2 at 0.88 V, and that a 2-μm layer could maintain $J < 1$ A/cm^2 at 225 V. As we might expect, and as we saw in Figure 2.2, this picture is unrealistic.

Depending on what values one assumes for the various parameters, the simplified theory can often be made to match an experimental J-V curve fairly well. For example, in Figure 3.5 we compare a measured J-V curve from a 2-μm epitaxial layer grown by MOCVD [13] to a theoretical J-V curve calculated from the simplified theory. In this case, the trap density used in the calculation was 7.7×10^{15} cm^{-3}, but we had no independent measure of the trap density in the sample. (SIMS data for a similar sample showed an Fe concentration of around 10^{17} cm^{-3}.)

When independent measures of the trap density are available, however, they sometimes point to much larger trap densities than a fit to the simplified theory would suggest. This is particularly true if one compares the measured critical voltage to the trap-filled voltage predicted by the simplified theory. For example, Wolf *et al.* [34] reported a trap density of 8×10^{16} cm^{-3}, from capacitance-voltage (C-V) measurements on a sample co-doped with Si. For a 3-μm layer with this trap density, and assuming a background donor concentration below 2.5×10^{15} cm^{-3}, the simplified theory predicts a trap-filled voltage in excess of 500 V; but Wolf *et al.* report a critical voltage of about 50 V.

Furthermore, we know on principle that many of the assumptions of the simplified theory are unphysical over some of the regimes shown in Figure 3.3. For example, the peak field for the 0.5-μm layer operating at 5 V would be well over 10^5 V/cm; we know that at this field it is unphysical to continue to assume a constant mobility. As we increase the field even further, we would expect
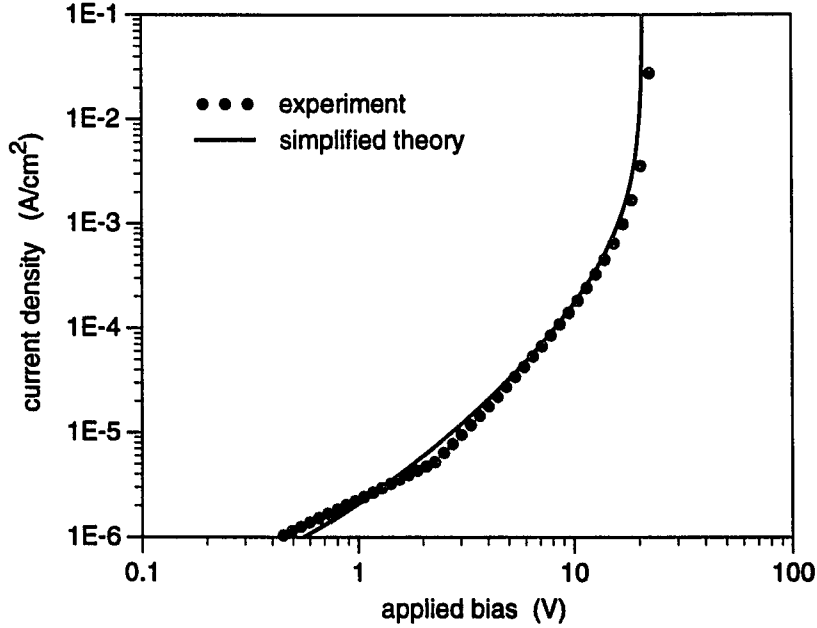
Figure 3.5:   Comparison of measured J-V curve with fit to simplified theory (a) experimental [13], (b) parametric solution using $N_t = 7.7 \times 10^{15}$ cm^{-3}, $N_d = 4 \times 10^{14}$ cm^{-3}, $\mu_n = 1200$ cm^2/V-s, and $L = 2$ μm.

that effects such as impact ionization would become important, especially for thicker layers (for which the avalanche breakdown field could be attained below the trap-filled limit). For thinner layers, in which the trap-filled limit occurs at lower field and in which band-bending at the interfaces would occupy a larger fraction of the total layer thickness, we would expect carrier diffusion at non-ideal contacts to play a larger role. In order to assess these and other effects, we turn to a numerical model.

Chapter 4

Trap filling and single-carrier effects

Using the numerical model, we can include various effects that were omitted from the simplified theory, and by comparing the numerical results with those of the simplified theory, we can examine the consequences of each effect in turn. (We stress that this is not just an academic exercise, but is necessary for an adequate description of the material.) In this chapter, we consider the effects of carrier diffusion, nonlinear velocity-field relations, and field emission from traps, and we examine the role of each in determining the course of trap filling and the resultant J-V characteristics. In particular, we show that the critical behavior for thin SI layers is dominated by diffusion from the contacts, and that space-charge-limited current flow need not be characterized by a quadratic J-V curve. In Chapter 5, we will turn to impact ionization and avalanche injection and examine some situations in which the critical behavior does not depend on trap filling.

4.1 Numerical model

Although in this chapter we study single-carrier effects, on which the influence of holes is negligible, in all of our numerical work we solve the full two-carrier problem. The basic formulation was given in Section 2.2 and is repeated here for convenience:

$$\frac{\partial^2 \psi}{\partial x^2} = -\frac{q}{\epsilon}(N_d + p - n - n_t) \tag{4.1}$$

$$\frac{\partial n}{\partial t} = \frac{1}{q}\frac{\partial J_n}{\partial x} - R + G = 0 \tag{4.2}$$

$$\frac{\partial p}{\partial t} = -\frac{1}{q}\frac{\partial J_p}{\partial x} - R + G = 0 \tag{4.3}$$

$$J_n = qD_n\frac{\partial n}{\partial x} - qn\mu_n\frac{\partial \psi}{\partial x} \tag{4.4}$$

$$J_p = -qD_p\frac{\partial p}{\partial x} - qp\mu_p\frac{\partial \psi}{\partial x} \; . \tag{4.5}$$

The Poisson equation (4.1) is solved simultaneously with the continuity equations (4.2–4.3) under various sets of assumptions about the physics. Initially, we retain many of the assumptions of the simplified theory. We then lift these assumptions one at a time, so as to isolate the contributions due to the various phenomena. The changes enter through the recombination and generation rates R and G, through the trap occupation function used to calculate n_t, and through the velocity-field relations embodied in the mobilities μ_n and μ_p.

The simplest form of the numerical model, discussed in Section 4.2, retains the assumptions of constant carrier mobility and of quasi-thermal equilibrium between the trapped and free electrons. That is, μ_n and μ_p in (4.4–4.5) are taken to be constants, and the trapped electron concentration n_t in (4.1) is derived from the free electron concentration n according to (2.8). We also continue to assume that there are no field-related generation processes. Comparing the predictions of this model to those of the simplified theory shows the effects of including carrier diffusion in the problem.

The effects of drift velocity saturation and negative differential mobility, for which μ_n and μ_p in (4.4–4.5) are taken to be functions of the local electric field, are discussed in Section 4.3. The effect of field emission, for which the trap occupation function is also taken to be a function of the local electric field, is discussed in Section 4.4.

In this chapter, we retain $R = G = 0$. In Chapter 5 we consider SRH recombination/generation, both through unspecified unintentional defects (R_0) and through the Fe level itself (R_t), and generation G by band-to-band impact ionization.

The numerical solution is discussed in Appendix D. Standard finite difference techniques [24] are used, with the electrostatic potential ψ and the free carrier concentrations n and p as independent variables. The drift-diffusion equations (4.4–4.5) are implemented in integral form, following the technique

of Scharfetter and Gummel [24, 35]. A three-layer, *n*-SI-*n* structure is defined by discontinuous changes in the doping levels N_t and N_d. In the *n*-type contact layers, for which $N_t = 0$, the donor concentration N_{dn} is taken as 5×10^{17} cm^{-3} for the calculations in Chapters 4 and 5. In the SI layer, we use a background donor concentration of 1×10^{15} cm^{-3}, as before. (The values of other constants used in the calculations are given in Appendix A.) Voltage (i.e. Dirichlet) boundary conditions are applied at the outside edges of the *n*-layers. That is, we demand that the carrier concentrations regain their bulk equilibrium values at the boundaries, and that the separation of the Fermi levels at the boundaries be equal to the applied voltage.

4.2 Carrier diffusion

For the simplified theory, we assumed the electric field to be zero precisely at the edge of the SI layer on the cathode side. We neglected any zero-bias bandbending in the SI layer at the contacts, and assumed that at zero bias the concentration of empty traps was constant and equal to its bulk thermal-equilibrium value across the entire layer. In actuality, of course, we will have bandbending at the interfaces as a result of the contact potential between the *n*-type contacts and the semi-insulating layer. Electrons diffuse into the SI layer from the *n*-layers, filling some of the traps. Under bias, we will have a potential barrier at the cathode side, and the point of zero electric field will occur inside the SI layer rather than at the interface. This effectively reduces the thickness of the SI layer. For a thick enough layer, this reduction is a small fraction of the total thickness, and the simplified theory remains a good approximation. For a thinner layer, however, the distance taken up by the barrier can be a significant fraction of the total layer thickness. For submicron layers, the bulk concentration of empty traps may never be attained at all in the limited distance available.

The distance required to empty the traps to bulk level decreases with increasing trap density. In Figure 4.1 we show zero-bias band diagrams for high and low trap densities for several layer thicknesses, from an exact numerical solution to the Poisson equation. The resulting distributions of filled traps at zero bias are shown in Figure 4.2. Note that for a thin layer all of the traps are already filled, even for $N_t = 8 \times 10^{16}$ cm^{-3}, and that for a 2-μm layer with $N_t = 2.5 \times 10^{15}$ cm^{-3} the concentration of empty traps at the center of the layer is only 50% of the bulk value.
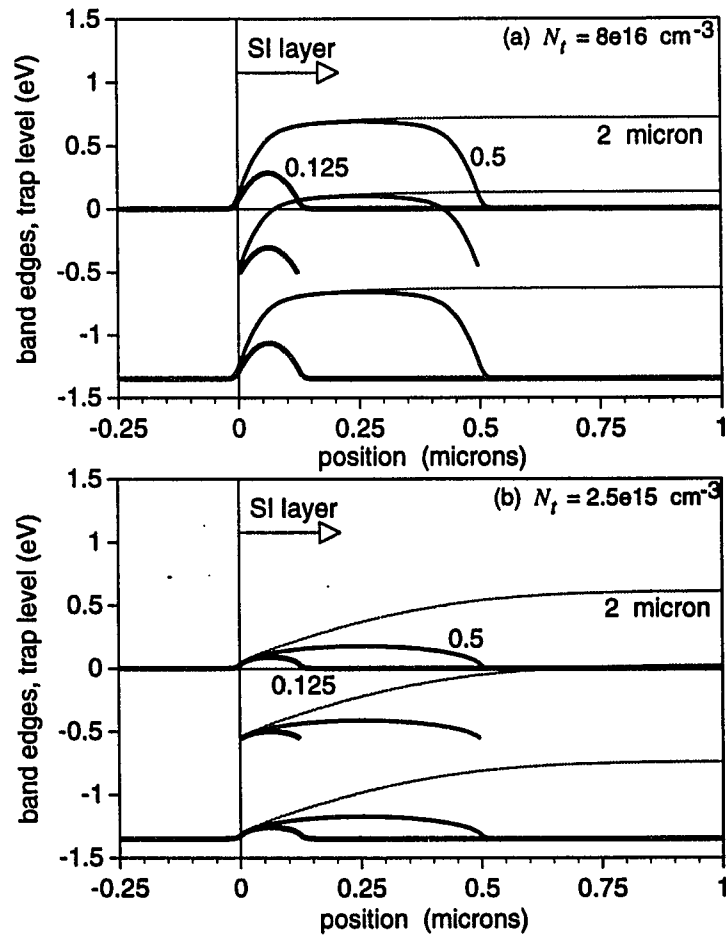
Figure 4.1:   Bandbending at contacts from numerical solution of Poisson equation at zero bias, for $L = 0.125$, 0.5, and 2 μm. (a) $N_t = 8 \times 10^{16}$ cm^{-3}; (b) $N_t = 2.5 \times 10^{15}$ cm^{-3}.
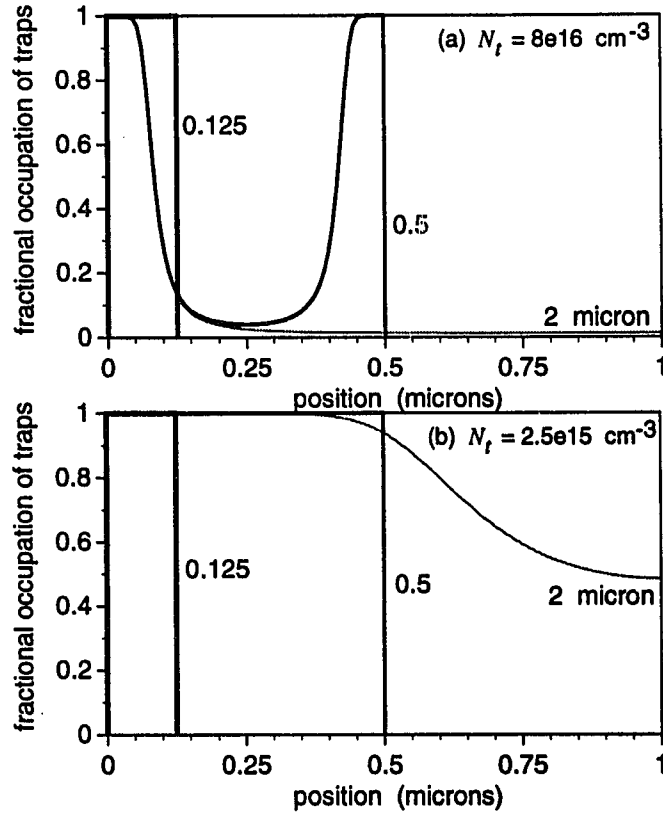
Figure 4.2: Distribution of filled traps at zero bias, for $L = 0.125$, 0.5, and 2 μm. (a) $N_t = 8 \times 10^{16}$ cm^{-3}; (b) $N_t = 2.5 \times 10^{15}$ cm^{-3}.

To treat the barrier correctly under bias, we include carrier diffusion in the problem, and solve the system of equations (4.1–4.5) above, continuing to treat the trap as a partially ionized deep acceptor in quasi-thermal equilibrium with the conduction band and retaining for now the other assumptions of the simplified theory (constant mobility, no high-field effects, etc.). J-V curves resulting from these calculations are shown in Figure 4.3, for the same set of layer thicknesses as in Figure 3.3. (For comparison, the simplified curves are reproduced here as well. In the trap-free SCL regime, the numerical curves show less current and smaller slope than do the simplified ones, because series resistance in the n-layers is included in the numerical calculations but not
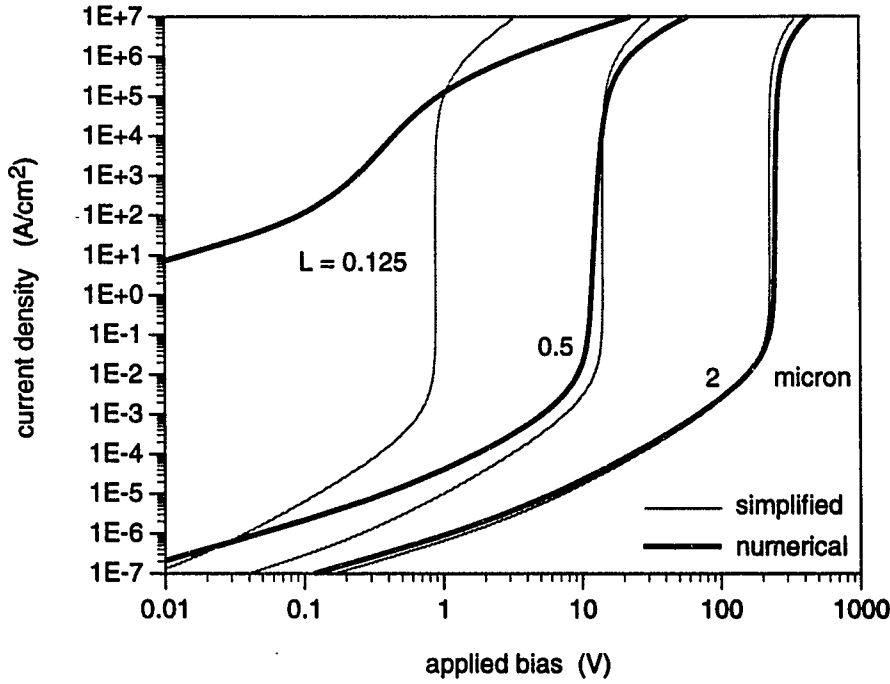
Figure 4.3:   Two-carrier drift-diffusion J-V characteristics from simplified theory and from numerical model, assuming constant carrier mobilities ($\mu_n =$ 2000 cm^2/V-s), for $L = 0.125$, 0.5, and 2 μm. $N_t = 8 \times 10^{16}$ cm^{-3}.

in the simplified ones.) As we would expect, the most significant effects of including diffusion (as compared with the simplified model) are seen for thin layers. As we saw in Figure 4.2, in a thin layer the bandbending from the interfaces can result in a concentration of initially empty traps that is lower than the bulk equilibrium value p_{t_0} across the entire layer. This increases the concentration of thermal electrons above its bulk value n_0, leading to larger current in the ohmic regime and narrowing or obliterating the shallow-trap SCL regime. Also, the inclusion of contact effects causes the TFL regime to be spread out over a wider voltage range than in the simplified theory. This result can be understood in terms of the shift in the position of the cathode barrier with increasing bias, as illustrated for a 0.5-μm case in Figure 4.4. The effective thickness of the SI layer increases with increasing bias as the plane of zero electric field moves toward the cathode interface.
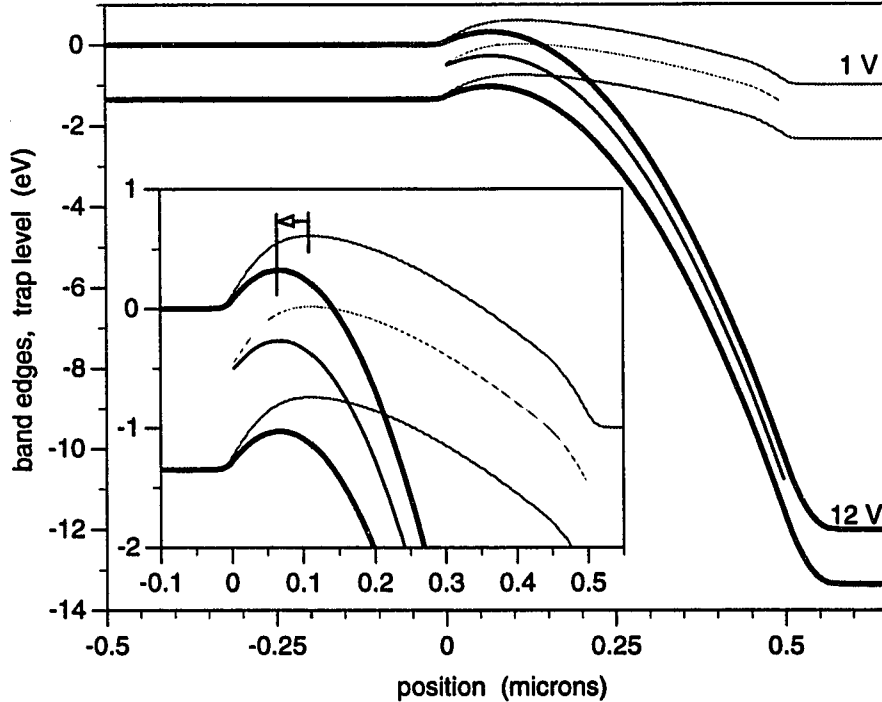
Figure 4.4: Band diagrams for 0.5-μm layer operating at 1 V and 12 V bias, showing junction effects. Shift in position of cathode barrier with increasing bias is readily seen in inset. $N_t = 8 \times 10^{16}$ cm^{-3}. (The trap level is included in the diagram to help indicate the spatial extent of the SI layer.)

The lower the trap density in the SI layer, or the larger the background donor concentration, the more pronounced are all of these effects.

In cases for which bandbending in the SI layer at the interfaces is important, the donor concentration in the n-type contact layers is also important. In Chapters 4 and 5 we have used $N_d = 5 \times 10^{17}$ cm^{-3} in the contact layers. (Calculations using other contact-doping levels are shown in Chapters 6 and 7.) Notice in Figure 4.4 that a significant portion of the total voltage can be dropped across the depletion layer in the anode contact; for a given overall bias, this reduces the potential drop across the SI layer, shifting the trap-filled limit to higher bias. Bandbending in the anode n-layer thus has the opposite effect on V_{TFL} from that of bandbending on the cathode side of the SI layer;

depending on doping levels, the resulting value of V_{TFL} can be either larger or smaller than that predicted by the simplified theory.

Since the value of V_{TFL} for thin layers depends strongly on the behavior at the interfaces, the performance of thin layers cannot reliably be predicted by extrapolating to smaller thicknesses the quadratic fits of V_{TFL} vs. L obtained from thicker samples (as, for example, in [21]). Also, the J-V characteristics of a thin Fe-doped layer are not usefully described by a bulk resistivity, even in the ohmic regime. Rather, the behavior of a thin Fe:InP layer in an n-SI-n configuration is a property of the structure as a whole. The numerical model allows us to treat it as such, and indicates that even for trap densities on the order of the solubility limit, very thin Fe:InP layers are ineffective for current blocking.

4.3   Nonlinear velocity-field relations

The drift-diffusion solution as described above is valid in regimes for which the carrier mobility μ_n can be assumed constant, that is for fields up to a few kV/cm in InP. At higher fields, however, the velocity-field characteristic for InP is nonlinear, exhibiting velocity saturation and negative differential mobility. For most cases—e.g. $V \geq 1$ V for a 2-μm layer—a realistic model must therefore include the effects of these nonlinearities.

To show the effects of the various features of the velocity-field characteristic on the behavior of our structure, we consider three different forms for $v(E)$, as shown in Figure 4.5. The first of these is a linear characteristic described by $v = \mu_0 E$, where μ_0 is independent of the field. The second is simple velocity saturation, in which $v(E)$ is a monotonically increasing function that never exceeds the saturation velocity v_{sn}. The third is a more realistic form that includes negative differential mobility and approaches v_{sn} for large fields. The figure also shows a Monte Carlo calculation taken from Sadra *et al.* [36]. For historical reasons, we are using a fit to this Monte Carlo to represent our "realistic" $v(E)$ curve in the calculations of Chapters 4 and 5.

The linear $v(E)$ characteristic is the one we have been using so far, in the development of the simplified theory in Chapter 3 and in the calculations in Section 4.2. Before taking up the realistic $v(E)$ characteristic with negative differential mobility (below, p. 49), we first consider what happens when we simply allow the drift velocity to saturate.

To start, we return to the phenomenological treatment of the J-V charac-
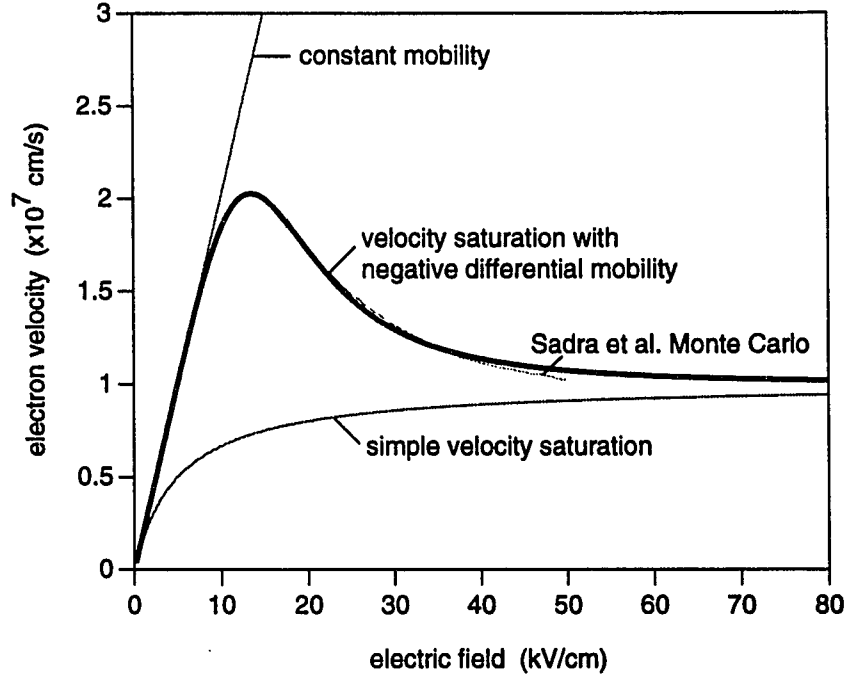
Figure 4.5: Velocity-field characteristics in numerical model: (i) constant mobility; (ii) simple velocity saturation; (iii) with negative differential mobility. Also shown are Monte Carlo results from Sadra *et al.* [36, Figure 8, for majority electrons with polar phonon interaction unscreened].

teristic for the SCL regime, but now instead of a constant carrier mobility we assume a constant carrier velocity. Recall that the square-law form (3.3) of the J-V curve in the SCL regime was derived under the assumption of constant mobility, and depends on the relation $n(x) \sim 1/E(x)$ (from $J = nq\mu_0 E =$ constant). If we have instead a constant carrier velocity v_{sn}, then $n(x) \sim 1/v_{sn} =$ constant (from $J = qnv_{sn} =$ constant), and we find for the J-V characteristic in the shallow-trap SCL regime

$$J = 2\theta\epsilon v_{sn}V/L^2 \tag{4.6}$$

where θ is again the ratio of the concentrations of free and trapped electrons. Thus, if the carrier velocity is constant, the J-V relation is linear in the shallow-trap SCL regime. Note that in general a square-law J-V relation is not an
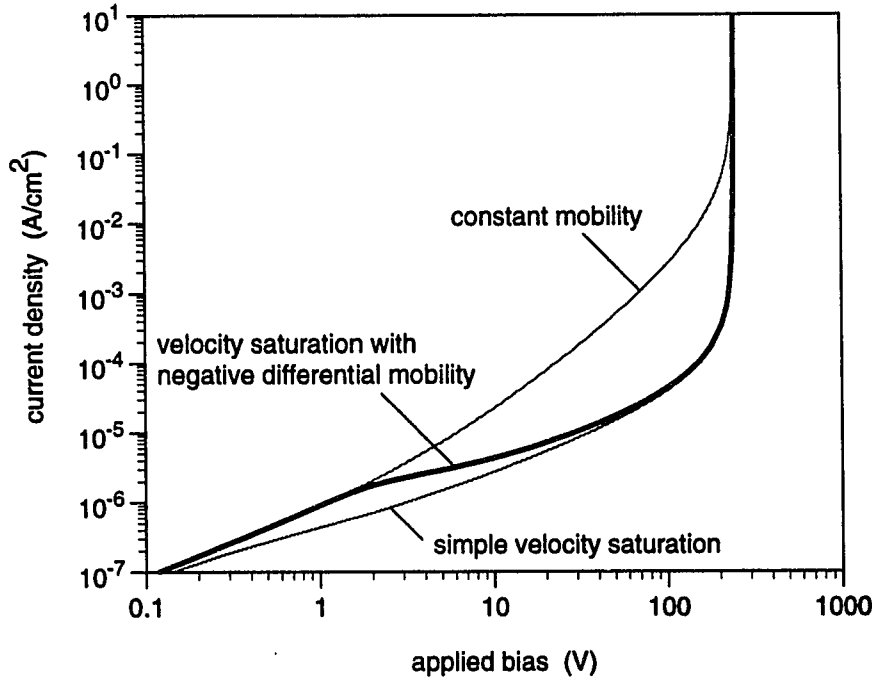
Figure 4.6: J-V characteristics for 2-μm layer: (i) constant-mobility; (ii) simple velocity saturation; (iii) velocity saturation with negative differential mobility. $N_t = 8 \times 10^{16}$ cm^{-3}.

inherent signature of SCL conduction if the carrier mobility is not constant, that is, if the velocity-field relation is nonlinear.

The phenomenological treatment with drift velocity saturation is relatively straightforward. Depending on the functional form of the velocity-field relation, analytic solutions to the full simplified problem (as discussed in Section 3.2 above) can also be obtained. Interested readers are referred to the work of Lampert and Rose [37].

In the numerical model, various forms for $v(E)$—or, equivalently, $\mu(E)$—can be assumed. For simple velocity saturation, we use two-section velocity-field characteristics as described by

$$\mu_{(n,p)} = \frac{\mu_{(n,p)0}}{1 + \mu_{(n,p)0}|E|/v_{s(n,p)}} \equiv \frac{\mu_{(n,p)0}}{1 + |E|/E_{s(n,p)}} \, , \tag{4.7}$$

that is,

$$\frac{1}{v_{(n,p)}} = \frac{1}{\mu_{(n,p)0}E} \pm \frac{1}{v_{s(n,p)}} \qquad (4.8)$$

where the sign of the second term is that of the field E. The electron and hole saturation velocities (v_{sn}, v_{sp}) are 1×10^7 and 8×10^6 cm/s respectively. For the low-field mobilities (μ_{n_0}, μ_{p_0}) we use 2000 and 400 cm^2/V-s respectively, the same values as were used in the constant-mobility calculations of Section 4.2. A plot of $v(E)$ from (4.8) using these numbers appears in Figure 4.5.

Numerical results illustrating the effects of simple velocity saturation by comparison with the constant-mobility case are shown in Figures 4.6 and 4.7 for a 2-μm layer. (We also show the effects of a $v(E)$ characteristic with negative differential mobility, which is discussed below.) Recall that the J-V characteristic under the assumption of constant mobility was quadratic in the shallow-trap SCL regime. By contrast, the J-V characteristic calculated with velocity saturation (Figure 4.6) is nearly linear in the shallow-trap SCL regime. This can be understood on the basis of the phenomenological approximation, as discussed above, and is the result of the more uniform charge distribution which obtains in the presence of velocity saturation (see Figure 4.7).

The above discussion assumes monotonic velocity-field relations as described by (4.7–4.8) for both electrons and holes. It is well known, however, that electrons in InP exhibit negative differential mobility. We can include this effect by instead using

$$\mu_n = \mu_{n_0} \frac{1 + \left(\dfrac{v_{sn}}{\mu_{n_0}|E|}\right)\left(\dfrac{E}{E_0}\right)^4}{1 + \left(\dfrac{E}{E_0}\right)^4} \qquad (4.9)$$

for the electrons. This form is taken from Horio *et al.* [28]; it is equivalent to

$$v_n = \frac{\mu_{n_0}E \pm v_{sn}(E/E_0)^4}{1 + (E/E_0)^4} , \qquad (4.10)$$

which is plotted in Figure 4.5. Here again the sign of the second term is that of E, and we have used $E_0 = 1.5 \times 10^4$ V/cm to conform to the results of Sadra *et al.* [36]. (This form still assumes that the electron velocity approaches a constant value for very large fields, beyond the range shown in [36].) The J-V characteristic that results from using this form for our 2-μm layer is plotted

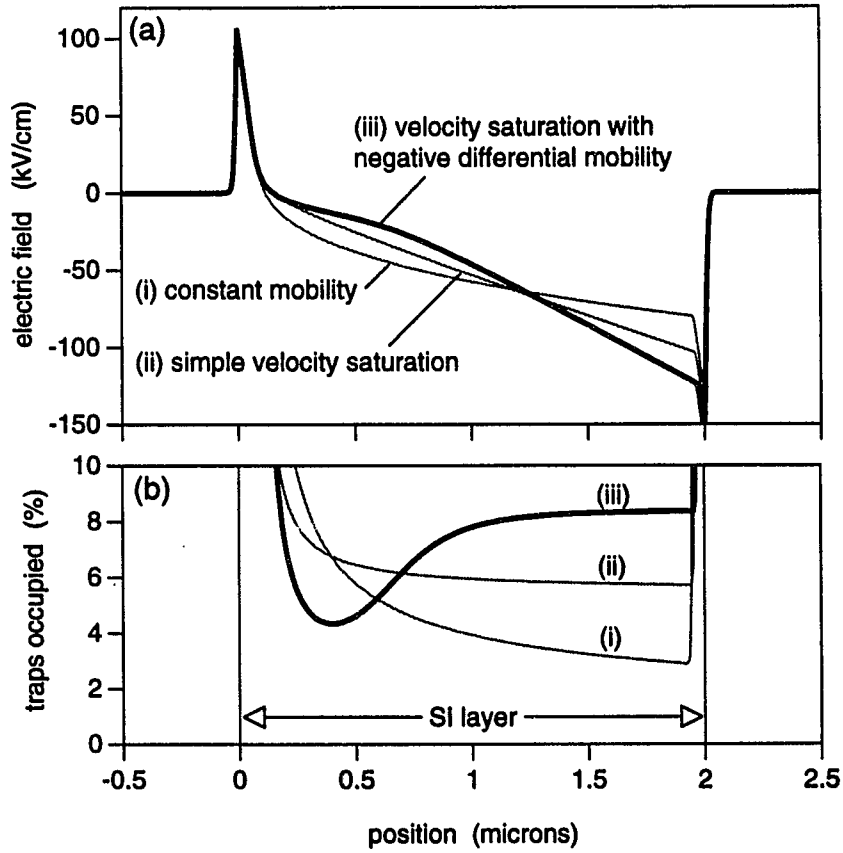Figure 4.7:   Spatial variation of (a) electric field and (b) occupied traps, for 2-μm layer operating at 10 V. (i) constant-mobility; (ii) simple velocity saturation; (iii) velocity saturation with negative differential mobility. $N_t = 8 \times 10^{16}$ cm^{-3}.

as the dark line in Figure 4.6. Since the electron velocity now undergoes a transition from a constant-mobility regime to a constant-velocity regime, it is not surprising that the predicted *J-V* characteristic also shows a transition from constant-mobility to constant-velocity behavior as we increase the bias level.

For large biases, the electron velocity will now be larger in the region of low electric field near the cathode than in the rest of the structure. For steady-state current continuity, the free electron concentration near the cathode must therefore be smaller. The reduction in n is accompanied by a reduction in n_t in the vicinity of the cathode, as shown in Figure 4.7b. Note that the peak field is larger in the presence of a negative differential mobility than it would be with simple velocity saturation.

As we saw in Figure 4.6, the inclusion of negative differential mobility introduces a sublinear regime in the *J-V* characteristics. This effect is most pronounced for thicker layers; in some cases we predict an almost constant current density over a wide voltage range, as shown in Figure 4.8.

Sublinear SCL behavior has recently been observed in low-temperature-grown (LT) GaAs [38]. The typical measured *J-V* curve in Fe:InP, however, exhibits a regime of superlinear behavior below the steep rise in current; the near-linear and sublinear *J-V* curves shown in Figure 4.6 do not in general agree with our experiments. The superlinearity in the experimental curves can be a trap-filling effect, if the actual trap densities are substantially lower than that assumed in this calculation; that is, on the basis of the model so far, we expect a linear *J-V* curve in the saturated-velocity SCL regime only so long as the ratio θ remains constant. If the trap density is small, the shallow-trap approximation fails at relatively low bias, and θ (and therefore dJ/dV) starts to increase with bias. On the other hand, if the assumed (large) trap density is accurate, then the lack of agreement indicates that some other process is operating. One possibility, field emission from the traps, is discussed in Section 4.4 below.

Another possibility is that the low-field mobility is so small that the saturated drift velocity is not attained in the SCL regime. Our experimental results suggest that this might indeed be the case in our material. We reach this hypothesis, however, on the basis of knowing what the effects would be if the mobility were larger, so for the purposes of this chapter and the next we continue to use the larger values in order to illustrate those effects.
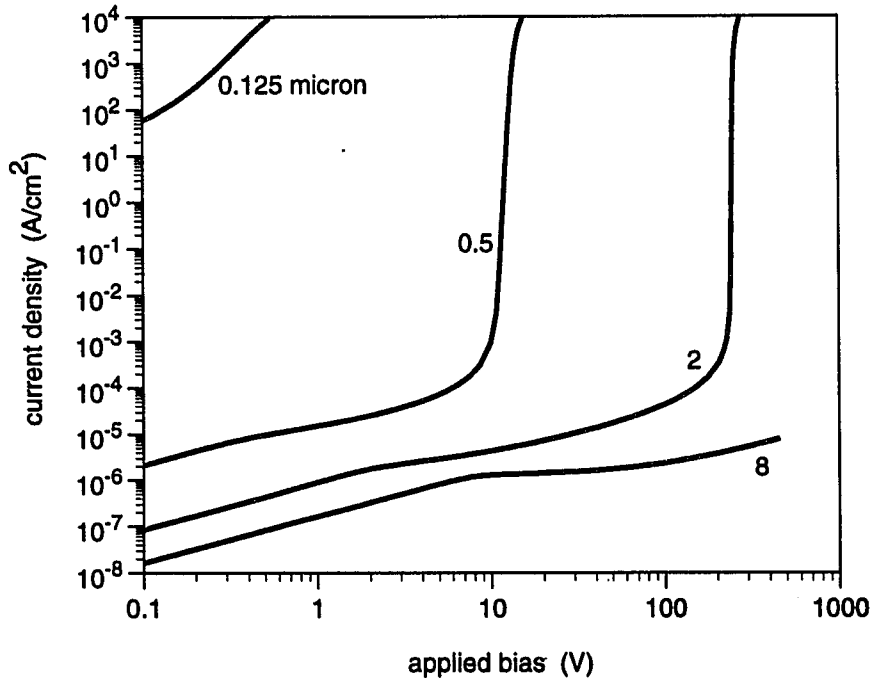
Figure 4.8: J-V characteristics with negative differential mobility, for $L =$ 0.125, 0.5, 2, and 8 μm. $N_t = 8 \times 10^{16}$ cm^{-3}.

4.4   Field emission from traps

The fields in our structures are high enough that we must include drift velocity saturation and negative differential mobility, for which we would expect (assuming a large trap density and a typical low-field mobility) a linear or sublinear J-V characteristic in the SCL regime. Measurements, however, typically show superlinear behavior. One possible source of this discrepancy is field emission from traps. A related mechanism has been previously proposed to explain the quadratic J-V regime of operation [23]. In order to examine this effect, we must lift the assumption of quasi-thermal equilibrium between trapped and free electrons; that is, the concentration of trapped electrons can no longer be assumed to be uniquely specified by the concentration of free electrons as in (2.8). We need a new occupation function for the trap.
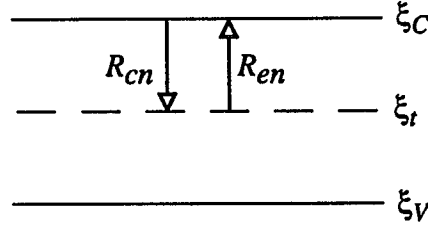
Figure 4.9: Electron capture and emission processes.

To establish a method for obtaining the new occupation function, let us first review how we got the old one. In writing (2.8), we have simply taken the equilibrium occupation function (2.1) for the trap, as given by Fermi-Dirac statistics, and used the assumption of quasi-thermal equilibrium to plug into it a quasi-Fermi level derived from the free electron concentration. This "method" glosses over some key assumptions, however; it is really a shorthand for what we do when we consider the capture and emission processes that populate and depopulate the traps.

Textbooks usually discuss these processes in connection with Shockley-Read-Hall recombination, so that capture and emission of holes as well as capture and emission of electrons are considered. For now, however, we continue to assume that there is no recombination through these traps, so that we only need consider two processes, as shown in Figure 4.9. Capture of electrons from the conduction band occurs with rate R_{cn}, which is the product of the number of available (i.e. free) electrons n and the probability per unit time that one of them will be captured, c_n. The probability c_n is in turn the product of the probability that an electron will intercept a trap—which we can write as $\sigma_{cn} v_{th_n} N_t$, where σ_{cn} is the effective cross section for electron capture—and the probability $(1 - f_t)$ that said trap will be empty. (Here f_t is the occupation function we are trying to derive.) The total capture rate is thus $R_{cn} = \sigma_{cn} v_{th_n} N_t (1 - f_t) n$.

Emission of electrons to the conduction band occurs with rate R_{en}, which is the product of the number of trapped electrons $f_t N_t$ and the probability per unit time that one of them will be emitted, e_n. It is in the evaluation of e_n that we make the assumptions that lead to (2.8).

In steady state, the number of trapped electrons must be constant, so

the total capture rate must equal the total emission rate. Equating $R_{cn} = \sigma_{cn} v_{th_n} N_t (1 - f_t) n$ with $R_{en} = e_n N_t f_t$ gives

$$f_t = \frac{1}{1 + e_n/(\sigma_{cn} v_{th_n} n)} \ . \tag{4.11}$$

This can be inverted to give an expression for e_n in terms of n and f_t. Since we know both n and f_t at thermal equilibrium, we can evaluate e_n at thermal equilibrium as follows:

$$e_n = \sigma_{cn} v_{th_n} \left(\frac{1 - f_{t_0}}{f_{t_0}} \right) n_0 \equiv \sigma_{cn} v_{th_n} g n_1. \tag{4.12}$$

Here f_{t_0} is the equilibrium occupation probability for the trap, n_0 is the equilibrium concentration of free electrons, g is the degeneracy factor for the trap as defined in (2.1), and $n_1 \equiv N_C \exp[-(\xi_C - \xi_t)/kT]$ as usual. The second equivalence in (4.12) depends on the use of a single quasi-Fermi level for n_0 and f_{t_0}.

We then assume that e_n remains unaffected by non-equilibrium conditions. That is, for quasi-equilibrium we substitute (4.12) into (4.11) to obtain

$$f_t = \frac{1}{1 + g n_1/n} \ , \tag{4.13}$$

as in (2.8).

Now the premise of field emission from the traps is that the emission probability e_n does not remain constant, but increases in the presence of an electric field. The reason for this can be seen in Figure 4.10, in which we schematically represent the potential well due to the trap as a one-dimensional Coulomb potential, with and without an applied field. In the presence of the field, the energy needed to remove the electron from the well (by emission over the barrier, in the positive z direction) is reduced by an amount $\Delta\xi_a(E)$ with respect to the zero-field case. This is referred to as Poole-Frenkel barrier-lowering [39].

As suggested by Karl Hess, we have used expressions for the barrier-lowering taken from Martin *et al.* [39] and have treated field emission by assuming that the capture cross section σ_{cn} stays constant but that the emission probability e_n depends on the local field as

$$e_n = \sigma_{cn} v_{th_n} g n_1 \cdot \exp[\Delta\xi_a(E)/kT] \ . \tag{4.14}$$
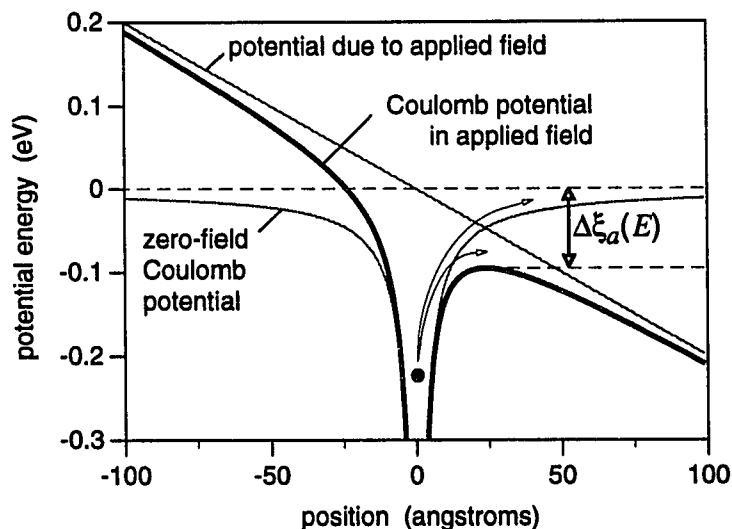
Figure 4.10: 1-D Coulomb potential with applied field.

This is equivalent to lowering the ionization energy $\xi_C - \xi_t$ of the trap by an amount $\Delta\xi_a(E)$, and results in a field-dependent quasi-Fermi level for the trap that differs from the quasi-Fermi level for free electrons by $\Delta\xi_a(E)$. Formally, we multiply n_1 in (4.13) by the factor $\exp[\Delta\xi_a(E)/kT]$; the occupation function thus becomes

$$f_t = \frac{1}{1 + (gn_1 \exp[\Delta\xi_a(E)/kT])/n} \cdot \qquad (4.15)$$

(So far, we have not included recombination through the traps. As shown in Section 5.1, such recombination also introduces a change in the occupation function. To include both field emission and recombination, we multiply n_1 by $\exp[\Delta\xi_a(E)/kT]$ in both (5.5) and (5.6).)

The change in activation energy $\Delta\xi_a(E)$ for a given field of course depends on the nature of the potential associated with the trap. We don't know a priori what kind of potential to assume, so we have experimented with three varieties. For the 1-D Coulomb potential shown in Figure 4.10, the functional form of the barrier-lowering $\Delta\xi_a(E)$ is derived in Appendix E. We also tried assuming a more realistic 3-D Coulomb potential and a 3-D square well. Functional forms for the field-dependent change in emission rate for the two 3-D potentials were
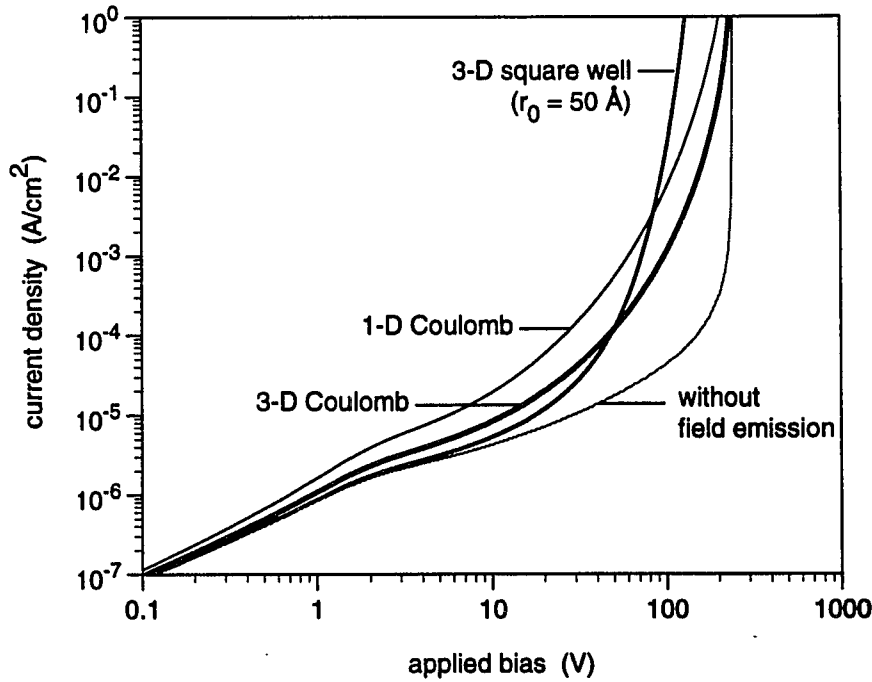
Figure 4.11: *J-V* characteristics for 2-μm layer including velocity saturation with negative differential mobility and field emission from traps, using (i) 3-D square well potential with radius $r_0 = 50$ Å; (ii) 1-D Coulomb potential; (iii) 3-D Coulomb potential.

taken from the work of Martin *et al.* [39] and are reproduced in Appendix E. *J-V* curves for a 2-μm layer, assuming in turn each of the three types of potential, are shown in Figure 4.11. The situation in the absence of field emission is also shown for comparison. All of these curves include nonlinear velocity-field relations (4.9–4.10) as used for Figure 4.8.

Notice that a quadratic *J-V* regime can indeed be an SCL regime, in which the quadratic *J-V* behavior is due not to the usual SCL square law, but to the linear SCL law with velocity saturation, in combination with field emission. The reason for this can be seen in the electric field and occupied trap distributions, illustrated for the 2-μm case in Figure 4.12. The effect of velocity saturation was to make the charge distribution more uniform (compared to the constant-mobility case), and thus to make the field distribution more nearly
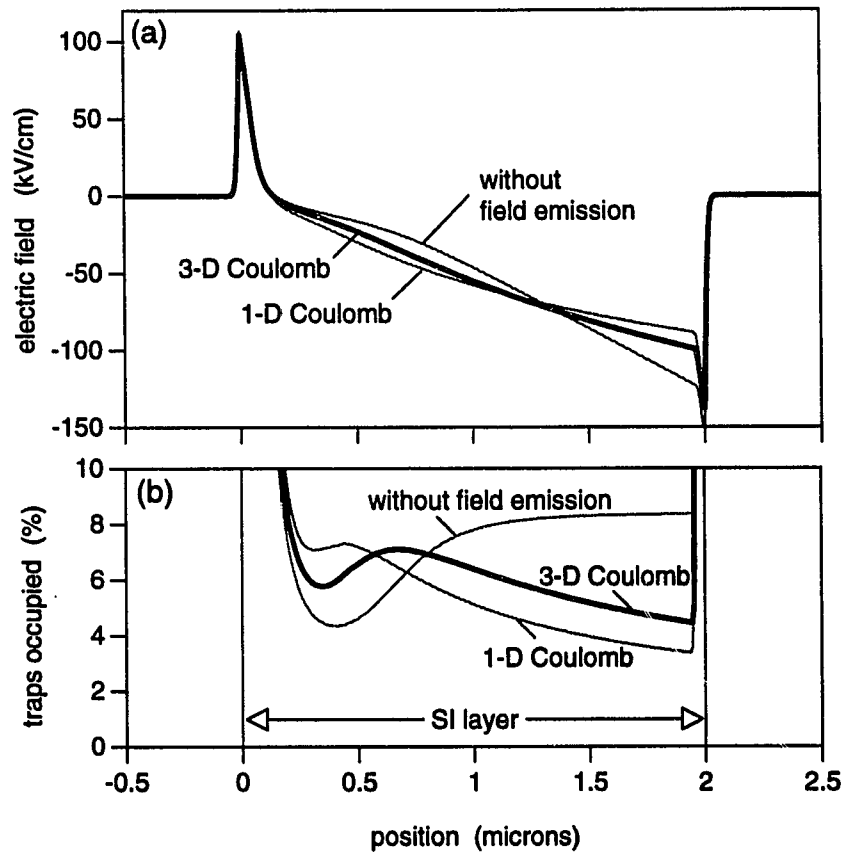
Figure 4.12:   Spatial variation of (a) electric field and (b) occupied traps, for 2-μm layer operating at 10 V, including velocity saturation with negative differential mobility and field emission from traps (using 1-D and 3-D Coulomb potentials). Compare constant-mobility distributions in Figure 4.7.

triangular (as we saw in Figure 4.7). Since field emission reduces the amount of trapped charge in the high-field region, the effect of including field emission in the model is to push the charge and field distributions back toward the forms they would have had in the simplified, constant-mobility model.

As we will see in Chapter 6, if we allow the carrier velocity to saturate (as we do in Figure 4.11), none of the three flavors of field emission considered here gives particularly good agreement with the shapes of our experimental *I-V* curves. This may indicate that other processes are operating, or that the low-field mobility is small enough that the velocity does not in fact saturate. In any case, because it is not clear whether we need to include field emission, or if so, in what form we should include it, and because the calculations are more time-consuming if we do include it, we have not included field emission in the calculations for Chapter 5. Knowing the effects that field emission would have on our field and trapped-carrier distributions allows us to estimate what would happen if we did include it; we also show in Section 6.1 a calculation of critical voltage as a function of layer thickness, in which we include field emission from a 3-D Coulomb potential as well as all of the two-carrier effects from Chapter 5.

In this chapter we have introduced holes into the problem, without commenting on their effects. In the next chapter we will examine the free carrier concentrations and see that, in the absence of a generation mechanism such as impact ionization, the hole population is small and has a negligible effect on the field and trapped-carrier profiles shown in the present chapter. As we shall see, even Shockley-Read-Hall generation/recombination through the traps, by itself, would have little effect on the *J-V* characteristics developed here.

So far, we have examined the spatial distribution of trapped electrons in the SI layer and shown how it is affected by diffusion from the contacts, by nonlinear velocity-field relations, and by field emission from the traps. We have also seen how these effects would manifest themselves in the *J-V* characteristics. In the next chapter we look at how things change under the influence of various two-carrier processes.

Chapter 5

Avalanche injection and two-carrier effects

In the previous chapter, we examined various effects in the context of a single-carrier injection problem. None of these explains the destructive breakdown that we observe experimentally. In this chapter, we turn to two-carrier effects, and examine the results of including several generation/recombination mechanisms in the model. We show that Shockley-Read-Hall recombination/generation alone, whether through a low concentration of unspecified, unintentional midgap centers or through our Fe traps themselves, has a negligible effect on the J-V characteristics. We then examine the consequences of carrier generation by band-to-band impact ionization. We show that in the presence of such generation the holes are very important, so that SRH recombination through the traps or radiative recombination can be significant. The holes participate in a positive feedback mechanism for avalanche breakdown. Unlike the critical behavior due to trap filling, this breakdown is indeed destructive, and it can occur at bias levels well below the trap-filled limit.

5.1 Shockley-Read-Hall generation/recombination

Shockley-Read-Hall (SRH) generation/recombination can occur through intentionally-introduced traps (Fe in our case) as well as through unintentional defects. For intentional traps, we keep track of the charge on the recombination centers and include that in the Poisson equation, and we characterize the centers by electron and hole capture cross sections. For unintentional defects, since we do not know the nature of the defects and since there are few enough
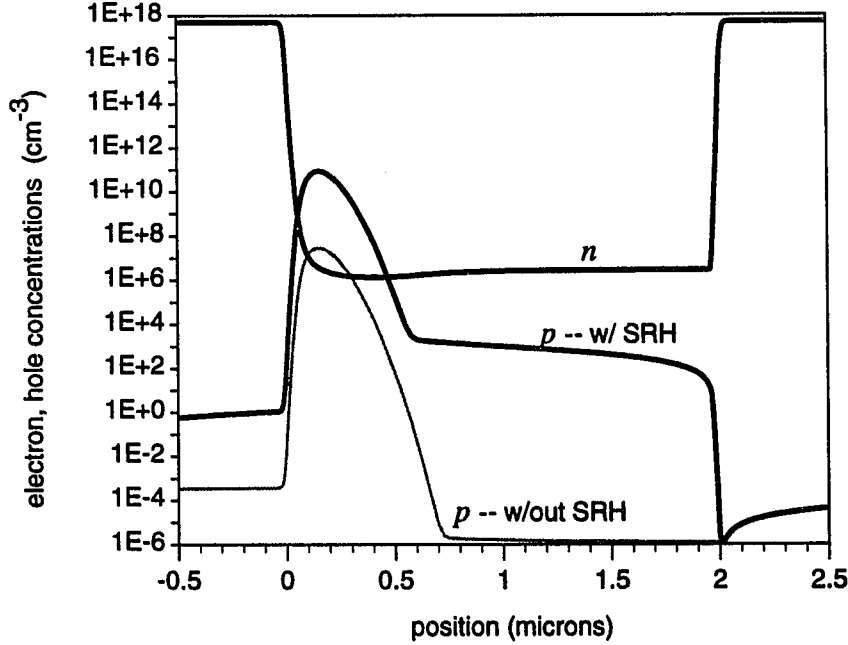
Figure 5.1:   Carrier concentrations for 2-μm layer operating at 10 V, with and without background SRH generation/recombination. Includes velocity saturation and negative differential mobility.

of them that their contribution to the net space charge can be neglected, we assume a midgap level and characterize the recombination rate phenomenologically by two time constants, τ_{n_0} and τ_{p_0}, as in (5.1).

Background SRH generation/recombination. To start, we assume that the only generation/recombination mechanism is SRH processes through unintentional defects. We include this by setting $R = R_0$ throughout the structure, where

$$R_0 = \frac{np - n_i^2}{\tau_{p_0}(n + n_i) + \tau_{n_0}(p + n_i)}.$$ (5.1)

(As the R suggests, this is written as a recombination rate. If $np < n_i^2$, we have $R_0 < 0$, that is, generation of carriers.) This is a standard expression for SRH recombination, commonly found in textbooks. It assumes a nonde-

generate state located at the intrinsic level ξ_i, and is thus a special case of the more general expression used below to treat recombination through the Fe traps. (We provide a derivation below, in connection with the more general expression.) For typical InP quality, we take $\tau_{n_0} = \tau_{p_0} = 10^{-7}$ s.

The effect of including this mechanism is to increase the hole population in the SI layer, in a manner completely analogous to that in the depletion region of a *p-n* junction. (The latter is discussed in Appendix F.) Carrier concentration profiles calculated with and without SRH generation/recombination are shown in Figure 5.1. The change in the hole concentration due to SRH processes can be many orders of magnitude, but the number of holes is still small enough that this change has a negligible effect on the field and trapped-carrier profiles as calculated in Chapter 4.

That the additional holes have a negligible effect on the *J-V* characteristics is illustrated in Figure 5.2, in which we show both the total current $J = J_n + J_p$ and the hole current J_p, as functions of applied bias, in three different planes of the structure. The calculation is for the same case as the 2-μm curve shown in Figure 4.8, except for the addition of the background SRH mechanism. The hole currents shown are those in the planes of the two junctions and in the center of the SI layer. It is evident that the hole current constitutes a very small contribution to the total. (Without the SRH term R_0, the hole currents in all three planes would be below 1×10^{-14} A/cm^2.)

The plateau in $p(x)$ under SRH generation seen in Figure 5.1 is similar in origin to the carrier plateaus shown in Figure F.1 for a reverse-biased *p-n* junction. The abrupt rise in the hole current in the anode junction (Figure 5.2) corresponds to the depletion of the diffused carriers from the space-charge region at the junction, and thus to the arrival at the junction plane of the generation-induced carrier plateau edge.

We have assumed that we can neglect any space charge due to carriers trapped at unintentional defects. We cannot of course neglect the space charge due to carriers trapped at our Fe centers, so we must treat recombination through these centers separately:

SRH generation/recombination through traps. In the simplified theory and in the numerical analysis of Chapter 4, we assumed that the trapped electrons were in quasi-thermal equilibrium with the free electrons, which is equivalent to assuming that Fe in InP acts purely as an electron trap and that no recombination takes place through the Fe level. A number of experiments, however, indicate that Fe in InP is a recombination center as well as an electron
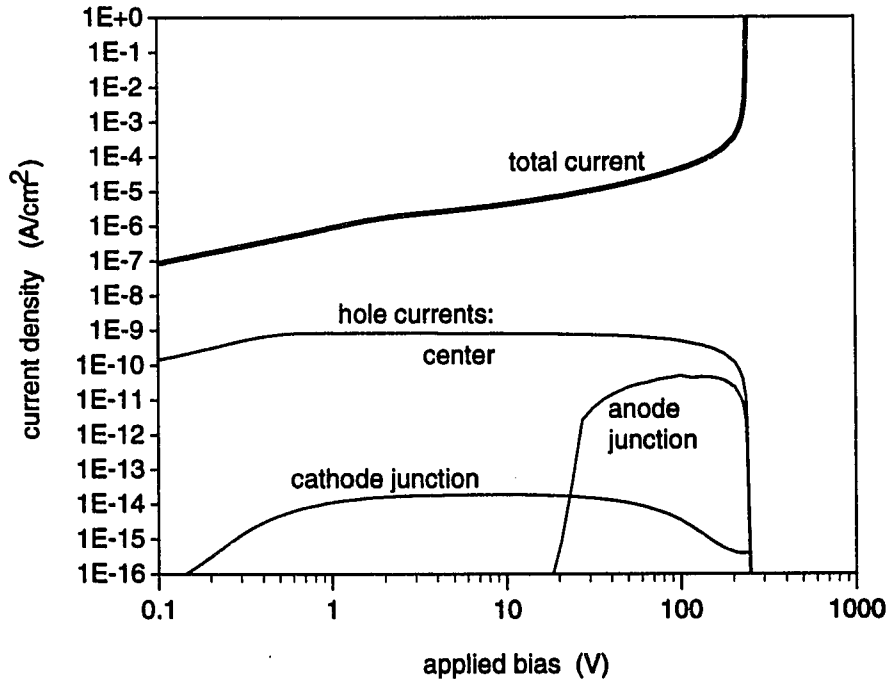
Figure 5.2:   *J-V* characteristic from numerical model, including background SRH generation/recombination, showing total current as well as hole currents at planes of metallurgical junctions and at center of SI layer. At the plane of the cathode junction ($x = 0$ in Figure 5.1), most of the holes generated in the body of the SI layer have already recombined.

trap, so we need to allow for SRH processes through this level.

In our discussion of field emission in Section 4.4, we lifted the assumption of quasi-thermal equilibrium between trapped and free electrons, so that the concentration of trapped electrons became a function of the electric field as well as of the concentration of free electrons. In that situation, we considered only capture of electrons from the conduction band and emission of electrons to the conduction band. We included field emission solely by modifying the occupation function for the trap.

In the case of recombination through the trap, we must account for capture and emission processes involving the valence band as well as those involving the conduction band, as indicated in Figure 5.3. This results in modifications
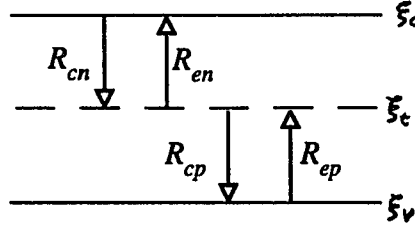
Figure 5.3: Electron and hole capture and emission processes. Arrows show direction of electron transitions.

both to the occupation function and to the recombination rate R.

The derivation of the occupation function follows the same method as in Section 4.4, but we now have to invoke the principle of detailed balance in the evaluation of the emission probabilities. The electron capture and emission rates are still given by $R_{cn} = \sigma_{cn} v_{th_n} N_t (1 - f_t) n$ and $R_{en} = e_n N_t f_t$. From analogous arguments, the hole capture and emission rates are $R_{cp} = \sigma_{cp} v_{th_p} N_t f_t p$ and $R_{ep} = e_p N_t (1 - f_t)$. Here σ_{cp} is the cross section for hole capture, e_p is the probability per unit time that an unoccupied trap will emit a hole, and f_t is as usual the probability that a trap is occupied by an electron. (By hole emission we mean the transition of an electron from the valence band into the trap, leaving behind a hole in the valence band. Hole capture is the reverse process.) For steady state operation, we demand that the population of the trap level be constant, so that $R_{cn} + R_{ep} = R_{en} + R_{cp}$. That is, the rate at which electrons enter the traps must equal the rate at which they leave. Using our expressions for the four rates, we find

$$f_t = \frac{1}{1 + \dfrac{\sigma_{cp} v_{th_p} p + e_n}{\sigma_{cn} v_{th_n} n + e_p}} \cdot \qquad (5.2)$$

Once again, we evaluate the emission probabilities under thermal equilibrium conditions, and then assume that they remain constant. In equilibrium, the rates of hole capture and emission must equal each other, just as the rates of electron capture and emission must equal each other, and the carrier concentrations and occupation function are known. We saw in (4.11– 4.12) how

equating R_{cn} with R_{en} enabled us to evaluate e_n in terms of σ_{cn}:

$$e_n = \sigma_{cn} v_{th_n} \left(\frac{1 - f_{t_0}}{f_{t_0}} \right) n_0 \equiv \sigma_{cn} v_{th_n} g n_1. \tag{5.3}$$

Similarly, equating R_{cp} with R_{ep} allows us to evaluate e_p in terms of σ_{cp}:

$$e_p = \sigma_{cp} v_{th_p} \left(\frac{f_{t_0}}{1 - f_{t_0}} \right) p_0 \equiv \sigma_{cp} v_{th_p} p_1 / g. \tag{5.4}$$

Here the constants n_1 and $p_1 = n_i^2/n_1$ represent the electron and hole concentrations, respectively, that would be present in equilibrium if the Fermi level coincided with the trap level.

Using (5.3) and (5.4) to eliminate e_n and e_p from (5.2), we find that the occupation function for the trap level becomes

$$f_t = \frac{\sigma_{cn} v_{th_n} n + \sigma_{cp} v_{th_p} (p_1/g)}{\sigma_{cp} v_{th_p} (p + p_1/g) + \sigma_{cn} v_{th_n} (n + g n_1)} \tag{5.5}$$

where as usual $n_t = f_t N_t$. This expression gives the steady-state occupation probability for a recombination center or trap state whose degeneracy factor is g and whose energy level is contained in the constant n_1.

Taking the hole capture cross section σ_{cp} as zero corresponds to the assumption of quasi-thermal equilibrium between the trapped electrons and those in the conduction band, so that (5.5) reduces to (4.13). Allowing the hole capture cross section to be non-zero also allows recombination/generation through the trap level, with rate

$$R_t = R_{cn} - R_{en} = \frac{np - n_1 p_1}{\tau_{p_t}(n + g n_1) + \tau_{n_t}(p + p_1/g)} \tag{5.6}$$

where

$$\tau_{(n,p)_t} \equiv 1/\sigma_{c(n,p)} v_{th_{(n,p)}} N_t. \tag{5.7}$$

(If we have a nondegenerate state located at the intrinsic level, then $g = 1$ and $n_1 = p_1 = n_i$, and we recover the expression (5.1) used above for recombination through unintentional defects.)

In our case, we have recombination through Fe traps as well as through unintentional defects. We therefore add the recombination rate through the traps, as given by (5.6), to the background SRH rate given by (5.1). The total SRH recombination/generation rate in the SI layer becomes $R = R_0 + R_t$.

The importance of recombination through the trap level depends on the sizes of the capture cross sections for electrons and holes. The condition for no recombination/generation through the trap corresponds either to a negligible hole population or to a zero hole capture cross section. For this work, we have taken the cross sections as 3×10^{-15} cm^2 for electrons and 1×10^{-16} cm^2 for holes; these values are taken from [26]. Considering the values of electron and hole capture cross sections reported for various traps in III-V semiconductors [40], it is unlikely that the hole capture cross section would ever be identically zero, which means that for an electron trap the condition for quasi-equilibrium between free and trapped electrons reduces to a condition on the hole population: for quasi-equilibrium among the electrons, the hole population must be negligible.

If the hole population is finite, then when we allow recombination through the trap level we find some redistribution of the hole population, with an accompanying slight redistribution of the the trapped charge and of the field. In the vicinity of the cathode barrier, where the hole population is largest, we have an increased recombination rate and a decrease in the hole population compared to the quasi-equilibrium case. In the body of the SI layer, where both free electrons and holes are scarce, we have an increased generation rate and an increase in the hole population compared to the quasi-equilibrium case. However, since the hole populations remain small, the effect on the total current is negligible. For example, for a 2-μm layer with $N_t = 8 \times 10^{16}$ cm^{-3} operating at 10 V (and using the cross sections given above), the effect of allowing recombination/generation through the traps is to lower the hole population at the cathode barrier by two orders of magnitude and to increase the hole population in the body of the SI layer by about one order of magnitude. The result is to increase the hole current in the SI layer by one order of magnitude in the SCL regime of operation, but since the hole current constitutes an insignificant contribution to the total current, the effect on the total current is negligible. (The effect is slightly more pronounced in the ohmic regime of operation, where the electron current is lower and the hole current more important.) The change in the hole currents at the center and junction planes can be seen by comparing Figure 5.2 with the thin lines in Figure 5.5.

Thus, in the cases so far considered, we have been justified in viewing current injection in an n-SI-n structure as an electron injection problem; the hole populations have been small enough so as not to change the essential character of the problem. If the hole population becomes large, however— whether through injection directly from a p-layer, leaking across an inadequate

n-layer, optical pumping, or avalanche injection—recombination through the trap level can be significant, and the resulting change in the trapped carrier concentration can be large. We turn now to a situation in which the holes play a crucial role in determining the J-V characteristics of the structure.

5.2 Impact ionization

The models described above all attribute the steep rise in current vs. voltage for an n-SI-n structure to trap filling in the SI layer, so that complete filling of the traps corresponds to the center of the TFL regime. However, other mechanisms can be responsible for such a steep rise in current. As we have seen in Figure 4.7, the peak field in these structures can be twice the average field; for applied biases of several volts across a layer a few microns thick, this means that the peak field is large enough that impact ionization cannot be ignored. In this case the behavior of the holes is very important. Holes generated in the high-field region near the anode will flow back to the cathode and encounter a barrier. The holes will accumulate on the cathode side of the layer and lower the net space charge there—either by contributing a large positive charge themselves, or by reducing the negative charge in the traps through recombination.

Band-to-band impact ionization is included in the numerical model as a generation term

$$G = \frac{1}{q}(\alpha_n |J_n| + \alpha_p |J_p|) \tag{5.8}$$

where J_n and J_p are the local electron and hole current densities, and α_n and α_p depend on the local field as

$$\alpha_{n,p}(E) = \alpha_{0(n,p)} \exp(-E_{0(n,p)}/|E|) \ . \tag{5.9}$$

We use this functional form because curve fits giving the values of the coefficients $\alpha_{0(n,p)}$ and $E_{0(n,p)}$ are readily available in the literature [41, 42, 43]. (The values we have used are taken from [43] and are shown in Table A.2. Since our electric field varies with position in the region of highest field, using these coefficients in this expression may overestimate the generation rate.) With the addition of this term, the J-V characteristics for the several thicknesses considered above take the forms shown in Figure 5.4. Here we have included drift velocity saturation and recombination through the traps, but not field emission. We show the J-V characteristics for this situation in the absence of
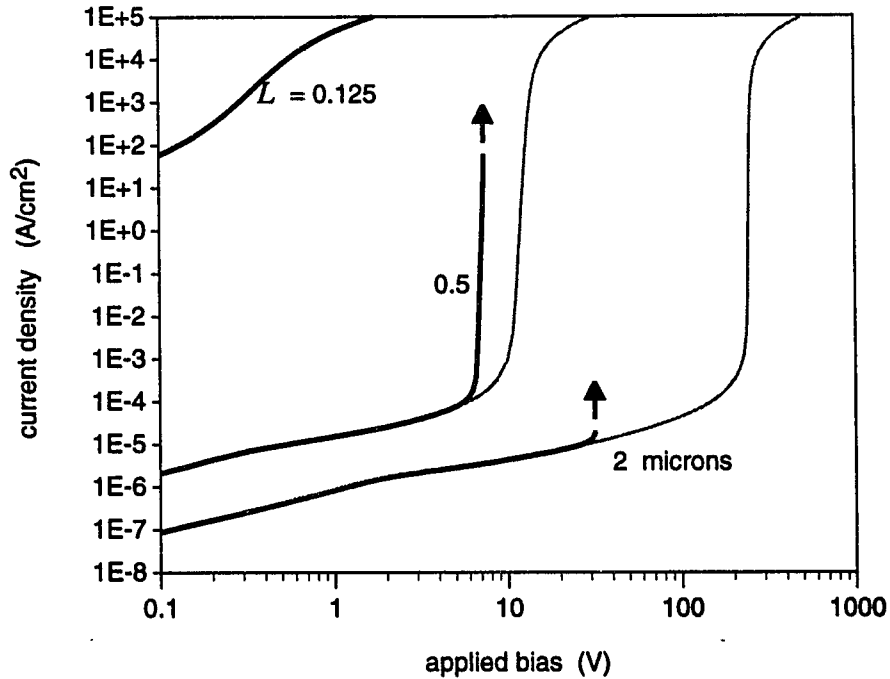
Figure 5.4:   J-V characteristics from numerical model, including velocity saturation and recombination through traps, for several layer thicknesses: (i) with impact ionization, (ii) without impact ionization.

impact ionization as well, in order to illustrate the effect of including it. (The 2-μm case is the same as that in Figure 4.8.) The arrows indicate avalanche breakdown, which appears in the model as a convergence failure when we try to step the voltage higher. We believe that this corresponds to the destructive breakdown that we observe in some samples under voltage-controlled operation.

That the convergence failure corresponds to a real physical phenomenon, rather than to a mathematical artifact, can be verified by examining the calculated hole currents. In Figure 5.5 we show the hole currents and total current for the same three planes as in Figure 5.2, now including SRH recombination through the traps and band-to-band impact ionization. The situation without impact ionization is shown also, for comparison. The rise in the hole currents below breakdown is due to avalanche injection, that is, to generation of
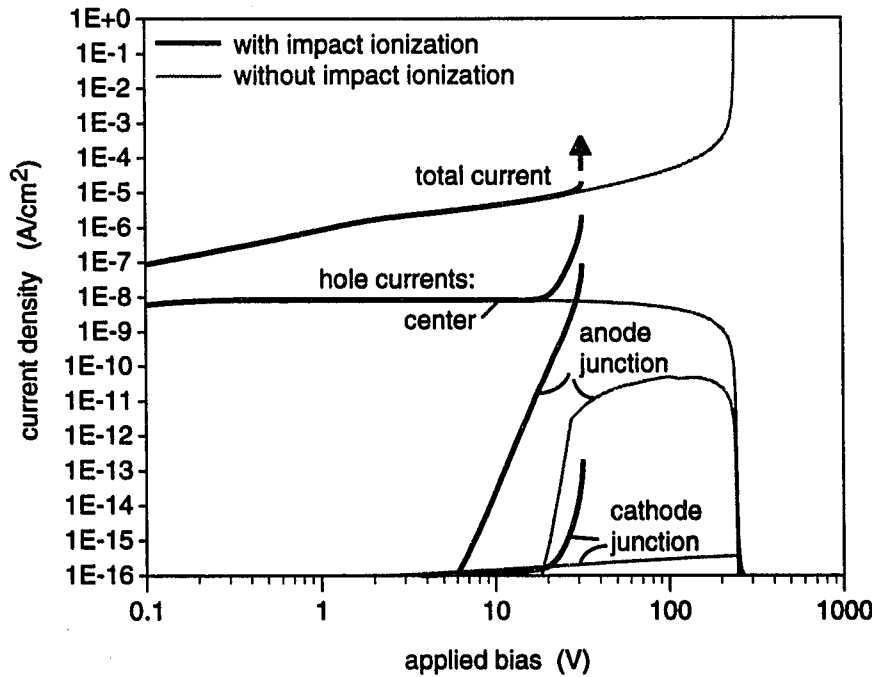
Figure 5.5:   J-V characteristics for 2-μm layer, showing total current and also hole currents in junction planes and in center of SI layer: (i) with impact ionization, (ii) without impact ionization.

electron-hole pairs by impact ionization in the high-field region at the anode.

The holes participate in a positive feedback mechanism, which is consistent with the abrupt breakdown and low critical voltages that we observe. The role of the holes in determining the critical voltage in the presence of impact ionization can be seen in Figures 5.6 and 5.7. Here we show an energy band diagram as well as the spatial variation of the electric field, free carrier concentrations, and trapped electron concentration for a 2-μm layer operating just below breakdown. To illustrate more clearly the effect of impact ionization, we also show the form that these distributions would take if we did not include it. We can see that the holes provide positive feedback for avalanche breakdown, as follows. Electron-hole pairs are generated in the high-field region at the anode. The electrons flow out into the anode, but the holes flow back across the SI layer and accumulate in the vicinity of the cathode barrier.
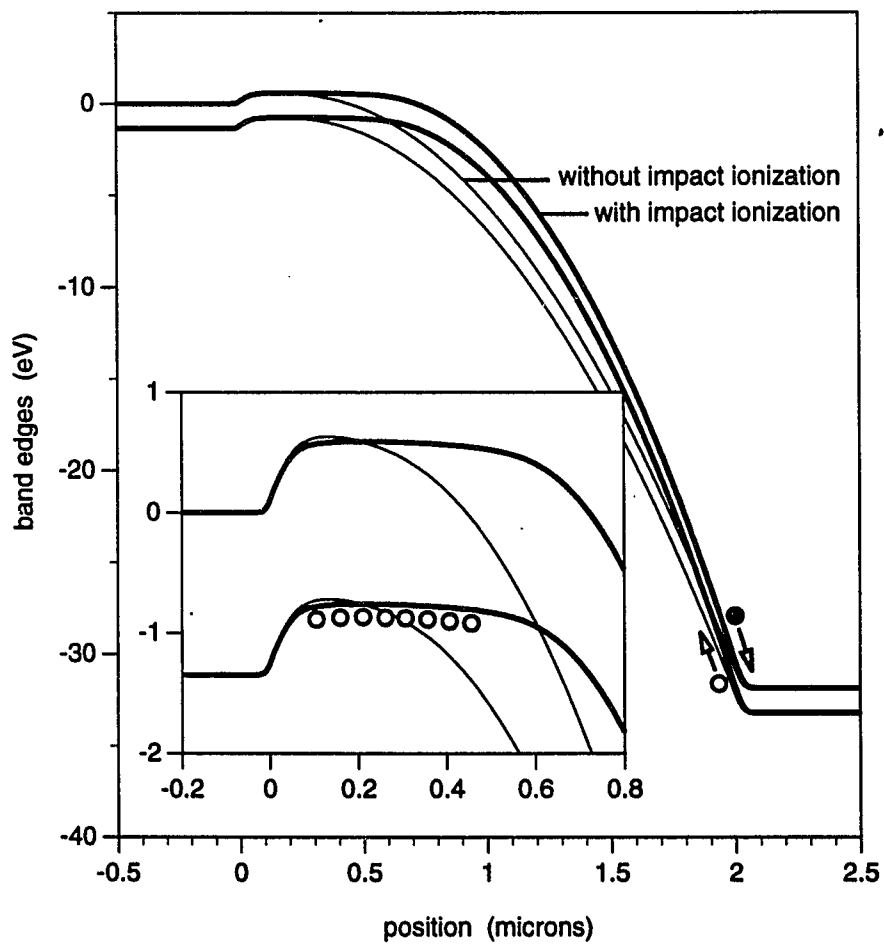
Figure 5.6: Energy band diagram for 2-μm layer operating under avalanche injection, just below breakdown. (i) with impact ionization, (ii) without impact ionization. $N_t = 8 \times 10^{16}$ cm^{-3}.
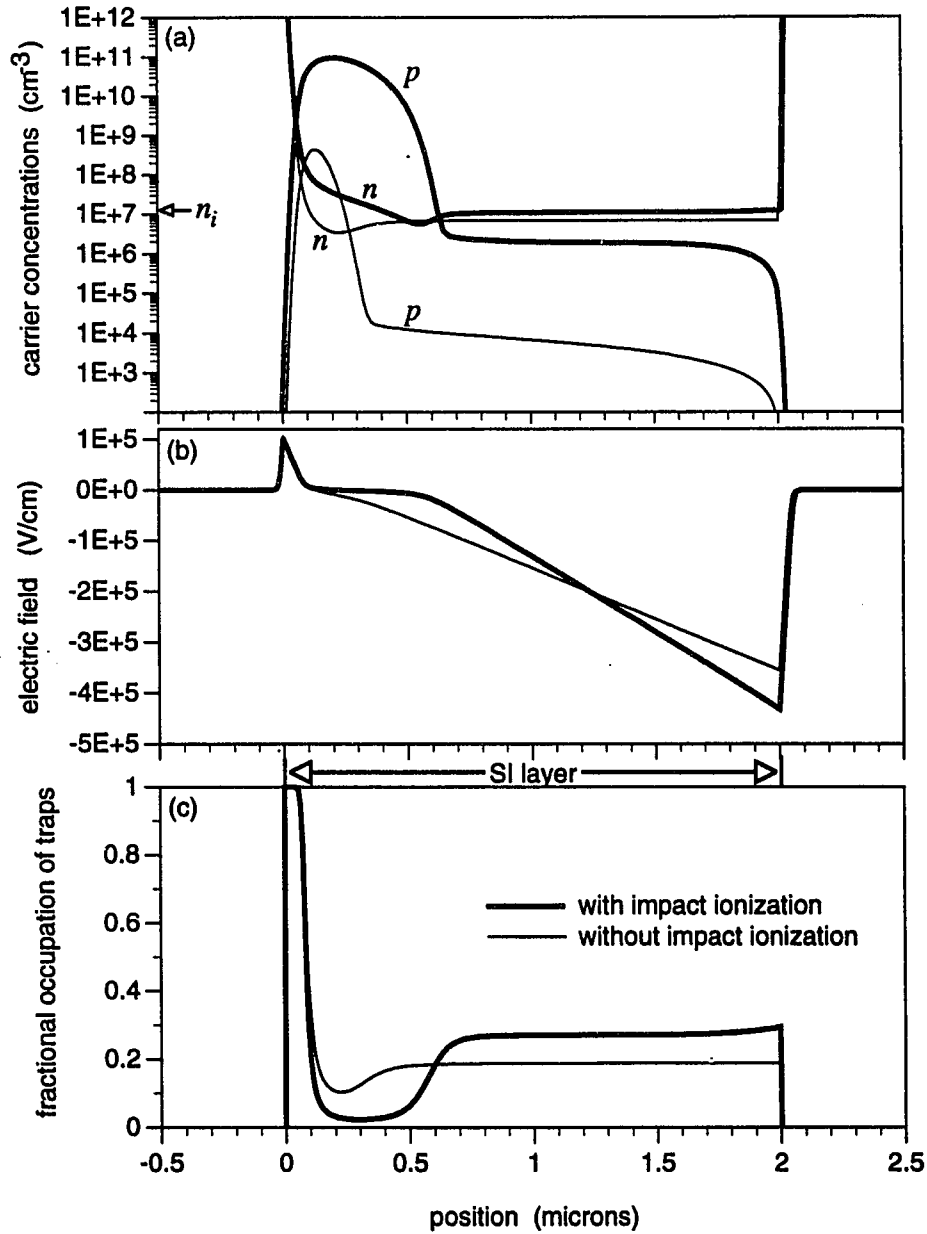
Figure 5.7:   Spatial variation of (a) carrier concentrations, (b) electric field, and (c) occupied traps, for same case as in Figure 5.6 (2-μm layer operating just below breakdown.) (i) with impact ionization; (ii) without impact ionization.

The large hole population there reduces the net space charge, which changes the shape of the barrier. (In the case shown, the reduction in space charge is principally the result of a reduction in the trapped electron concentration, due to recombination; but if we had not allowed recombination through the traps, the hole population at the cathode barrier would be several orders larger, and the positive space charge due to the holes themselves would have a similar effect.) The plane of zero field moves further away from the cathode junction, in effect decreasing the thickness of the layer. The potential drop then occurs over a shorter distance, so that the peak field increases. The increase in the field at the anode causes an increase in the generation rate due to impact ionization, which in turn increases the hole population at the cathode, and so on. (Similar phenomena have been observed in surface breakdown of both GaAs [44] and InP [22].)

We emphasize that the increased current that flows in the presence of impact ionization is due to increased electron injection resulting from a charge redistribution caused by the accumulation of holes in the vicinity of the cathode barrier. It is not due to the current carried by the generated holes themselves. The hole accumulation at the cathode barrier contributes an additional forward bias to the n-SI cathode junction, lowering the barrier height for electron injection. (The reduction in barrier height as compared to the situation without impact ionization can be seen in the inset to Figure 5.6.)

What we have shown for the cases of avalanche breakdown in Figures 5.4 and 5.5 is actually only a portion of the complete J-V curve. In the presence of impact ionization, our structure exhibits negative differential resistance as shown in Figure 5.8. Breakdown (or convergence failure in the model) occurs when we attempt to step the voltage past the turning point. The J-V curve has a third, positive-differential-resistance branch at very large currents, not shown in the figure, so that the overall curve has an "S" shape. Over some range of voltages, there are three possible current states, only two of which are stable. Breakdown under voltage-controlled operation results from the current snapping up to the third branch of the J-V curve as the turning point is passed.

(The inset to Figure 5.8 is provided for readers who may be wondering how a double-valued J-V characteristic is calculated using voltage boundary conditions. The five solutions indicated by crosses (the last two of which are indistinguishable on the scale of this inset) are acquired in order of increasing applied voltage. The first three of these lie on the lower, positive-differential-

resistance branch of the curve, while the fourth and fifth lie on the upper, negative-differential-resistance branch. Each successive solution is used as the initial guess for the calculation of the next. In the vicinity of the turning point, the calculation is very unstable, and the solutions corresponding to the two branches lie very close together. Thus, starting from a solution on the lower branch and increasing the voltage slightly, one sometimes finds a solution on the upper branch rather than on the lower branch—as, for example, in going from the third to the fourth cross here. The next higher-voltage solution then yields a decrease in current density. (I have resisted the temptation to provide an inset to the inset in order to illustrate this point.) When we thus detect that a solution on the upper branch has been found, we can change the sign of the voltage step and successively reduce the applied voltage so as to trace out the upper branch. Dots in the inset show upper-branch solutions acquired in order of decreasing applied voltage.)

Current flow in the presence of such an "S-type" (current-controlled) negative differential resistance has been shown to be spatially unstable [31]. That is, if the one-dimensional *J-V* curve has the form shown in Figure 5.8, a slight nonuniformity in current density will develop into filamentary current flow, with most of the area of the device operating on the lower branch of the *J-V* curve but with most of the current flowing in a narrow filament operating on the upper branch. Depending on load conditions and heatsinking, this results in thermal runaway [31] and catastrophic failure of the device, and is consistent with what we see experimentally.

All of this is due to avalanche injection of holes. Thus, in the presence of impact ionization, the holes play a crucial role, and this fact has a number of implications for modeling. We are no longer dealing with a single-carrier problem. In order to predict the breakdown behavior, the two-carrier problem must be solved self-consistently. Deriving an avalanche multiplication factor from the field profile calculated for the single-carrier problem without impact ionization would yield breakdown voltages larger than those calculated with the self-consistent model.

In the presence of impact ionization, the hole population at the cathode side becomes large enough that several of our earlier simplifying assumptions fail. There are enough holes to significantly change the occupation function for the traps: we can no longer assume quasi-thermal equilibrium between the trapped and free electrons, but must employ a separate quasi-Fermi level for the traps, as in (5.5). This results in a much lower concentration of trapped
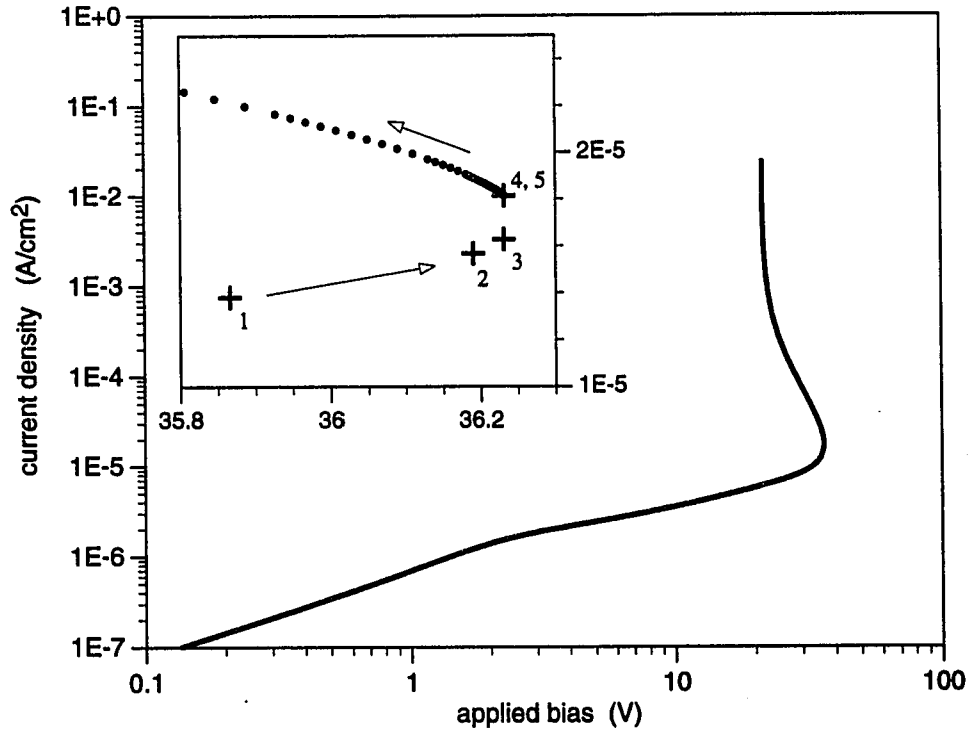
Figure 5.8: *J-V* curve for 2-μm layer, showing current-controlled negative differential resistance caused by avalanche injection. Magnified view (inset, drawn on linear scale) shows solutions in vicinity of turning point. Crosses indicate solutions found by increasing the applied voltage; dots indicate solutions found by decreasing the applied voltage.

electons in the vicinity of the cathode than would have been predicted under the quasi-equilibrium assumption. Recombination mechanisms that we could have ignored but for impact ionization now become significant: SRH recombination through the traps, as in (5.6), was a negligible effect without impact ionization; with impact ionization, it serves to depopulate the traps and contributes to the positive feedback loop. We also predict that in the presence of impact ionization the hole population at the cathode can be large enough to allow for considerable radiative recombination.

Radiative recombination can be included in the model as an extra source term $R_{rad} = Bnp$, where $B \approx 10^{-10}$ cm^3/s [26], so that the net genera-
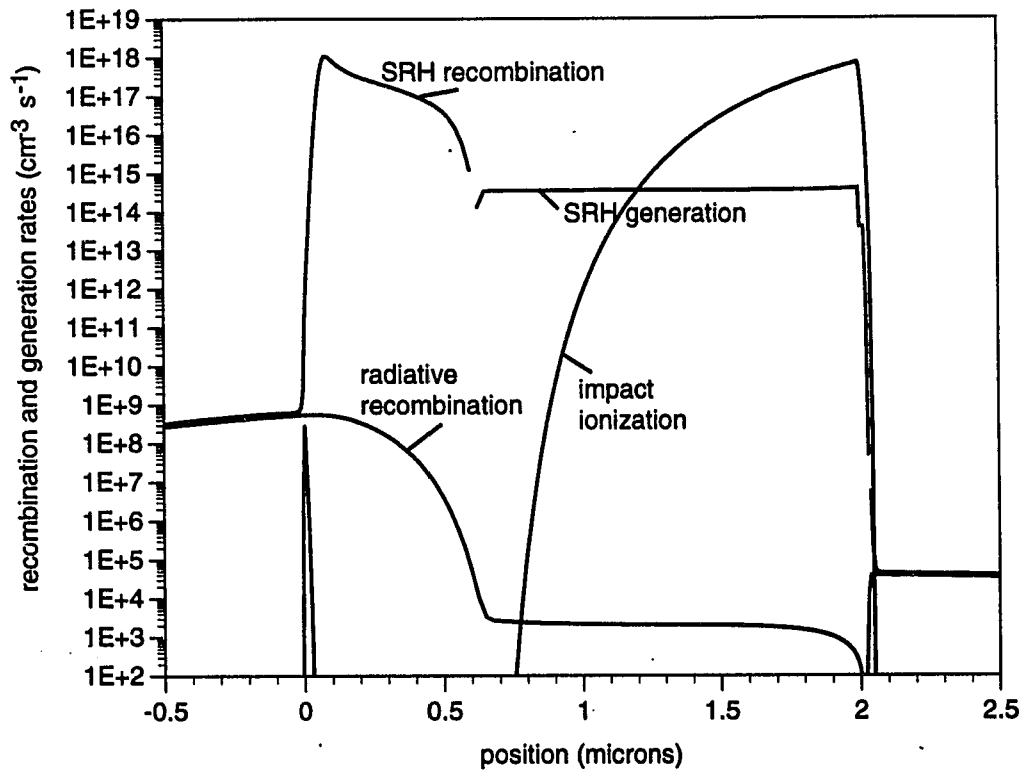
Figure 5.9: Generation and recombination rates under avalanche injection, for 2-μm layer operating just below breakdown.

tion/recombination rate is $G - R_0 - R_t - R_{rad}$. For our 2-μm layer operating just below breakdown, the contributions of the various terms are shown in Figure 5.9. Radiative recombination would be several orders larger were it not for SRH recombination through the traps.

At first, it may not have appeared that the field could be high enough for us to invoke avalanche breakdown as an explanation for device failure, even including a factor of 3/2 or 2 from the solution of the SCL problem. However, we now see that if we include impact ionization in the model, the peak field may be even larger for the same average field, due to the feedback mechanism

and field redistribution just described. In Figure 5.7b we compared the field distributions with and without impact ionization included in the model for a 2-μm layer operating just below breakdown. The average field for this case is 1.6×10^5 V/cm, but in the presence of impact ionization the peak field is 4.3×10^5 V/cm.

The bias level for the plots of Figures 5.6 and 5.7 is just below avalanche breakdown if we include impact ionization. The distribution of filled traps (Figure 5.7c) at this voltage illustrates an important point. When we include impact ionization, the current is rising steeply at this voltage, but the traps are still mostly empty. Depending on the trap density and the thickness of the SI layer, the avalanche breakdown voltage can be larger than, equal to, or (most importantly) lower than the trap-filled voltage. The critical voltage will correspond to whichever is lower.

For characterization, therefore, the critical voltage alone cannot be used to estimate the equilibrium density of empty traps in the manner that the simplifed theory would suggest. From a design perspective, the critical voltage for a thick layer may be much lower than the trap-filled limit predicted by the simplified theory. Because the avalanche breakdown voltage depends roughly linearly on the thickness of the SI layer, while the trap-filled voltage goes as the square of thickness, the critical voltage cannot be expected to continue to obey (3.5) for thick layers. (The predicted dependence of critical voltage on trap density and thickness is illustrated in Figures 7.2, 7.7–7.10, and 8.1.)

Finally, we again stress that while trap-filling is a reversible process, avalanche breakdown by the mechanism we describe here is not. Avalanche injection in this structure leads to a current-controlled negative differential resistance which is conducive to filament formation and thermal runaway.

Thus, besides predicting lower critical voltages than the simplified theory would suggest, the numerical model also predicts a major qualitative difference in the critical behavior.

Chapter 6

Comparison of models with experiment

This work was originally undertaken in order to explain a seemingly anomalous short-circuit failure mechanism that we saw while trying to characterize early Fe:InP samples. With the inclusion of impact ionization in a self-consistent two-carrier model, we now have a way of explaining this observation. The aim of this chapter is to do a more quantitative comparison of the models with experiment, and to verify the main features of the critical behavior. If we can verify the accuracy of the model, we can then go on and use it as a design tool. Indeed, we will show that the numerical model gives significantly better agreement with experiment than did the simplified theory, and that it is consistent with the observed critical behavior.

6.1 Summary of predictions of critical behavior

We use the term "critical behavior" to refer loosely to a steep rise in current as a function of voltage, regardless of the physical mechanism responsible. The "critical voltage" is more precisely defined as the voltage below which the current does not exceed some specified value. The critical voltage is typically associated with a steep rise in current, but depending on the current criterion it may occur in any part of the I-V curve. (We use the terms "trap-filled voltage" and "breakdown voltage" to designate a critical voltage that results from trap filling or avalanching respectively.)

The emphasis here is on the prediction of the critical voltage, since this will typically be the characteristic of the SI layer that limits the operating

range of a device. In Chapter 2 we introduced the criterion of $J < 1$ A/cm^2 for the critical voltage, and we will retain this definition throughout the work. For a typical buried heterostructure (BH) laser with stripe area 1 μm $\times$ 250 μm, contact area 50 μm $\times$ 50 μm, and threshold current density 1 kA/cm^2, a leakage current of 1 A/cm^2 would represent 1% of the threshold current. $J < 1$ A/cm^2 is therefore a reasonable performance criterion for the blocking layers in a BH laser. For a detector, a more stringent criterion would be used. Since the current is generally rising steeply, however, our conclusions are not sensitive to the particular current density chosen.

The predictions of the simplified and numerical models for this critical voltage as a function of SI layer thickness were summarized in Figure 2.2, for two trap densities. Recall that the simplified theory predicts a steep rise in current associated with the filling of the traps. (As we discussed in Chapter 3, this can be viewed as a filling in energy as well as a filling in space.) The trap-filled voltage is given by (3.5), and is proportional to the density of empty traps at equilibrium and to the square of the thickness of the SI layer. Provided there are enough traps that the critical voltage is not reached in the ohmic or SCL regime, the critical voltage is just the trap-filled voltage, and V_{cr} vs. L appears as a straight line on a log-log plot.

Using the numerical model, we predicted significant deviations from the simplified theory. In Chapter 4 we showed how diffusion from the contact layers would reduce the number of available traps and smooth out the trap-filled-limited regime (that is, reduce the slope of the J-V curve in the trap-filled limit), thereby reducing the critical voltage for thin layers below that predicted by the simplified theory. In Chapter 5, we went on to show that for thicker layers and larger trap densities, avalanche breakdown would occur before all the traps are filled—again leading to critical voltages well below those predicted by the simplified theory.

We can summarize the effects of the various mechanisms discussed in Chapters 4 and 5 by showing the changes they produce in a plot of V_{cr} vs. L (Figure 6.1). In all of the numerical models, the behavior for thin layers is dominated by diffusion from the contacts, as shown in Figure 2.2. The behavior for thicker layers is dominated by impact ionization, so in the calculations for Figure 6.1 we include that mechanism next, and then show the successive effects of SRH recombination/generation, drift velocity saturation, negative differential mobility, and field emission from traps on the resulting avalanche breakdown voltage. (We have added impact ionization next, because the other mechanisms do not affect the critical voltage except in the presence of impact
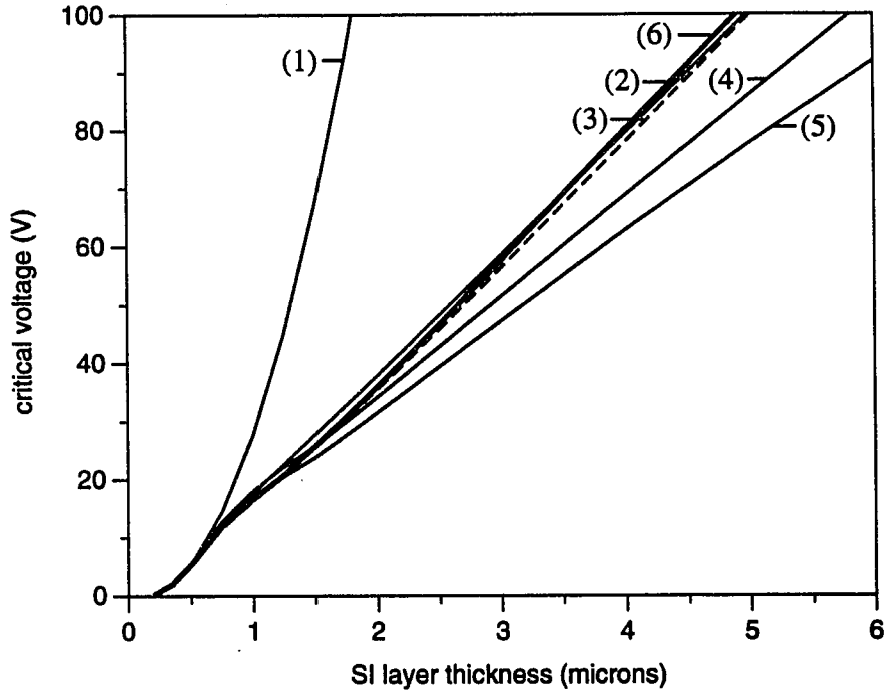
Figure 6.1: Critical voltage as a function of SI layer thickness, calculated with numerical model, showing effect of various mechanisms: (1)—trap filling plus diffusion only; (2)—same as (1) but with impact ionization; (3)—same as (2) but with recombination through traps; (4)—same as (3) but with simple velocity saturation; (5)—same as (4) but with negative differential mobility; (6)—same as (5) but with field emission from traps. $N_t = 4 \times 10^{16}$ cm^{-3} and $N_d = 5 \times 10^{15}$ cm^{-3} in SI layer; $N_{dn} = 1 \times 10^{17}$ cm^{-3} in contact layers.

ionization. That is, while they affect the shape of the J-V characteristic below the trap-filled limit, these other mechanisms do not affect the position of that limit. When the critical behavior is due to avalanching, however, they have significant effects.) The reasons for these effects can be understood on the basis of the field profiles and trapped carrier distributions discussed in Chapters 4 and 5: SRH generation near the anode increases the hole current available for impact ionization, but SRH recombination at the cathode reduces the hole population there, modifying the electrostatic feedback mechanism. Velocity saturation makes the distribution of trapped carriers more uniform, and lowers

the breakdown voltage by increasing the peak field for a given overall voltage. Negative differential mobility further lowers the breakdown voltage by reducing the trapped carrier concentration in the low-field (high-velocity) region near the cathode. Field emission returns the situation to one more nearly like the constant-mobility case by lowering the trapped carrier concentration near the anode.

We emphasize that the behavior for thin layers is the result of trap filling in all the cases we have discussed. Diffusion from the contacts reduces the number of initially empty traps, so that fewer injected electrons are needed to fill them. The actual trap-filled voltage is therefore lower than the trap-filled limit of the simplified theory—but the mechanism is the same and the cause of the steep rise in current is the same. The critical behavior is due to trap filling, and is reversible.

As the layer thickness is increased, the fraction of the traps that are filled by diffusion is reduced, and the actual trap-filled voltage approaches that predicted by the simplified theory. As the trap-filled voltage increases, however, it becomes larger than the voltage needed for avalanche breakdown, and the critical behavior of the device is then governed by impact ionization rather than by trap filling. As we saw in Chapter 5, the critical behavior due to avalanche injection is destructive.

We thus expect two qualitatively different kinds of critical behavior: a smooth, reversible rise in current due to trap filling, and an abrupt, irreversible rise in current due to avalanche breakdown. We expect to see trap filling for thin layers and low trap densities, and we expect to see avalanche breakdown for thicker layers and higher trap densities. As we increase either the SI layer thickness or the trap density, we expect a transition from reversible to irreversible critical behavior.

6.2   Growth and processing of test structures

To evaluate the accuracy of the numerical model, we compare its predictions with experimental results. A series of planar n-SI-n structures was grown for this purpose, using atmospheric-pressure non-hydride metalorganic chemical vapor deposition (MOCVD). The reactor was a horizontal quartz cell with a graphite susceptor heated by a mercury lamp. The sources were trimethylindium (TMI), tertiarybutylphosphine (TBP), *bis*-cyclopentadienyl iron (ferrocene), and disilane. Growth conditions were held constant at values

Table 6.1: Growth conditions for n-SI-n test structures.

thermocouple temperature	620	°C
pressure	1	atm (unregulated)
growth rate	4	μm/hr
EFFECTIVE FLOW RATES:		
TMI (20°C, 1100 torr)	280	sccm
TBP (20°C, 1100 torr)	125	sccm
ferrocene (15.3°C, 1100 torr)	1.4–86	sccm (SI layer only)
disilane, 200 ppm in hydrogen	0.13	sccm (n-layers only)
hydrogen (carrier)	5	slm

that we previously had shown [13] to yield good semi-insulating material; these are listed in Table 6.1. Only the thickness of the SI layer and the ferrocene concentration were intentionally varied.

The epitaxial layers were grown on Sn-doped n-type InP substrates. The substrate doping is on the order of 10^{18} cm^{-3}, so the potential drop in the substrate can be ignored. The n-type buffer and cap layers were deliberately rather lightly doped to facilitate comparison with the theory, which assumes nondegenerate statistics for the conduction band. Hall measurements on 2.5-μm-thick n-type calibration layers grown under the same conditions on commercial semi-insulating substrates show an electron concentration of about 1.3×10^{17} cm^{-3}. The n-layers in the n-SI-n structures were approximately 1.5 μm thick, to keep the anode depletion region within the epitaxial material for either polarity.

Calibration of doping levels in the SI layers is more difficult. One can measure the Fe content of the SI layer by secondary ion mass spectrometry (SIMS), but the Fe concentration does not necessarily correspond to the trap density. (Only substitutional Fe contributes active traps, but SIMS measures interstitials and precipitates as well.) Deep level transient spectroscopy (DLTS) using samples co-doped with Si would give a more direct measure of the trap density. Unfortunately, the trap density we wish to measure is on the order of 10^{16}–10^{17} cm^{-3}, and the n-type co-doping needs to be significantly larger than that—so it becomes difficult to deplete the layer.

If the background doping were constant, it would be possible to estimate

trap densities from the *I-V* characteristics of lightly-doped samples—that is, ones for which we can be sure that the critical behavior is due to trap filling. We did in fact attempt this, but found that the variation in background doping among the samples, which were grown over a period of several days, was too large to permit calibration of the trap density by this method. SIMS analysis revealed a large unintentional Si concentration in the SI layers of some of these wafers, the source of which has not been identified. In the end, for our quantitative comparison with the theory we have relied on heavily Fe-doped samples for which SIMS shows an Fe concentration well in excess of the published solubility limit for our growth temperature [34] and for which the Si concentration in the SI layer is below the SIMS detection limit. We therefore guess that the trap density in these layers is on the order of the solubility limit and that the background donor concentration is on the order of that found in our undoped material.

The principal test of the model is therefore the prediction of the critical behavior as a function of SI layer thickness. We assume that growth conditions remain constant from run to run, and vary the growth times to give samples with SI layers of approximately 0.3, 0.5, 1, 2, and 4 μm. Because of the spatial variation in the height of the gas-phase boundary layer, we also have a significant variation in the layer thickness along each wafer, so that a few samples provide a large number of different thicknesses. The thicknesses were measured by scanning electron microscopy of stained cross-sections on calibration wafers grown with InGaAs marker layers. (Thanks to Archie Holmes for the InGaAs recipe.)

For electrical measurements, "ohmic" contacts were made to the n-type cap layer and to the substrate. On the epi side, evaporated AuGe/Ni/Au was lifted off to form dots, with diameters ranging from 20 to 100 μm. On the back side, AuGe/Ni/Au was evaporated to form a broad-area contact, and the contacts were alloyed at 380°C in the rapid thermal annealer. Using the top metal as a mask, we then etched through the n-type cap using a mixture of one part hydrochloric acid to four parts phosphoric acid. To obtain a stable surface, we followed this isolation etch with a 15-second dip in buffered HF.

6.3 Current-voltage measurements

Current-voltage (*I-V*) measurements were done on a Hewlett-Packard 4145B semiconductor parameter analyzer. The measurements were performed using voltage control because this method yielded linear *I-V* curves for several large calibration resistors. Current-control measurements on the calibration resistors showed a large nonlinearity around 1 nA, presumably due to range-switching in the instrument.

The measurements shown here were performed in the dark at uncontrolled room temperature. For the power levels dissipated in our devices below breakdown, we estimate a temperature rise on the order of several mK with respect to the back contact, so elaborate heat sinking should not be necessary.

Samples were set on a gold-coated copper stud which was in turn probed to make the back contact. Top contacts were made with a beryllium-copper probe tip, and care was taken to set it down gently. Tungsten probes and more aggressive pressure generally resulted in larger currents and less reproducible results, presumably due to damage on the surface.

The use of coaxial leads up to the probe tips reduced the noise floor considerably. With these probes, an open circuit measures about 10^{11} Ω; a typical low-bias resistance for one of our 100-μm-diameter heavily-doped devices is 10^9 Ω. For the set of measurements shown here, both medium and long integration times on the 4145B yielded similar results, without much hysteresis, so we believe that these results are representative of the steady state. For these measurements, the total current also scaled approximately quadratically with the device diameter, so we believe that these results are representative of bulk current injection.

The measurements shown here were all performed in an area of roughly 0.4 × 0.8 cm in one upstream corner of the wafers. Most of the longitudinal thickness variation discussed above occurs within this area. (For wafer-to-wafer comparison, it is important that measurements be made in similar positions on each wafer.) For the present work, we focus on the thickness dependence of the critical behavior.

In Figure 6.2 we show representative *I-V* curves from the thinner downstream region of each of five wafers, all grown with an effective ferrocene flow of 65 sccm. The thicknesses of the SI layers are 0.29, 0.51, 0.95, 1.9, and 3.6 μm. The nature of the critical behavior as we move from thinner to thicker layers agrees well with the predictions of the numerical model: For the thinnest
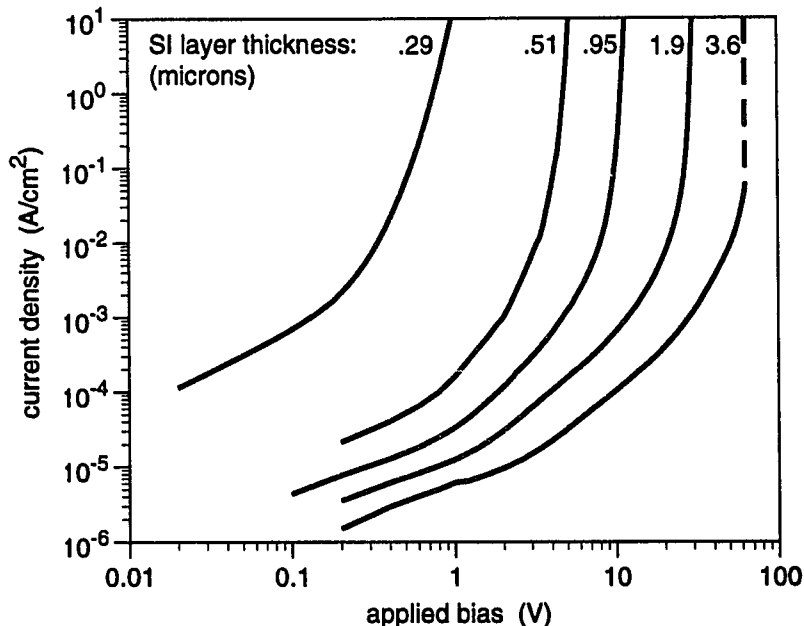
Figure 6.2: Measured *I-V* curves for *n*-SI-*n* structures of different SI layer thicknesses, doped with 65 sccm effective ferrocene flow (which exceeds the solubility limit.) Current densities were obtained by dividing the measured current by the mask area of the top contact.

layer we have a sloping TFL regime, which is characteristic of a situation in which the bandbending at the interfaces takes up a significant fraction of the total thickness. For thicker layers we see a steeper TFL regime, and finally for the thickest layer we have an abrupt, destructive breakdown.

The critical behavior for the four thinner layers is reversible and repeatable, as is consistent with trap filling. The critical behavior for the 3.6-μm layer is irreversible: after the initial measurement, subsequent measurements on the same device show a short. Inspection of the failed devices with a light microscope typically reveals a small crater, which is consistent with the filament formation one would expect under avalanche injection.

The transition from reversible to irreversible behavior with increasing SI layer thickness was also observed within a single wafer. For the 1.9-μm wafer, the thickness on the upstream edge ranges up to approximately 2.7 μm. De-
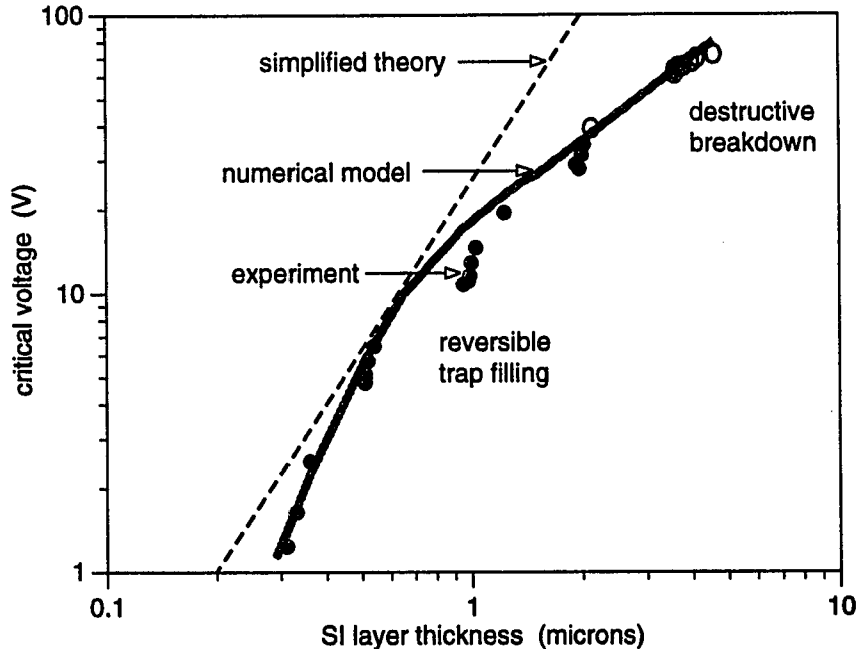
Figure 6.3: Critical voltage a function of thickness, for large trap density. Experimental results show transition from reversible trap filling (dots) to destructive breakdown (circles) at a thickness of about 2 μm; numerical model shows it at about 1.5 μm. (Simplified theory does not predict this transition.) Experimental results are from wafers doped with 65 sccm ferrocene. Theory curves use $N_t = 4 \times 10^{16}$ cm^{-3} and $N_d = 5 \times 10^{15}$ cm^{-3} in SI layer, and $N_{dn} = 1 \times 10^{17}$ cm^{-3} in contacts. Numerical calculations use $\mu_{n_0} = 1000$ cm^2/V-s.

vices at positions corresponding to thicknesses of 2.1 and 2.6 μm showed abrupt irreversible breakdown, while devices further downstream (and thus with thinner SI layers) showed smooth, reversible behavior.

The thickness-dependence of the critical voltage, both from wafer to wafer and within wafers, is shown in Figure 6.3. The transition from reversible to irreversible behavior is labeled. In this figure we also show the critical voltage as a function of layer thickness as calculated in the simplified and numerical models, using the doping levels shown in the figure caption. For the numerical model, the physics included corresponds to the lowest set of critical voltages shown in Figure 6.1.

Before considering the details of the comparions between the numerical model and the experiments, we note that, as we would expect, the numerical model gives much better qualitative agreement with experiment than does the simplified theory. The numerical model predicts the reduction in critical voltage at both ends of the thickness range, as compared with the trap-filled limit of the simplified theory, and gives us a means to understand this reduction in terms of the different physical processes that dominate in the different thickness ranges.

Assuming that the critical voltage coincides with the trap-filled limit, the simplified theory predicts that a given fractional change in the SI layer thickness will result in the same fractional change in the critical voltage, regardless of the layer thickness. That is, in the simplified theory, $(\Delta V_{\mathrm{TFL}}/V_{\mathrm{TFL}})/(\Delta L/L)$ = 2 for any L. The numerical model, on the other hand, predicts that a given fractional change in SI layer thickness will result in a larger fractional change in the critical voltage for thin layers and a smaller fractional change in the critical voltage for thick layers, which is consistent with experiment.

Finally, the numerical model predicts the observed qualitative change in the nature of the critical behavior, from smooth and reversible to abrupt and destructive—which the simplified theory does not.

In Figure 6.3, the five clumps of points correspond to five separate wafers with different growth times and therefore different average SI layer thicknesses. Within each wafer, the six points range from positions near the upstream edge, where the layers are thickest, to approximately 0.8 cm downstream, where the layers are thinner. That all thirty data points do not lie on a smooth curve indicates that the variation in performance is not entirely due to the variation in SI layer thickness. This suggests that, in addition to the thickness variation as we move downstream, we also have some doping nonuniformity.

A similar effect is seen Figure 6.4, where we show critical voltage as a function of SI layer thickness for another series of five wafers, this time with an effective ferrocene flow of 11.4 sccm. Again, we have a performance reduction from upstream to downstream within each wafer that cannot be entirely explained by the thickness variation along the wafer. The remaining variation could be the result either of a reduction in the trap density, or an increase in the background level, or an increase in the n-doping in the contact layers as we move downstream. If the n-doping in the contacts is low enough that the anode gets fully depleted, then the thickness variation in the contact layers would also contribute to the degradation downstream, since less voltage would
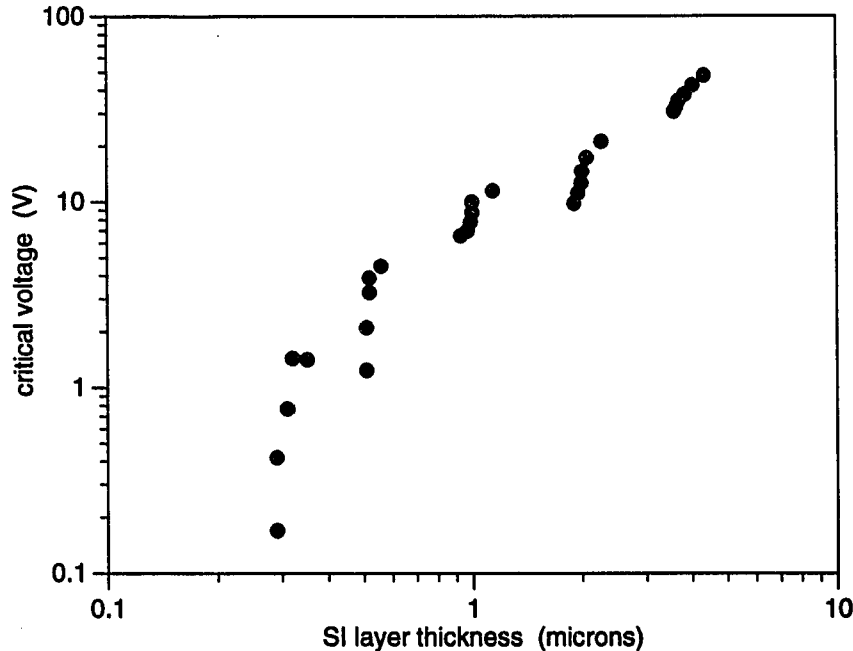
Figure 6.4: Critical voltage a function of thickness, for medium trap density. These experimental results are from wafers doped with 11.4 sccm ferrocene. As in Figure 6.3, the thickest devices in each group of points are from the upstream area of the wafer, with thickness decreasing downstream. All show reversible critical behavior.

be dropped across a thinner anode. (One should also keep in mind that the doping can vary significantly from wafer to wafer. SIMS results for the 3.6-μm wafers in these series show a larger Fe concentration on the substrate side of the SI layer. If the first half micron of Fe:InP in general has a larger trap density than the rest of the layer, then the average trap density will be higher in the thin layers than in the thicker ones.) In Chapter 7 we model the effects of various doping changes, and estimate the variation in doping that would be needed to account for the effects shown here.

For the 65-sccm data (Figures 6.2 and 6.3), we saw a transition from reversible to irreversible breakdown as we increased the layer thickness for a constant doping level. We can also see such a transition as we increase the
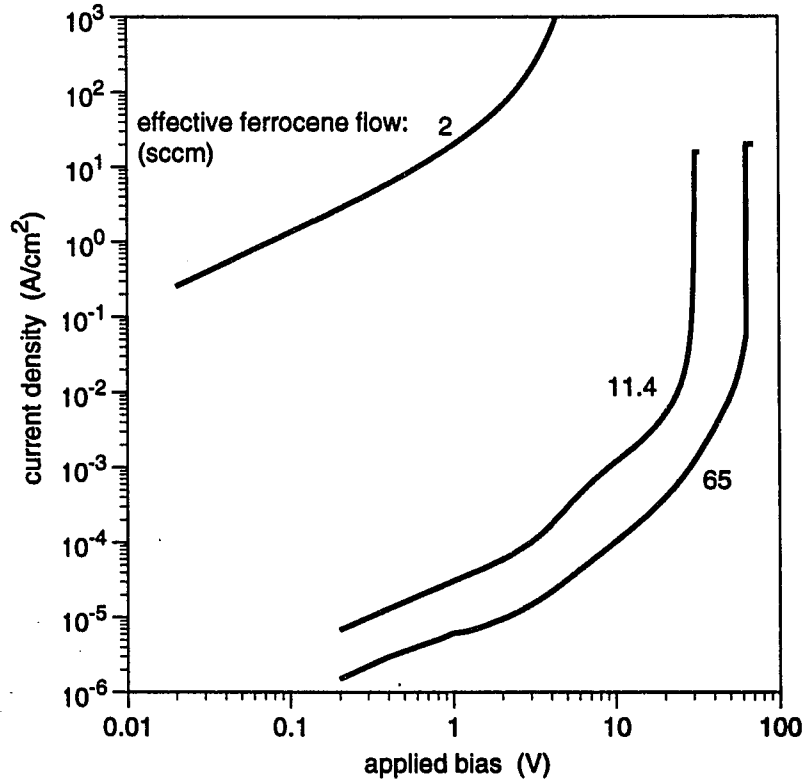
Figure 6.5:   Measured I-V curves for 3.6-μm-thick SI layers doped with 2, 11.4, and 65 sccm ferrocene. Current densities were obtained by dividing the measured current by the mask area of the top contact. Currents for 11.4 and 65 sccm cases are externally limited at the top of the curves shown. 65 sccm case shows destructive breakdown.

doping level for a given thickness, which is apparent in the data from the thickest of the five wafers in Figures 6.3 and 6.4. For any of the points with $L > 2.1$ μm, we have reversible trap-filling at the lower doping and irreversible breakdown at the higher doping.

We grew a third series of five wafers, like those shown in Figures 6.3 and 6.4 but using an even lower Fe flow (2 sccm). The background donor concentration in this series, unfortunately, was too large and too variable for the resulting plot of V_{cr} vs. L to be useful. For particular thicknesses, however, we can

compare the *I-V* curves with 2, 11.4, and 65 sccm Fe to show the progression of critical behavior with increasing trap density (Figure 6.5).

6.4 Difficulties .

A quantitative comparison of the numerical predictions of the critical voltage with experiment is complicated by our ignorance of several important properties of the material. The numerical curve shown in Figure 6.3 is calculated for a trap density N_t of 4×10^{16} cm^{-3} and a background donor density N_d of 5×10^{15} cm^{-3} in the SI layer, with an n-layer doping N_{dn} of 1×10^{17} cm^{-3}. The value of N_{dn} is obtained from Hall measurements on calibration samples, as mentioned above. The trap density is taken as the published solubility limit for our growth temperature, according to the data of Wolf *et al.* [34], because we have reason to believe (both from SIMS and from old resistivity-vs.-doping data [13]) that the Fe concentration in this series of wafers exceeds the solubility limit. The background doping level is consistent with Hall measurements on our undoped material [4] (performed by Archie Holmes).

The fit shown in Figure 6.3 includes all of the physics described in Chapters 4 and 5, with the exception of field emission. A nonlinear velocity field curve as described by (4.10) was used for the electrons, but with a low-field mobility of 1000 cm^2/V-s rather than the 2000 cm^2/V-s shown in Figure 4.5. This results in a velocity-field curve as shown by the solid line in Figure 6.6. While we measure a room-temperature Hall mobility of 2400–4400 cm^2/V-s on our 1×10^{17} cm^{-3} n-type material, it would not be surprising if the mobility were lower in the SI material, especially if it is doped in excess of the solubility limit. For the fit shown in Figure 6.3, only the value of μ_{n_0} has been adjusted; values of other constants were taken from the literature (as shown in Appendix A.)

We have lowered the value of μ_{n_0} to 1000 cm^2/V-s because using the larger value would result in the prediction of avalanche breakdown voltages lower than our measured ones. (A discrepancy between a given measured breakdown voltage and a *higher* predicted value can be readily explained on the basis of material or processing nonuniformities; a discrepancy of the opposite sense is more difficult to account for.) With 1000 cm^2/V-s, we predict avalanche breakdown for somewhat thinner layers than those for which we observe it, but we obtain good overall agreement with the measured values of the critical voltage.
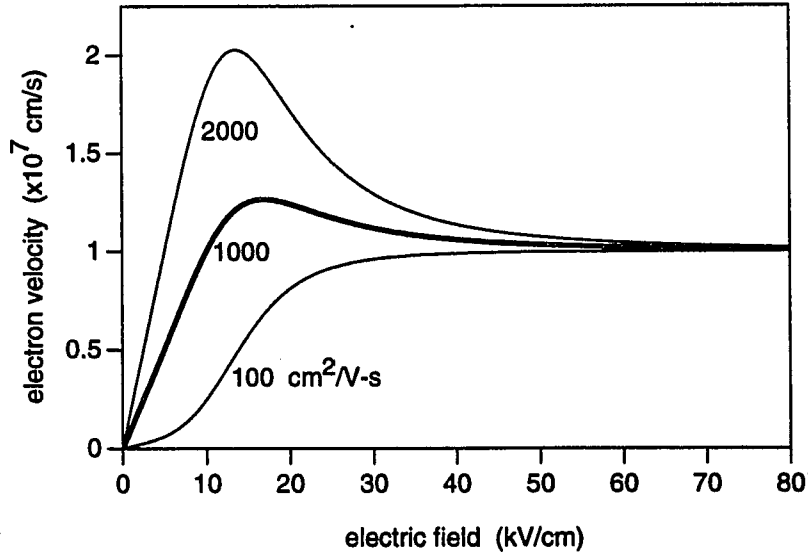
Figure 6.6:   Numerical velocity-field curves resulting from use of smaller low-field mobilities: (i) $\mu_{n_0} = 1000$ cm^2/V-s; (ii) $\mu_{n_0} = 100$ cm^2/V-s. The 2000 cm^2/V-s curve from Figure 4.5 is reproduced here for comparison.

On the other hand, the model as used for the fit of Figure 6.3 gives poor agreement with the shapes of our measured I-V curves below breakdown. A set of measured curves was shown in Figure 6.2; corresponding curves obtained from the model are shown in Figure 6.7. The sublinear regime that we predict for intermediate bias levels on the thicker layers does not agree with our experimental results. (Although such a sublinear regime has not been reported in Fe:InP, this feature does strongly resemble behavior seen in low-temperature-grown (LT) GaAs [38].)

In the model, the sublinear regime shown in Figure 6.7 results from the negative differential mobility section of the velocity-field curve. Inclusion of field emission, as discussed in Section 4.4, reduces but does not entirely eliminate the sublinearity for thick layers. The resulting I-V curves are sill not in very good agreement with experiment, and the slope of log V_{cr} vs. log L in the
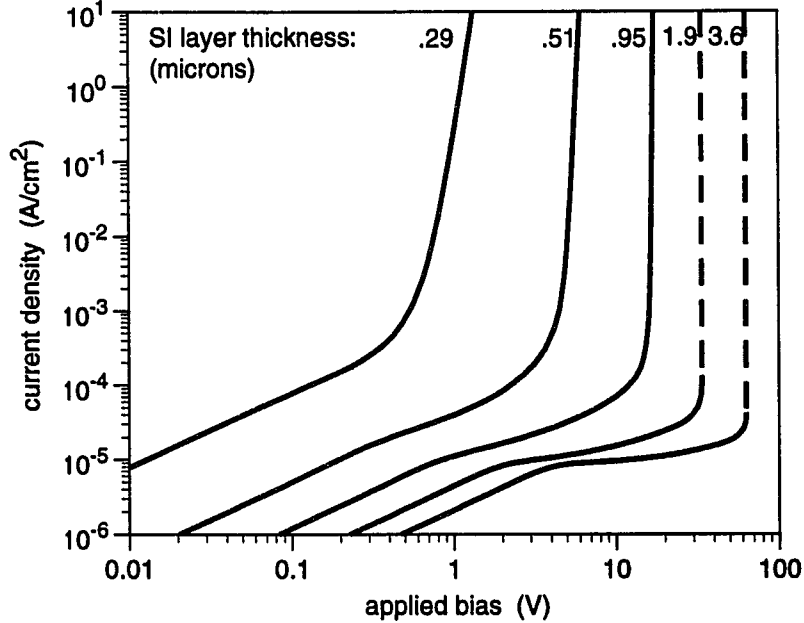
Figure 6.7: Calculated *I-V* curves for *n*-SI-*n* structures with SI layer thicknesses corresponding to those of Figure 6.2, using model parameters as in Figure 6.3.

avalanche breakdown regime is somewhat larger than what we observe.

One might argue that our trap density is much lower than we have assumed, or our background doping much larger, so that the slope of our measured *I-V* curves below breakdown is due to trap filling. For the fit of Figure 6.3, we assumed a trap density N_t corresponding to the published solubility limit at our growth temperature, where our growth temperature was measured by a thermocouple inside the susceptor. The actual surface temperature, and therefore the solubility limit, may be lower. Given that the trap-filled-limited voltages observed on our intermediately-doped (11.4 sccm) samples show a difference $N_t - N_d$ on the order of 10^{16} cm^{-3}, however, a comparison of our 11.4-sccm and 65-sccm data suggests that, for the latter, $N_t - N_d$ is indeed on the order of 4×10^{16} cm^{-3}.

We also considered the possibility that the electron mobility in our samples is much lower than we have assumed, so that the velocity saturates only

at higher biases and negative differential mobility is eliminated. Assuming a very low electron mobility—on the order of 100 cm^2/V-s—yields *I-V* characteristics that are in much better agreement with experiment, and also gives good agreement for the values of the critical voltage as a function of thickness and for the transition from reversible to destructive breakdown. (In this case the predicted avalanche breakdown voltages are on the order of xx% higher than those we observe, but as we have pointed out above, this discrepancy is not difficult to explain. Given the instability of the current distribution under avalanche injection, and given that we have not included impact ionization into or out of the traps, we might expect that measured breakdown voltages would be lower than those we predict with the present model.)

Using a low value of μ_{n_0} in the expression (4.10) yields *I-V* curves that show the characteristic shape exhibited by the 11.4-sccm curve in Figure 6.5 and reported by Huang *et al.* [12], Wolf *et al.* [34], Tsang *et al.* [14], and others. In the model, however, the "bump" in the SCL regime is a result of the decidedly strange velocity-field curve that results from plugging $\mu_{n_0} = 100$ cm^2/V-s into (4.10), shown as the dotted line in Figure 6.6. The similarity of the shapes of the resulting *I-V* curves with the shapes of measured curves may be purely coincidental; without a physical explanation for the improbable $v(E)$ behavior shown, we are reluctant to attribute the measured shape solely to velocity-field phenomena. The difficulty with the low-mobility approach is in explaining the low mobility itself.

Lacking such an explanation, we leave the shape of the *I-V* characteristics below breakdown as an unsolved problem requiring further work. Using the present model, with $\mu_{n_0} = 1000$ cm^2/V-s and other parameters taken from the literature, we do obtain excellent agreement with our experimental results for the critical voltage as a function of thickness. We also have fairly good agreement for the transition from reversible trap filling to destructive breakdown.

Chapter 7

Numerical results

In Chapters 4 and 5 we developed a numerical model, adding physical mechanisms one at a time and illustrating their effects using calculations based on "best-case" dopings for the SI layer and on materials parameters taken from the literature. In Chapter 6 we found that this model gives good agreement with our experimental results for the critical voltage as a function of thickness. It also predicts the transition from reversible critical behavior to destructive breakdown that we observe. While discrepancies remain with regard to the behavior in the SCL regime, we find that the model provides a useful description of critical behavior in Fe:InP.

Having thus evaluated the accuracy of the model, we can use it to predict performance variations for an n-SI-n structure as a function of various design and materials parameters. In this chapter we explore the sensitivity of the numerical predictions to several of these parameters. In addition to illustrating the properties of the model, this helps us to predict what sort of performance improvement can be expected as a result of changes to the material that we might attempt. Knowing the sensitivity of the results to changes in the material properties is also a useful guide to the identification of unintentional variations in the material.

We then return to the design implications of these results, and state some design rules in contrast to those that would be suggested by the simplified theory.

7.1   Sensitivity to materials parameters

In this section we examine the sensitivity of the predicted critical voltage to changes in various model parameters. We look first at the effects of changes in doping levels—trap density and background donor concentration in the SI layer, and donor concentration in the contacts—and then at the effects of changes in other properties of the material and of the trap.

Because the SI layer thickness L is the most likely thing one would intentionally vary in a design situation, we show these sensitivities in the form of families of V_{cr} vs. L curves. We show the effects of order-of-magnitude changes in both directions from the set of parameters used to match our experimental results for our best material from Chapter 6.

Contact doping. For the calculations in Chapter 6, we used an n-doping of 1×10^{17} cm^{-3} in the contacts, which was consistent with the measured doping level for our experiments. For a trap density of 4×10^{16} cm^{-3} and a background donor concentration of 5×10^{15} cm^{-3} in the SI layer, we show in Figure 7.1 the effect of varying the contact doping over the range 10^{16}–10^{18} cm^{-3}. As we would expect, the contact doping is important for thin layers. Increasing the donor concentration in the contacts increases the number of electrons that diffuse into the SI layer, reducing the number of available traps and thus lowering the critical voltage. (In addition, increasing the donor concentration reduces the width of the anode depletion layer, which increases the potential drop across the SI layer.) For a lower trap density, the effect for thin layers would be even more pronounced.

In a real device, the contact doping is likely to be higher than the 1×10^{17} cm^{-3} that we used in our experiments. To show the sensitivity of the critical voltage to model parameters in comparison with our experimental results, we continue to use $N_{dn} = 1 \times 10^{17}$ cm^{-3} for the calculations in this section. In the next section we switch to a larger contact doping for use in developing design rules for the SI layer.

Trap density. In Figure 7.2 we show the effect of increasing or decreasing the trap density in the SI layer by an order of magnitude from our value of 4×10^{16} cm^{-3}. Because we have assumed a background donor concentration of 5×10^{15} cm^{-3}, reducing the trap density to 4×10^{15} cm^{-3} would result in a net concentration of 1×10^{15} cm^{-3} of uncompensated background donors, so the material would not be semi-insulating. The critical voltage in this instance
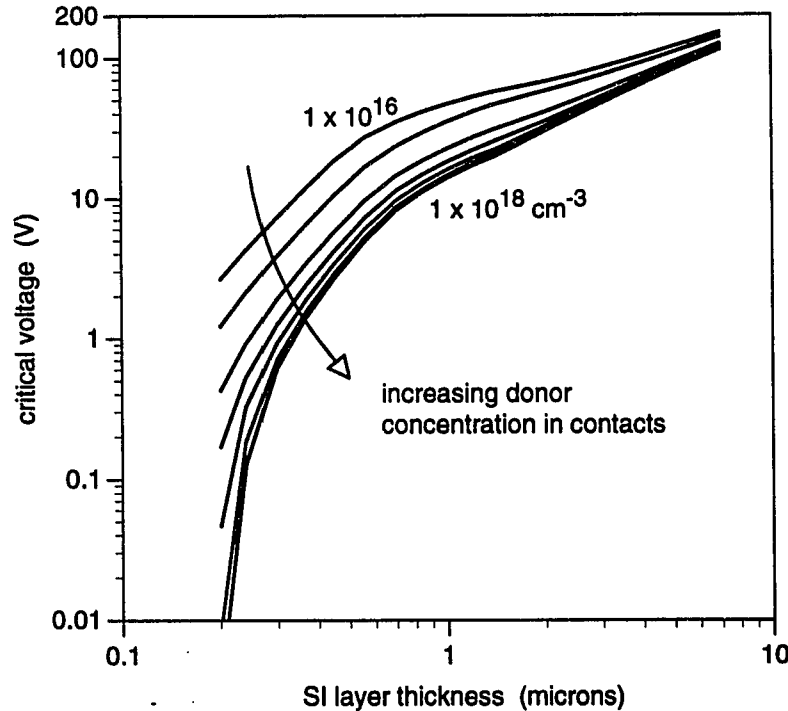
Figure 7.1: Sensitivity of critical voltage to donor concentration in n-layers, for $N_t = 4 \times 10^{16}$ cm^{-3} and $N_d = 5 \times 10^{15}$ cm^{-3} in the SI layer. Values of N_{dn} are: 1×10^{16}, 2×10^{16}, 5×10^{16}, 1×10^{17}, 2×10^{17}, 5×10^{17}, and 1×10^{18} cm^{-3}.

would occur at very low voltage, in the ohmic regime of operation.

On the other hand, increasing the trap density to 4×10^{17} cm^{-3} takes us out of the range of Fe-doping levels that have been reported so far. It is instructive to predict the effect of such an improvement in trap density, however, so as to gauge the benefit that might be gained by achieving an improvement in solubility or activation. We see that the effect would be significant for thinner layers, where the critical behavior is still governed by trap filling, but that increasing the trap density would be less effective for improving the avalanche breakdown voltage for thicker layers.

Background doping. The concentration of unintentional donors in the
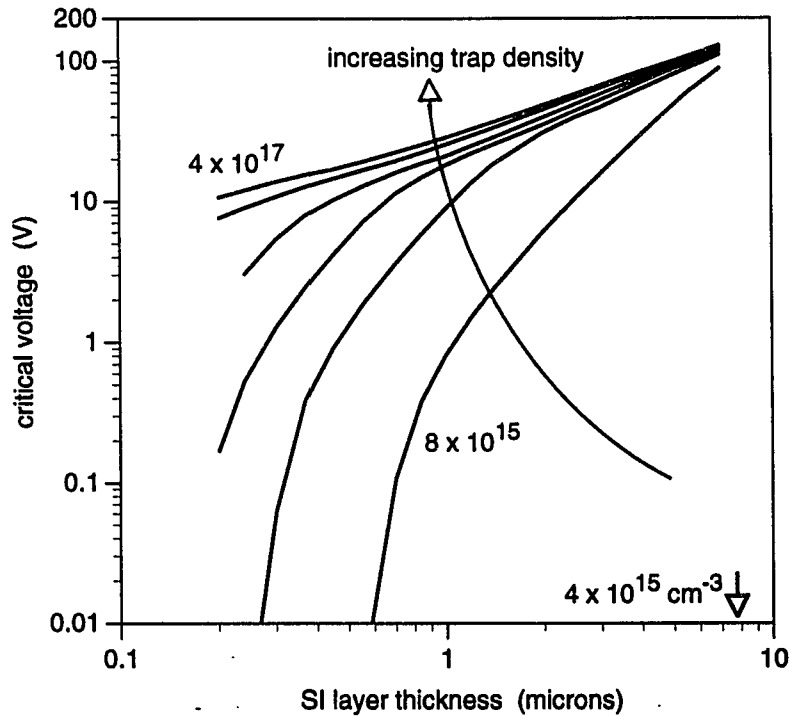
Figure 7.2: Sensitivity of critical voltage to trap density in SI layer, for N_{dn} $= 1 \times 10^{17}$ cm^{-3} in contacts and $N_d = 5 \times 10^{15}$ cm^{-3} in the SI layer. Values of N_t are 4×10^{15}, 8×10^{15}, 2×10^{16}, 4×10^{16}, 8×10^{16}, 2×10^{17}, and 4×10^{17} cm^{-3}.

SI layer is one of the most difficult properties to control. In Figure 7.3 we show the effect of an order of magnitude variation in both directions about 5×10^{15} cm^{-3}. Again, for our trap concentration of 4×10^{16} cm^{-3}, increasing the background doping to 5×10^{16} cm^{-3} would result in uncompensated donors and a critical voltage too small for the scale of the figure.

Except in cases in which the background donor concentration is on the order of the trap density, decreasing the background provides little improvement in the critical voltage. If the critical behavior is due to trap filling, then the critical voltage depends largely on the difference $N_t - N_d$, so that changes in N_d have little effect if $N_d \ll N_t$.
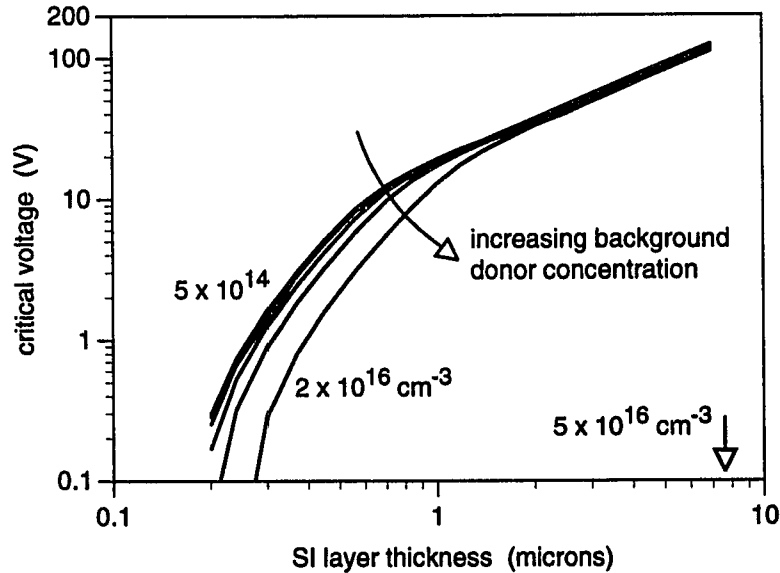
Figure 7.3: Sensitivity of critical voltage to background donor concentration in SI layer, for $N_t = 4 \times 10^{16}$ cm^{-3} in the SI layer and $N_{dn} = 1 \times 10^{17}$ cm^{-3} in the contacts. Values of N_d are 5×10^{14}, 1×10^{15}, 2×10^{15}, 5×10^{15}, 1×10^{16}, and 2×10^{16} cm^{-3}. Curve for $N_d = 5 \times 10^{16}$ cm^{-3} is completely off scale.

We have seen that in general the doping levels in the SI layer do not have a strong effect on the critical voltage when the critical behavior is due to avalanche breakdown. In the above calculations of the sensitivity of the critical voltage to these doping levels, though, we have only accounted for the direct effect of charge-density changes through the Poisson equation (and, in the case of the trap density, through the SRH generation/recombination rate.) We have not included the possible side effects of the doping changes, such as variations in defect densities (which could affect the carrier lifetimes) or in scattering rates (which could affect the mobility).

We next consider the effects of changes in some of these other quantities. For the remaining calculations in this section, the doping levels have been held at 4×10^{16} cm^{-3} traps and 5×10^{15} cm^{-3} background donors in the SI layer, and 1×10^{17} cm^{-3} donors in the contacts.
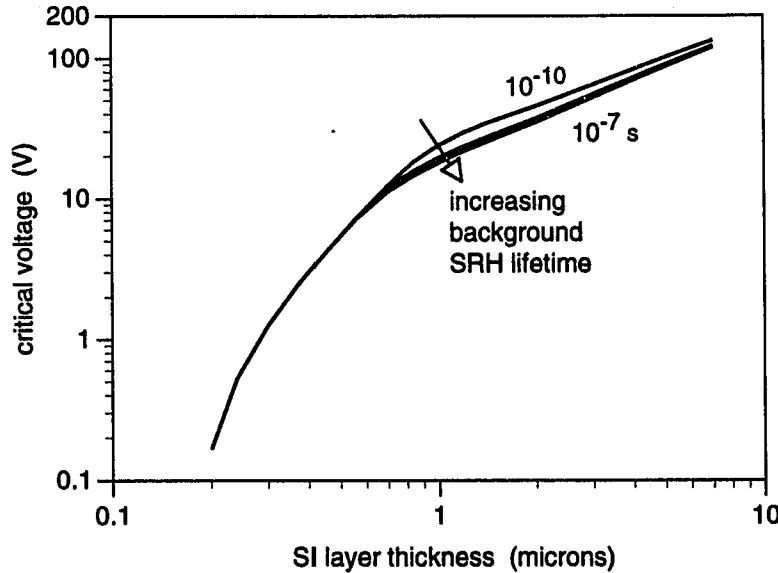
Figure 7.4: Sensitivity of critical voltage to background SRH lifetimes. Values of $\tau_{n_0} = \tau_{p_0}$ are 10^{-10}, 10^{-9}, 10^{-8}, and 10^{-7} s.

Carrier lifetimes. Because the presence of holes in the vicinity of the cathode barrier influences the feedback mechanism for avalanche breakdown, one would expect that decreasing the lifetimes would improve the critical voltage for cases in which the critical behavior is governed by avalanche breakdown. (By "lifetimes" we mean here the time constants τ_{n_0}, τ_{p_0} which enter our expression for SRH recombination through unintentional defects.) On the other hand, decreasing the lifetimes also corresponds to increasing the SRH generation rate for regions in which carriers are scarce—which increases the hole current available for avalanche multiplication and might tend to lower the critical voltage.

In Figure 7.4 we show the predicted effect of a 10-, 100-, or 1000-fold decrease in both τ_{n_0} and τ_{p_0} throughout the structure. Shorter lifetimes do indeed result in slightly higher critical voltages in the avalanche breakdown regime, so the dominant effect is that of reducing the hole population at the cathode. The results are generally insensitive to changes in the background carrier lifetimes, however, which is consistent with this recombination path
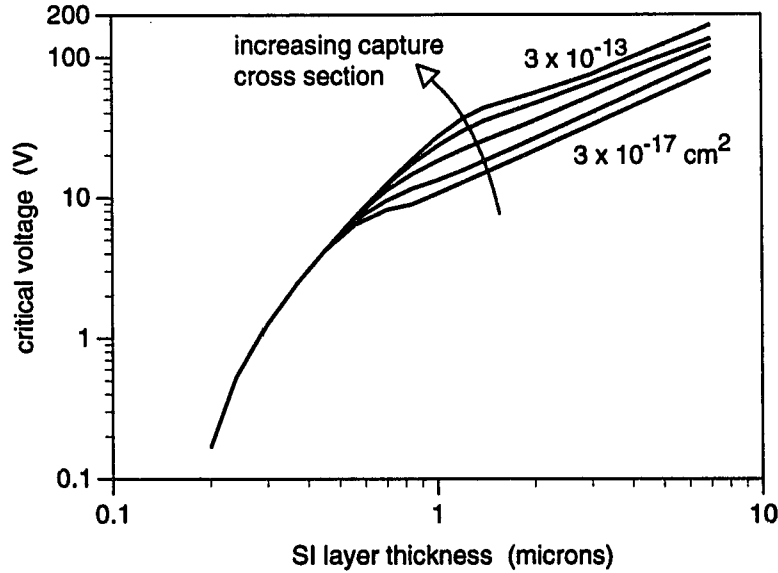
Figure 7.5:   Sensitivity of critical voltage to capture cross sections for SRH recombination through traps. Values of σ_{cn} are 3×10^{-17}, 3×10^{-16}, 3×10^{-15}, 3×10^{-14}, and 3×10^{-13} cm^2, with $\sigma_{cn}/\sigma_{cp} = 30$ in each case.

representing a small fraction of the total.

Capture cross sections. In the model, if we allow SRH recombination/generation through the traps, these processes outnumber those through the unintentional defects (for the background SRH lifetimes we have been assuming). Since the lifetimes which describe SRH processes through unintentional defects do affect the breakdown, we would expect that the capture cross sections which describe SRH processes through the traps would affect the breakdown as well.

In Figure 7.5 we show the predicted effect of increasing or decreasing the electron capture cross section σ_{cn} by one or two orders of magnitude, while holding $\sigma_{cn}/\sigma_{cp} = 30$. (As we have mentioned elsewhere, the results are insensitive to the value of σ_{cp} provided it is smaller than σ_{cn}.) Increasing the capture cross section corresponds to decreasing the lifetime for SRH recombination through the traps, which keeps down the hole population at the cathode
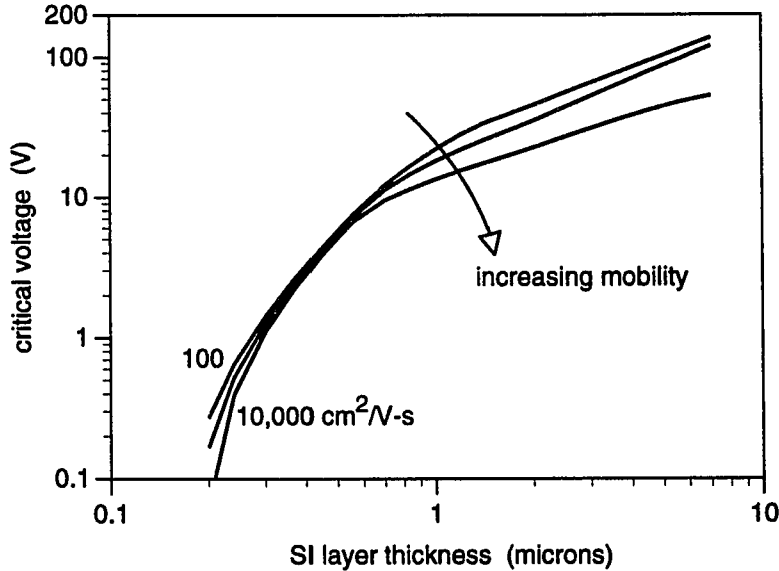
Figure 7.6: Sensitivity of critical voltage to low-field electron mobility. Values of μ_{n_0} are 100, 1000, and 10,000 cm^2/V-s, with $\mu_{n_0}/\mu_{p_0} = 5$ in each case.

and thus increases the avalanche breakdown voltage.

These results suggest that reducing the carrier lifetimes in the vicinity of the cathode would help to improve the critical voltage in the avalanche breakdown regime.

Mobility. In connection with our discussion in Section 6.4 of the discrepancy between the numerical and experimental results in the SCL regime, we mentioned the effect on the predicted critical voltage of raising or lowering μ_{n_0} from our value of 1000 cm^2/V-s. The effect of order-of-magnitude variations is shown in Figure 7.6. Note that these lines do not cross each other at the center; a decrease in the low-field mobility results in an improvement in the critical voltage in both the diffusion-limited and avalanche breakdown regimes.

In the diffusion-limited regime for thinner layers, in which velocity saturation is generally not an issue, a decrease in the mobility shows up as a proportional decrease in current across the entire J-V characteristic. Given the slope of the J-V curve in the TFL regime in the presence of diffusion from

the contacts, shifting the *J-V* curve down results in a larger critical voltage for any particular current criterion chosen.

For thicker layers, a decrease in the mobility increases the bias level at which velocity saturation becomes important. Recall from Chapter 4 that in the presence of velocity saturation the field profile is more nonuniform, so that the peak field is larger for a given applied voltage. Reducing the low-field mobility staves off this effect, and also reduces the current density for the same carrier population, so that the probability of impact ionization is reduced.

In the intermediate thickness range, for which the critical behavior is governed by trap filling due to injected carriers, the TFL regime of the *J-V* curve is steep and its position is determined by the concentration of initially empty traps—so changes in the low-field mobility have little effect on the critical voltage.

7.2 Design implications

For device design, the two properties of an SI layer over which one has the most control are the trap density N_t (through the Fe concentration) and the thickness L. The simplified theory gives a straightforward answer to the question of how the critical voltage depends on both: provided there are enough traps so that the critical voltage does not fall in the ohmic or SCL regime, the critical voltage is just the trap-filled limit (3.5), and increases linearly with $N_t - N_d$ and quadratically with L.

We have seen that the simplified theory fails to describe the experimental results. At both ends of the thickness range, the numerical model predicts— and experiment shows—a lower critical voltage than the simplified theory would predict.

In the previous section, we plotted numerical predictions for V_{cr} vs. L under various conditions, using log-log scales to show both sides of the thickness range. For device design, however, thin layers with low critical voltages are of less interest. In this section we focus on the behavior of thicker layers, for which trap filling by injected carriers and/or avalanche breakdown dominate. For the calculations in this section, we have used a larger contact doping than we did in the previous section (to more closely approximate the situation in a typical device), and a smaller background doping.

It is instructive to examine the dependence of V_{cr} on N_t and on L using a linear scale, and to contrast the predictions of the numerical model with

Figure 7.7: V_{cr} vs. N_t design curves for several thicknesses. $N_{dn} = 5 \times 10^{17}$ cm^{-3} in contacts; $N_d = 1 \times 10^{15}$ cm^{-3} in SI layer. Open circles indicate transition from reversible trap filling to destructive breakdown as predicted by numerical model.

those of the simplified theory. This we do in Figures 7.7 and 7.8. Because the simplified theory is well known, comparing the numerical results to the simplified trap-filled limit gives us a useful way to organize what we learn from the numerical model.

Figure 7.7 shows the dependence of critical voltage on trap density for several SI layer thicknesses. The thin straight lines show the trap-filled limit of the simplified theory; the dark lines show the prediction of the numerical model. (The construction of the numerical curves is further discussed in Appendix G.) The transition from reversible to destructive breakdown predicted by the numerical model is indicated by the open circles. So long as the critical voltage remains in the trap-filled-limited regime, increasing the trap density is an effective way to improve the critical voltage. In the avalanche breakdown regime, however, increasing the trap density is ineffective for improving the
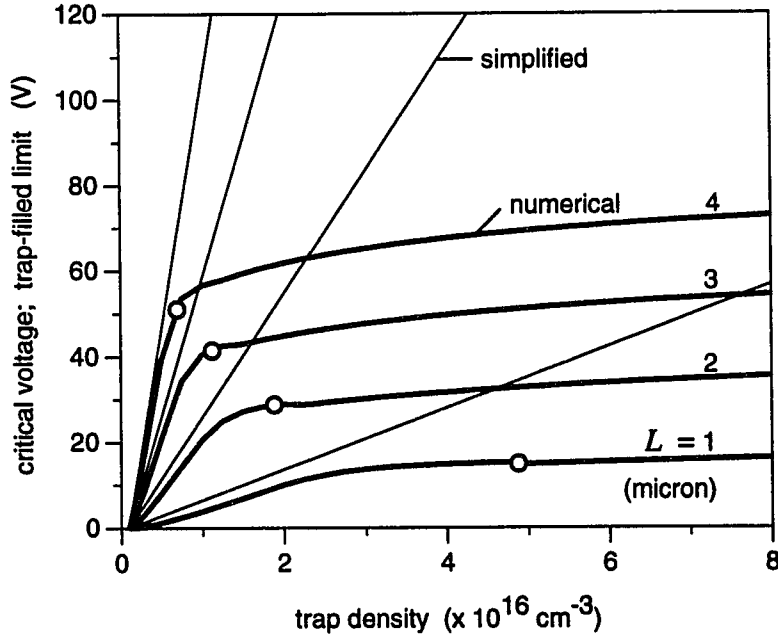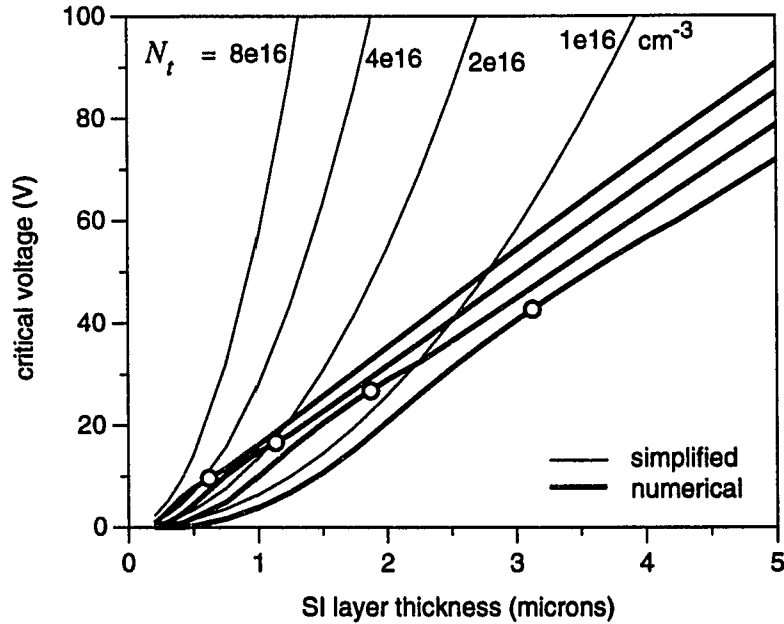
Figure 7.8: V_{cr} vs. L design curves for several trap densities. $N_{dn} = 5 \times 10^{17}$ cm^{-3} in contacts; $N_d = 1 \times 10^{15}$ cm^{-3} in SI layer. Open circles indicate transition from reversible trap filling to destructive breakdown as predicted by numerical model.

critical voltage.

That the critical voltage does not increase with the square of the SI layer thickness can also be seen clearly from Figure 7.7 and is shown explicitly in Figure 7.8. Here the thin parabolas show the trap-filled limit of the simplified theory and again the dark lines give the prediction of the numerical model. The critical voltage is approximately linear with increasing thickness in the avalanche breakdown regime, as we would expect for a field-related effect.

We can see that the quadratic-to-linear transition in V_{cr} vs. L corresponds to a transition from trap-filled-limited to avalanche-dominated behavior. The critical voltage follows either the trap-filled limit or the breakdown voltage, whichever is lower. If the traps fill before the breakdown voltage is reached, then the critical behavior is reversible and the critical voltage is roughly quadratic in the thickness. If the breakdown voltage is reached before the traps fill, then the critical behavior is irreversible and the critical voltage is

$$z = V_{cr} \quad (V)$$
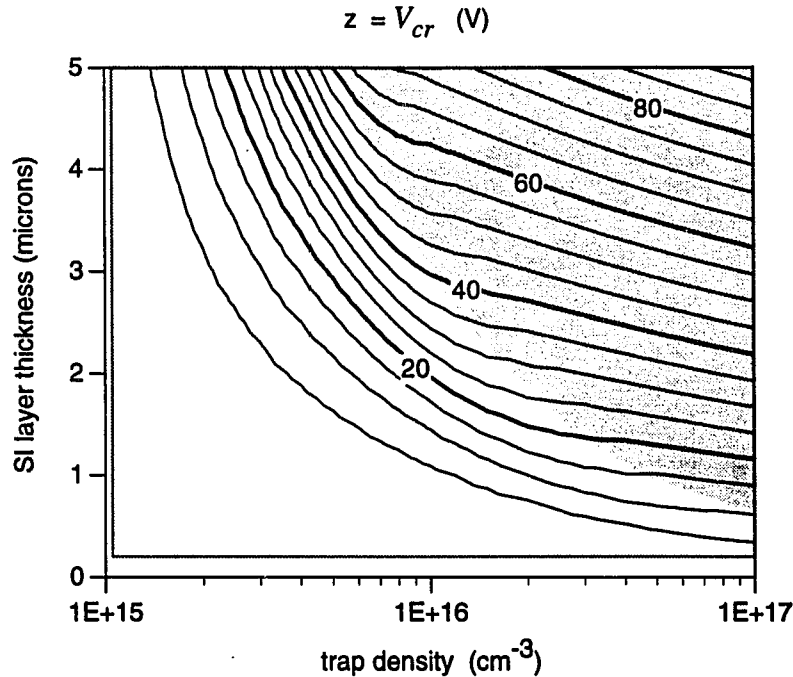
Figure 7.9: Contours of constant critical voltage V_{cr} as a function of trap density N_t and thickness L. $N_{dn} = 5 \times 10^{17}$ cm^{-3}; $N_d = 1 \times 10^{15}$ cm^{-3}. Critical behavior is reversible trap filling except in shaded region, where critical behavior is destructive breakdown resulting from avalanche injection.

roughly linear in the thickness.

We can summarize the predicted dependence of the critical voltage on SI layer thickness and trap density in the contour plot of Figure 7.9, where we show contours of constant V_{cr} in the N_t-L plane. The shaded region indicates the regime of destructive breakdown.

(In Figure 7.10 we divide the critical voltage V_{cr} by the SI layer thickness L to obtain an effective average critical field. That this field is not constant in the avalanche breakdown regime is a result of the spatial nonuniformity of the actual field distribution and of the fact that at these large biases a significant voltage drop occurs in the anode depletion layer.)

Figure 7.9 illustrates an important implication for device design. For high-reliability applications, a lower trap density or a thinner layer—with a
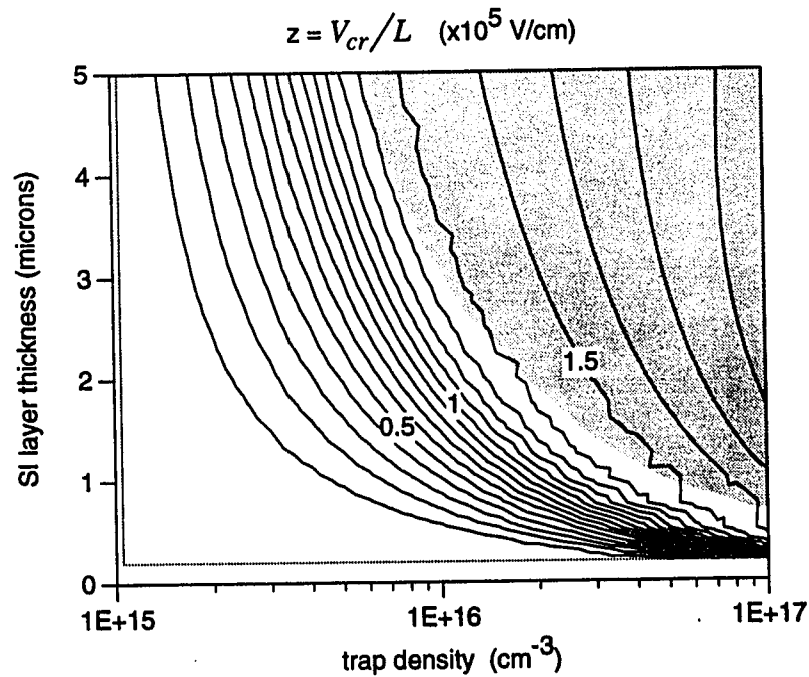
Figure 7.10: Contours of constant effective average critical field V_{cr}/L as a function of trap density N_t and thickness L. $N_{dn} = 5 \times 10^{17}$ cm^{-3}; $N_d = 1 \times 10^{15}$ cm^{-3}. Shaded region indicates avalanche breakdown.

corresponding performance reduction—may actually be preferable, so that in case of accidental application of a high voltage the trap-filled limit is reached before avalanche breakdown sets in. An electrostatic transient or misuse would thus result in a temporary, reversible current increase, rather than in destruction of the device.

Chapter 8

Conclusions and future directions

We have developed a numerical model for steady-state current injection in semi-insulating Fe:InP in a planar n-SI-n configuration. This model allows us to include mechanisms that are neglected in the traditional simplified theory, and to study the effects of these mechanisms on the progress of trap filling in the material and on the resulting J-V characteristics. It offers an explanation for the destructive breakdown that we have observed.

The critical voltages and the nature of the critical behavior predicted by the model are in good agreement with experiment. The model thus provides a basis for assessing the validity of the simplifying assumptions of the traditional theory, for extracting information about the material, and for predicting the performance of the material, as an aid to device and circuit design.

In this chapter we summarize the most important of the numerical results and then go on to suggest further work based on the beginnings we have made here.

8.1 Summary of numerical results

By comparing the predictions of the numerical model with those of the simplified theory, we can judge the validity of the simplifying assumptions which underlie the latter. The simplified theory, which was reviewed in Chapter 3, assumes that the behavior of the material is governed by injected electrons alone. Using the numerical model, we showed in Chapter 4 that for thin layers or low trap densities, diffusion of electrons from n-contacts fills a significant

portion of the traps at zero bias and thus leads to critical voltages much lower than the simplified theory would predict. On the other hand, we showed in Chapter 5 that for thick layers or high trap densities, avalanche injection can cause irreversible breakdown while most of the traps remain empty, so that again the critical voltages are much lower than those predicted by the simplified theory. Furthermore, we found that for trap densities large enough to be useful for device work, there is essentially no intermediate thickness range over which the simplified theory gives a good estimate of the critical voltage. For thin layers, diffusion from the contacts dominates. As soon as the layer becomes thick enough to minimize the effect of the interfaces, however, it is also thick enough that impact ionization becomes significant below the trap-filled limit.

Comparing the predictions of the numerical model with those of the simplified theory thus provides a useful way of classifying the various regimes of operation described by the numerical model.

In Figure 8.1 we show contours of constant V_{cr}/V_{TFL} in the N_t-L plane. That is, we plot the critical voltage predicted by the numerical model as a fraction of the trap-filled limit from the simplified theory. In the area labeled I, the critical voltage is lower than the simple trap-filled limit because diffusion from the contacts is significant. Carrier generation can be neglected, and the critical behavior is due to trap filling, but the drift-only asssumption of the simplified theory fails. In the area labeled III, the critical voltage is lower than the trap-filled limit because impact ionization is significant. The critical behavior is destructive breakdown due to avalanche injection, and the no-generation assumption of the simplified theory fails. Only in the intermediate area labeled II does the critical voltage approach the simple trap-filled limit. Only in this area is the simplified theory a good approximation, and only here is the critical behavior well described as trap filling by injected electrons.

Because the critical behavior in area III is due to avalanche breakdown rather than to trap filling, measures designed to increase the trap-filled limit (such as increasing the trap density) are ineffective for improving the performance in this regime. The improvement in breakdown voltage due to an increase in thickness will be much smaller than would be predicted for the trap-filled limit. Depending on load conditions and heatsinking, for high-reliability applications it may be desirable to design for lower trap densities and/or thinner layers so as to avoid the avalanche breakdown regime altogether.

In both the diffusion-limited and avalanche breakdown regimes, the nature of the contacts is important. The I-V characteristics of an n-SI-n structure
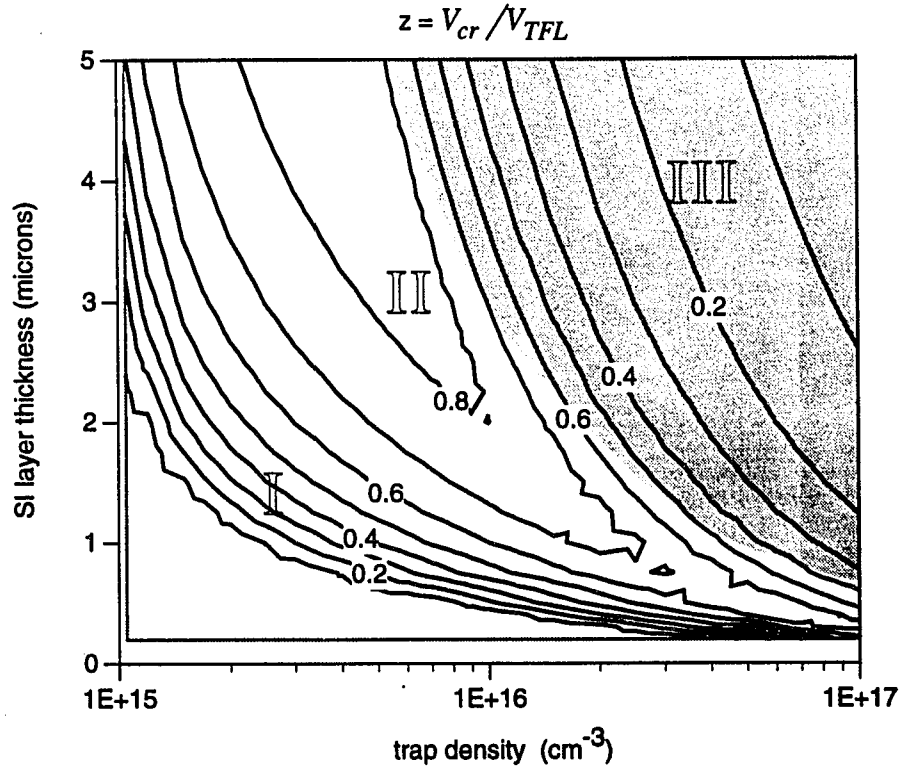
Figure 8.1: Ratio of critical voltage V_{cr} to simplified trap-filled limit V_{TFL} as a function of trap density N_t and SI layer thickness L. $N_{dn} = 5 \times 10^{17}$ cm^{-3}; $N_{dp} = 1 \times 10^{15}$ cm^{-3}. Shaded region indicates avalanche breakdown.

must be seen as properties of the structure as a whole rather than of the SI layer alone.

Finally, if an n-SI-n structure is used in order to avoid double injection in Fe:InP, one should remember that at high bias similar problems may arise due to avalanche injection of holes. From the point of view of recombination in the SI layer, the signature of double injection, it matters little whether the holes are injected from a forward-biased SI-p junction, diffuse across a too-thin n-layer in an SI-n-p anode, or are generated by impact ionization in the high-field region of an n-SI-n structure.

8.2   Suggestions for further work

Verification of model. In Chapter 6 we relied on room-temperature *I-V* characteristics for the comparison of theory with experiment. To further verify the model, it would help to have more direct evidence of impact ionization. Radiative recombination would be a good indication, but our calculations in Chapter 5 indicate that for the magnitude of the capture cross sections we are using, only a small amount of radiative recombination will be present at breakdown.

Manfred Pilkuhn has suggested looking for an enhancement in the noise just below breakdown as a means of verifying the presence of impact ionization. Predicting and measuring the temperature dependence of the *I-V* characteristics would also be instructive.

Ideally, for comparing theory and experiment we would like to have a good independent measure of the trap density. DLTS or simple *C-V* measurements on co-doped samples offer this possibility. If a lighter than optimal co-doping is needed in order to be able to deplete the sample, the model itself may be of help for the resulting analysis, since we can predict the exact shape of the depletion edges in the presence of deep levels.

(Static *C-V* measurements would be interesting as well. Because of charge transfer from the anode to the cathode space-charge layer, we predict that the static capacitance for an n-SI-n structure should approach zero at low bias.)

The velocity-field characteristics we have used in the model are questionable. Experimental data [45] for InP show the peak velocity occurring at slightly lower field than we have assumed. A modified $v(E)$ curve should be used in the next round of calculations.

Furthermore, in comparing the model with the experiments, we found that very low electron mobility could be used to explain the results. Further work is needed to determine if this is warranted or not. An independent measure of the mobility would be very helpful. Lampert and Mark [1] suggest a time-of-flight technique; John Bowers has suggested Hall measurement of a co-doped sample. (If further calculations and/or measurements continue to point to an extremely small low-field mobility, then work will be needed to identify the reason for it. If on the other hand the assumption of a low mobility is unjustified, then we continue to have a discrepancy in the shape of the *I-V* curve which suggests that other mechanisms may be operating.)

Our comparison of theory and experiment has assumed that both pertain to the same structure, namely a symmetric planar n-SI-n structure with abrupt

junctions operating in steady state. This means that we are assuming we can neglect geometric and surface-state effects along the edges of our mesas, and that we are idealizing the doping profiles. Further work to examine the validity of these assumptions is in order. We have looked at the current as a function of the diameter of our mesas, and sometimes (although not for the results shown in Chapter 6) see a dependence which is more nearly linear than quadratic—suggesting a significant contribution from surface current. Different methods of surface preparation give very different results, so for the most reliable comparison with theory, every effort should be made to passivate the surface. It would be good to see how the deposition of a silicon nitride layer would affect the I-V characteristics. Gottfried Döhler has suggested the use of guard rings to minimize surface conduction.

Since SIMS measurements indicate doping nonuniformities, we can put nonuniform doping into the model to see how much of an effect is attributable to this.

A variety of interesting results, involving hysteresis, polarity dependence, and nonreproducibility, remains to be accounted for. Because of the difference in behavior as a result of different final etches, we believe that many of these may be attributable to the surface.

Improvements in the model. Having convinced ourselves of the validity of the comparison, we can then explore other mechanisms that might account for any remaining discrepancy between the model and the experiments. Impact ionization into and out of the traps is a good candidate here. Ionization into the traps, in particular, could be expected to lower the avalanche breakdown voltage, since it creates holes.

Since we have not discussed the mechanics of the implementation here, we will simply state for the record that future work could profitably include the implementation of a better user interface and of a more robust solution technique. A systematic method for obtaining solutions on the negative-differential-resistance branch of the J-V characteristic would also be helpful. (A current-control version of the program has been implemented, and appears to be more stable—in the cases for which it works—than is the voltage-control version. However, the current-control version does not converge when empty traps are present. It fails precisely for those situations in which one wants to use it.) An obvious next step (obviously desirable, that is) is the implementation of a time-dependent solution. The results of the present model can be used as bias points for a small-signal analysis.

Use of model for characterization. Being able to predict the electrical characteristics as a function of materials parameters offers the possibility of using the model in conjunction with I-V measurements as a characterization tool. The extraction of doping information from the SCL portion of the I-V curve has been explored in the past [46, 47, 48]. This technique is based on multiple derivatives of the I-V curve and is derived in the context of the simplified theory; the present model gives us a means of evaluating its accuracy. As with the analysis of Chapter 3, it is not possible by this method to separate the mobility from the degeneracy.

As we mentioned in Chapter 6, in the course of our experiments we uncovered several growth nonuniformities. Mapping trap-filled limits on a moderately doped sample may prove a sensitive technique for exploring variations in background doping.

To the extent that materials parameters can be deduced from I-V measurements, the model can be an aid for process optimization. Knowing the nature of the planar I-V characteristics also provides a basis for the identification of other effects, such as leakage or recombination at regrown interfaces.

Use of model for design. With a verified model, one can also explore various schemes for improving the current-blocking capability of structures containing Fe:InP. For example, in a typical p-n-SI-n structure in which the total thickness of the middle two layers is dictated by processing considerations, what is the optimum division of that thickness between the n and SI layers? The present model can be used to answer this question if the doping levels in the various materials are known.

In Chapter 7 we have already explored the effects that would result from increasing the trap density or the layer thickness. We also predicted that increasing the capture cross sections and thereby reducing the carrier lifetimes would improve the avalanche breakdown voltage. In general, the model could be used to define the properties of an "ideal" trap for a given application, or to predict the performance for known traps. Conversely, because it relates the electrical performance of the material to the properties of the traps, the model could aid in the study of those properties for new traps.

The use of Ti (which provides a deep donor hole trap in InP) as a co-dopant with Fe has already been studied experimentally [34]. The co-doped material was found to have excellent thermal stability, and its electrical properties are promising. The present model could be easily extended to include this type of center, and could thus be used to predict the electrical performance of the

co-doped material under a variety of injection conditions.

The presence of Ti was also found to inhibit the interdiffusion of Fe with *p*-dopants [34]. The possibility of a thermally stable shallow acceptor adjacent to an Fe-InP layer is interesting, as it could provide a way to improve the performance of a thin SI layer in an *n*-SI-*n* structure. A sheet of fully-ionized acceptors at each interface would reduce the bandbending in the SI layer and thereby increase the number of initially empty traps available for current blocking. Our calculations indicate that this would indeed improve the performance for thin layers. The trouble with this scheme, apart from the stability of the δ-doping, is that the magnitude of the sheet charge must be controlled very accurately.

It has recently been proposed that the addition of narrow-bandgap recombination layers would help to reduce double injection in SI materials. Although the present model does not include heterojunctions, the performance of this type of structure could be modeled by artificially increasing the recombination rate in a particular layer. Since the presence of holes near the cathode contributes to lower breakdown voltages in *n*-SI-*n* structures, one approach to performance improvement (and also to further verification of the feedback mechanism proposed here) would be to suck these holes out through a lateral contact. This was suggested by Steve Koester, in analogy to the work of Bobby Brar. By introducing a "sink" term in our one-dimensional model, we could get an idea of what sort of improvement to expect from this two-dimensional effect, if a suitable contacting scheme could be devised.

Use of model for other materials, other structures. The model can of course be applied more generally, to the study of other materials besides SI InP. For example, it could be used to help with the identification of the traps in GaN, or to study the performance of low-temperature (LT) GaAs, or to examine the effects of interface charge at fused junctions. It has already been used to design and to predict the behavior of an APD.

To make the model a more generally useful design tool, we would want to add the capability of handling heterojunctions, non-local effects such as tunneling through barriers, time dependence, energy conservation, and 2-D or 3-D current flow. These are no longer additions to the present model, but rather revisions of the overall organization and philosophy of the model. Several commercial programs of this type already exist. In this context, the principal

value of the present work is in identifying the physical phenomena that must be included in such a model, if it is to accurately predict the performance of structures involving SI Fe:InP.

As InP technology progresses, design problems such as back- and side-gating, which have already been studied extensively in other materials, will arise. We can look to previous modeling work connected with more mature technologies—such as those of GaAs and silicon—as a guide to the development of good models. Simple models like the ones presented here can be used in conjunction with simple test structures to identify dominant mechanisms for inclusion in more complex models.

Appendix A

Constants and materials parameters

Values of various constants used for the calculations are listed in Tables A.1–A.3. The values shown in Table A.1 are taken from (or derived from the values given in) Kittel and Kroemer [49]. The properties of InP shown in Table A.2 are taken from Tiwari [50] unless otherwise noted. Derivative quantities are calculated from the other constants as follows:

$$N_{(C,V)} = \frac{1}{\sqrt{2}} \left(\frac{m_{(e,h)} kT}{\pi \hbar^2} \right)^{3/2} \tag{A.1}$$

$$\xi_C - \xi_i = (\xi_C - \xi_V)/2 - (kT/2) \ln(N_V/N_C) \tag{A.2}$$

$$n_i = N_C \exp[-(\xi_C - \xi_i)/kT] \tag{A.3}$$

$$v_{th_{(n,p)}} = \left(\frac{8kT}{\pi m_{(e,h)}} \right)^{1/2} \tag{A.4}$$

where for the thermal velocities we have used $v_{th} \equiv \bar{v} = \langle |v| \rangle$.

The constants describing the velocity-field relations as used in Chapters 4 and 5 are taken from an eyeball fit to the data of Sadra et al. [36], using the functional forms shown in Section 4.3. The calculations of Chapters 6–8 use a smaller low-field mobility, which was inferred from fitting our experimental data.

The impact ionization coefficients shown in Table A.2 are fits to the data of Cook et al. [41] as given by Capasso [42] for the range 3.6–5.6 × 10^5 V/cm. (Another fit to the same data is given by Wang [43].) A more accurate approach, short of treating the nonequilibrium distribution function correctly,

Table A.1: Values of universal constants used in the calculations.

c	2.998×10^{10}	cm/s
$\hbar c$	1.973×10^{-5}	eV-cm
$m_0 c^2$	0.511	MeV
q	1.602×10^{-19}	C
ϵ_0	8.854×10^{-14}	F/cm
kT at 300 K	0.02585	eV

would be to use a piecewise fit for these coefficients. Also note that the model for impact ionization used here is strictly local; that is, the generation rate at any position depends only on the field (and current density) at that position. In reality, however, an electron acquires energy from the field over a finite distance, so in the presence of a nonuniform field our model may overestimate the ionization rate.

The values used for various characteristics of Fe in InP are listed in Table A.3. The quantity n_1 is derived from the ionization energy $\xi_C - \xi_t$ according to

$$n_1 \equiv N_C \exp[-(\xi_C - \xi_t)/kT] \, . \tag{A.5}$$

There is much literature regarding the value of $\xi_C - \xi_t$. The energy levels of the trap have been studied by a number of experimental techniques, including thermal activation [5, 16], optical absorption [5, 15, 51], photoluminescence [15, 51], DC photoconductivity [16, 17, 52], AC photoconductivity [17], photocapacitance [51], DLTS [32, 51], calorimetric absorption spectroscopy [20], and FTIR absorption [18]. The reported ionization energies range from 0.59 eV [51, by DLTS] to 0.68 ± 0.02 eV [5, by thermal activation].

Naive analysis of Arrhenius plots of our own temperature-dependent I-V data gives an activation energy of 0.59–0.66 eV. However, this analysis is based on the assumption that $I \propto J \propto n_0 \propto \exp[-(\xi_C - \xi_t)/kT]$ only; the temperature dependence of the mobilities and that of the effective density of states, among other possibilities, are ignored. One can show analytically that ignoring the $T^{3/2}$ dependence of the density of states leads to an overestimation of the ionization energy by an amount $\frac{3}{2}kT$. That is, if $n_0 \propto (kT)^{3/2} \exp(-\Delta\xi/kT)$,

Table A.2: Properties of InP at 300 K as used in the calculations. For meaning of symbols, see list following table of contents.

$\xi_C - \xi_V$	1.35	eV
ϵ/ϵ_0	12.6	
m_e/m_0	0.077	
m_h/m_0	0.64	
τ_{no}, τ_{po}	10^{-7}	s

FOR VELOCITY-FIELD RELATIONS:

μ_{no}	1000–2000	cm^2/V-s
μ_{po}	200–400	cm^2/V-s
v_{sn}	1×10^7	cm/s
v_{sp}	8×10^6	cm/s
E_0	1.5×10^4	V/cm

FOR IMPACT IONIZATION:

α_{0_n}	3.48×10^6	cm^{-1}
α_{0_p}	2.64×10^6	cm^{-1}
E_{0_n}	2.76×10^6	V/cm
E_{0_p}	2.40×10^6	V/cm

DERIVATIVE QUANTITIES:

N_c	5.36×10^{17}	cm^{-3}
N_v	1.29×10^{19}	cm^{-3}
$\xi_C - \xi_i$	0.634	eV
n_i	1.20×10^7	cm^{-3}
v_{th_n}	3.88×10^7	cm/s
v_{th_p}	1.35×10^7	cm/s

Table A.3: Properties of Fe in InP at 300 K as used in the calculations.

$\xi_C - \xi_t$	0.59	eV
g	0.45	
n_1	7×10^7	cm^{-3}
σ_{cn}	3×10^{-15}	cm^2
σ_{cp}	1×10^{-16}	cm^2

then

$$\frac{d(\ln n_o)}{d(1/kT)} = -(\Delta\xi + \tfrac{3}{2}kT) .$$

(A.6)

For our data, taken over the range 280–380 K, including this effect in the analysis would reduce the estimate of the activation energy by 0.04 eV to 0.55–0.62 eV. For the thermal activation energies cited in the literature, it is often not clear whether this has been taken into account or not. In addition, even for a pure electron trap the current density depends on other temperature-dependent quantities, such as the mobility. If the trap also acts as a recombination center, the interpretation is further complicated by the interaction with the valence band [40]. Therefore, we favor the spectroscopic evidence for the position of the levels.

As mentioned in Chapter 2, the ionization energy $\xi_C - \xi_t$ refers to the position of the lowest-energy state of the occupied acceptor, with respect to the conduction-band edge. Thonke and Pressel [18] deduce the position of this level as 802.8 ± 1.2 eV above the valence band edge at 4.2 K. Scaling the energy difference proportionally with the bandgap (for lack of a more informed approach) converts this to $\xi_C - \xi_t = 0.59$ eV at 300 K.

Confusion also exists with regard to the degeneracy factor g. As mentioned in Chapter 2, several values have appeared or been implied in the literature, but these tend to be assumptions based on shallow-acceptor behavior. The value $g = 2/5$ [33] derives from an approach similar to ours, using $g_0 = 2$ for the $^6A_1$ ground state of the ^6S ($S = 5/2$, $L = 0$) level of the $3d^5$ (unoccupied) configuration, and $g_1 = 5$ for the ^5E ground state of the ^5D ($S = 2$, $L = 2$) level of the $3d^6$ (occupied) configuration in a tetrahedral crystal field.

The value $g_0 = 2$ is consistent with electron spin resonance (ESR) mea-

surements, which show five unpaired d-electrons for the unoccupied acceptor [5, 15]. (Excited states of the neutral acceptor, involving a spin-flip transition to a $^4T_1$ state 0.5 eV above the ground state, have been reported [19]. Because 0.5 eV $\gg kT$ for the temperatures of interest, we can neglect these excited states in our occupation function. On the other hand, a splitting of 0.07 cm^{-1} (.009 meV) between the two $^6A_1$ levels has also been reported [19, citing [15]]. This splitting is small enough to be neglected at room temperature, but would become significant at lower temperatures—in which case the method of Appendix B should be extended to include the excited state of the unoccupied acceptor.)

The value $g_1 = 5$ may overestimate the effective degeneracy of the occupied acceptor, even at room temperature. Spectroscopic data have been interpreted as showing that the five-fold degeneracy of the ^5E states is lifted by spin-orbit and spin-spin interactions to give an average separation of 14 cm^{-1} (1.7 meV) [15] between the ^5E levels. If these levels have no further degeneracy, we can apply the results of Appendix B with $g_1 = g_2 = g_3 = g_4 = g_5 = 1$. (The $^5T_2$ excited states are separated from the ground state by 0.35 eV, and thus can be neglected here.) Again using the data of Thonke and Pressel [18, Fig. 1], we find an effective degeneracy $g_1 = 4.4$ (rather than 5) for the occupied state at 300 K. Retaining $g_0 = 2$ for the unoccupied state, this gives us a degeneracy factor $g = g_0/g_1 = 0.45$ at 300 K.

Several values for the electron capture cross section have appeared in the literature: Look [16] extracted $\sigma_{cn} = 1 \times 10^{-15}$ cm^2 by fitting a model for the photoconductivity, using $\xi_C - \xi_t = 0.64$ eV and $g = 4$ in the analysis. Bremond et al. [32] found $3.5 \pm 1.9 \times 10^{-14}$ cm^2 by DLTS; Tapster et al. found 4×10^{-14} cm^2 [51]. Bremond et al. used $g = 1$ and also found an activation energy of 0.63 eV for the trap; in their formalism, this includes an activation energy for the capture cross section, which was not determined separately.

In their modeling work [26], Asada et al. used $\sigma_{cn} = 3 \times 10^{-15}$ cm^2, which they say agrees with their own DLTS measurements and with the reported values of Look [16], Fung et al. [17], and Bremond et al. [32]. For this work, we have retained Asada's value; in Chapter 7 we examine the sensitivity of the results to changes in it. In the presence of impact ionization, changes in the magnitude of the capture cross section can have a sizeable effect on the critical voltage we predict.

Asada et al. commented that no clearly determined values for the hole capture cross section had yet appeared in the literature. To our knowledge,

this is still the case. Asada *et al.* chose a tentative value of $\sigma_{cp} = 1 \times 10^{-16}$ cm^2 and found that their results were insensitive to σ_{cp} so long as it was much smaller than σ_{cn}. For the models discussed here, this is true as well, and we have retained $\sigma_{cp} = 1 \times 10^{-16}$ cm^2.

Appendix B

Occupation function for acceptor with excited state

In this work, we have used the usual occupation function for a single acceptor:

$$f^- = \frac{1}{1 + (g_0/g_1)\exp\left[-(\xi_F - \xi_t)/kT\right]}.$$
(B.1)

This occupation function is derived under the assumption that the acceptor has two states, unoccupied and occupied (by an electron). The degeneracies of the two states are g_0 for the unoccupied (unpaired, neutral) state, and g_1 for the occupied (paired, ionized) state. The ratio g_0/g_1 is the quantity that we have called the degeneracy factor g.

It has been reported that the Fe^{2+} occupied acceptor in InP exhibits excited states in the bandgap. In this section, we explore the effects of including such states in the occupation function for the trap.

For a deep acceptor whose occupied configuration has both a ground state and one excited state in the bandgap, there are three possible states, which we label 0, 1, 2 as shown in Table B.1. In this notation, ξ_0, ξ_1, and ξ_2 represent the total energy of the acceptor in its various states; ξ_{t_1} and ξ_{t_2} represent the energy of an electron in the ground state and excited state, respectively. The ionization energies $(\xi_C - \xi_{t_{(1,2)}})$ are ξ_{a1} from the ground state and ξ_{a2} from the excited state, so that $\xi_{a1} > \xi_{a2}$. Let's define $\Delta\xi_{a12} \equiv \xi_{t_2} - \xi_{t_1}$, the energy needed to lift the occupying electron out of the ground state into the excited state.

For our transport problem, so long as the electron is localized on the acceptor, it does not matter whether the electron is in the ground or excited state. In either case, the acceptor is ionized and carries a charge of $-q$, and the

state 0:	unoccupied	$N_0 = 0$
	unpaired	$g_0 = 2(?)$
		$\xi_0 = \xi_0$
state 1:	occupied, ground state	$N_1 = 1$
	paired	$g_1 = 1(?)$
		$\xi_1 = \xi_0 + \xi_{t_1}$
state 2:	occupied, excited state	$N_2 = 1$
	paired	$g_2 = 1(?)$
		$\xi_2 = \xi_0 + \xi_{t_2}$

Table B.1: Labeling of states for deep acceptor.

electron is unavailable for conduction. Thus the relevant occupation function is $f^- = f^1 + f^2 = P(1) + P(2)$.

Taking the Gibbs sums,

$$
\begin{aligned}
f^- &= f^1 + f^2 \\[2ex]
&= \frac{g_1 \exp[(\xi_F - \xi_1)/kT] + g_2 \exp[(\xi_F - \xi_2)/kT]}{g_0 \exp[-\xi_0/kT] + g_1 \exp[(\xi_F - \xi_1)/kT] + g_2 \exp[(\xi_F - \xi_2)/kT]} \\[2ex]
&= \frac{g_1 \exp[(\xi_F - \xi_{t_1})/kT] + g_2 \exp[(\xi_F - \xi_{t_1} - \Delta\xi_{a12})/kT]}{g_0 + g_1 \exp[(\xi_F - \xi_{t_1})/kT] + g_2 \exp[(\xi_F - \xi_{t_1} - \Delta\xi_{a12})/kT]} \\[2ex]
&= \left[1 + \left(\frac{g_0}{g_1 + g_2 \exp(-\Delta\xi_{a12}/kT)}\right) \exp[-(\xi_F - \xi_{t_1})/kT]\right]^{-1} . \quad (\text{B.2})
\end{aligned}
$$

If $\Delta\xi_{a12} = 0$, the effect of including the "excited" state is to increase the degeneracy of the occupied acceptor from g_1 to $g_1 + g_2$. This has the effect of lowering the degeneracy factor from $g = g_0/g_1$ to $g' = g_0/(g_1 + g_2)$, which would be equivalent (for a given temperature) to shifting the energy level down by an amount $kT \ln(g/g') = kT \ln[(g_1 + g_2)/g_1] = kT \ln(1 + g_2/g_1)$. That

is, for a given free electron concentration ($=>\xi_{Fn}$), there would be a larger fraction of occupied traps if we decrease the degeneracy factor (increase the degeneracy of the occupied state, or add an excited state). (In our problem, this means decreasing $\theta \sim gn_1/N_t$, which implies less current flow at a given injection level.) In the limit $\Delta\xi_{a12} \to \infty$, the occupation function returns to the single-level expression, as if the excited state were not there.

In the general case, including an excited state for the occupied acceptor with degeneracy g_2 and energy $\Delta\xi_{a12}$ above the ground state is equivalent (for a given temperature) to reducing the degeneracy factor by

$$\frac{g_0}{g_1} \to \frac{g_0}{g_1 + g_2 \exp(-\Delta\xi_{a12}/kT)} \tag{B.3}$$

or lowering the energy of the single-level acceptor by

$$\xi_{a1} \to \xi_{a1} - kT \ln\left[1 + (g_2/g_1)\exp(-\Delta\xi_{a12}/kT)\right] . \tag{B.4}$$

The reduction in the degeneracy factor is temperature-dependent. If kT is small compared to $\Delta\xi_{a12}$, the degeneracy factor remains near the single-level value. On the other hand, if kT is large compared to $\Delta\xi_{a12}$, then the degeneracy factor approaches $g_0/(g_1 + g_2)$. (For the transport problem, recall that the current density in the ohmic and SCL regimes is proportional to g. Other things being equal, therefore, the decrease in the degeneracy factor with increasing temperature would lead to a decrease in current density. But the current density is also proportional to n_1, which increases with temperature. The temperature dependence through n_1 is stronger than that through g, so for the overall problem the temperature dependence of g is more than offset by that of n_1.)

For an acceptor whose occupied configuration exhibits M excited states labeled $i = 2, 3, \ldots, M+1$, each with degeneracy g_i and separated from the ground state by an energy $\Delta\xi_{a1i}$, the degeneracy factor becomes

$$g = \frac{g_0}{g_1 + \sum_{i=2}^{M+1} g_i \exp(-\Delta\xi_{a1i}/kT)} . \tag{B.5}$$

In Appendix A we applied this result to the case of Fe in InP.

Appendix C

Parametric solution to the simplified problem

As noted in Chapter 3, the set of equations (3.9-3.12) describing the simplified problem for a single acceptor electron trap can be solved analytically for $V(J, E)$ and $x(J, E)$ [1]. Substituting (3.11) and (3.10) into (3.9) gives

$$\frac{dE}{dx} = -\frac{q}{\epsilon} \cdot \left[\left(\frac{J}{q\mu E} - n_0 \right) + \left(\frac{N_t}{1 + gn_1(q\mu E/J)} - n_{t_0} \right) \right] \equiv \mathcal{F}(J, E) . \quad \text{(C.1)}$$

The thermal carrier concentrations n_0 and n_{t_0} are constant, and are related by $n_{t_0} = N_t/(1 + gn_1/n_0)$. As shown in Section 3.2, (C.1) is integrated to yield

$$V(J, E) = \int \mathcal{F}^{-1}(J, E) E \, dE \quad \text{(C.2)}$$

$$x(J, E) = \int \mathcal{F}^{-1}(J, E) \, dE . \quad \text{(C.3)}$$

Lampert and Mark define the dimensionless variables

$$u \equiv \frac{qn_0\mu}{J} \cdot E(x) \quad \text{(C.4)}$$

$$v \equiv \frac{q^3 n_0^3 \mu^2}{\epsilon J^2} \cdot V(x) \quad \text{(C.5)}$$

$$w \equiv \frac{q^2 n_0^2 \mu}{\epsilon J} \cdot x . \quad \text{(C.6)}$$

Letting $E_0 = J/qn_0\mu$, the dimensionless field $u \equiv E(x)/E_0 = n_0/n(x)$ is the ratio of the actual local field $E(x)$ to that which would be present if the current were carried entirely by thermal free electrons. This quantity is the parameter for the solution.

In the dimensionless variables, (C.1) can be written as

$$\frac{du}{dw} = \frac{(1-u)(1+Gu)}{u(1+Cu)} \tag{C.7}$$

where, again using Lampert and Mark's definitions,

$$G \equiv C + D$$

$$D \equiv BC/(1+C)$$

$$C \equiv gn_1/n_0$$

$$B \equiv N_t/n_0 \ .$$

(For consistency with the rest of this document, we use here the symbol n_1 for the quantity that Lampert and Mark call N, and we use the symbol g for the quantity that Lampert and Mark would call $1/g$. Note, however, that B, C, D, G, R, and v as defined in this appendix have no relation to the quantities designated by those symbols elsewhere in this work.)

The parametric solution (C.2–C.3) is [1, Equations 4.113–4.114]

$$v = -\frac{C}{2G}u^2 - \left(R + \frac{S}{G}\right)u - R\ln(1-u) + \frac{S}{G^2}\ln(1+Gu) \tag{C.8}$$

$$w = -\frac{C}{G}u - R\ln(1-u) - \frac{S}{G}\ln(1+Gu) \tag{C.9}$$

where

$$R \equiv \frac{C+1}{G+1}$$

$$S \equiv \frac{D}{G(G+1)} \ .$$

Appendix D

Formulation of the numerical problem

The equations describing the numerical model were given in Section 4.1, with forms of additional terms given in Sections 4.2–4.4 and in Chapter 5 and in Appendix E. We have implemented a finite-difference solution, of which an overview is provided here. Greater detail can be found in the books by Kurata [24] and Selberherr [25].

Discretization of equations and formulation of matrix problem. A solution consists of three functions, $\psi(x)$, $n(x)$, and $p(x)$, that describe the spatial variation of the potential and of the carrier concentrations across the structure, and simultaneously satisfy the Poisson and continuity equations for all points in the structure. The technique in general is to assume that these have the forms $\psi_0(x) + \delta\psi(x)$, $n_0(x) + \delta n(x)$, and $p_0(x) + \delta p(x)$ where ψ_0, n_0, and p_0 are known, and then to locate zeroes of $\delta\psi$, δn, and δp as functions of ψ, n, and p. (I hope these symbols are not confusing; $n_0(x)$ here has nothing to do with the thermal concentration n_0 used elsewhere in this document— except that in starting from an equilibrium solution at zero bias we may use n_0 as our guess for n_0 when stepping up to the first non-zero bias point.) The solution is carried out by Newton's method, using analytic differentiation.

In the numerical version, the variables $\psi[i]$, $n[i]$, and $p[i]$ are defined on a mesh of M+1 "main" division points (let's label them $i = 1,2,3 \dots M+1$) that divides the structure into M cells. Derivatives of these variables are defined on a set of "auxiliary" points lying between the main points, at the centers of the cells. (Let's label these so that auxiliary point i lies between main division

points i and $i + 1$.) Most of the derivatives are formed in the obvious way, taking differences between values at the edges of a cell and dividing by the width of the cell.

We thus have a set of $3(M + 1)$ simultaneous equations: one Poisson and two continuity equations for each mesh point, plus the boundary conditions at the end points. The equations for the interior points $(2 \leq i \leq M)$ can be written in matrix form as follows:

$$A[i]\delta y[i - 1] + B[i]\delta y[i] + C[i]\delta y[i + 1] = F[i] . \qquad (D.1)$$

Here $A[i]$, $B[i]$, and $C[i]$ are 3×3 matrices, and $y[i]$, $\delta y[i]$, and $F[i]$ are 3×1 vectors. The elements of $\delta y[i]$ are $\delta p[i]$, $\delta n[i]$, $\delta \psi[i]$, and each of the rows of $A[i]$, $B[i]$, $C[i]$, and $F[i]$ corresponds to one of the original three equations. In our implementation, row 1 is the hole continuity equation, row 2 is electron continuity, and row 3 is Poisson. Thus the element $A_{12}[i]$ is the coefficient of $\delta n[i - 1]$ in the hole continuity equation for mesh point i, $B_{31}[i]$ is the coefficient of $\delta p[i]$ in the Poisson equation for mesh point i, and so on. These elements together form a $3(M - 1) \times 3(M - 1)$ block-tridiagonal matrix that can be inverted by standard algorithms, provided there are no singularities (see below).

The matrix elements are derived from the original equations by Taylor expansion to first order, substitution of discretized derivatives, and straightforward algebraic manipulation—with the following exception:

Scharfetter-Gummel integral forms for drift-diffusion equations. The drift-diffusion equations (4.4–4.5) relate the current densities to derivatives of the carrier concentrations and of the electrostatic potential. For the numerical problem, we need to relate each of the current densities at some auxiliary mesh point to the corresponding carrier concentration, and electrostatic potential, at the two adjacent main mesh points. The method of Scharfetter and Gummel [35] is an alternative to the "obvious" way of doing this, so as to avoid matrix singularities that would otherwise arise if the difference in potential between adjacent mesh points exceeds $2kT/q$. (Kurata [24] gives a good discussion of the problem; here we simply state the two methods and give the expressions to which they lead. For consistency with Kurata, we use as the example the equation for holes.)

For both the "obvious" method and the Scharfetter-Gummel method, the discretized hole current equation can be written as

$$J_p[i] = \lambda_{p_1}[i] \cdot p[i] + \lambda_{p_2}[i] \cdot p[i + 1] \qquad (D.2)$$

where $\lambda_{p_1}[i]$ and $\lambda_{p_2}[i]$ depend on $\beta[i] \equiv (q/kT)(\psi[i] - \psi[i+1])$. Using the "obvious" approach, we simply express $\partial p/\partial x$ and $\partial \psi/\partial x$ in difference form and plug those into (4.5). For the hole concentration in the drift term, we define the value of p at auxiliary point i by linear interpolation between the values at main points i and $i+1$. After some manipulation, we find from this "obvious" approach

$$\lambda_{p_1}[i] = (kT/q)\mu_p[i](\beta[i]/2 + 1) \qquad (D.3)$$

$$\lambda_{p_2}[i] = (kT/q)\mu_p[i](\beta[i]/2 - 1) . \qquad (D.4)$$

In the method of Scharfetter and Gummel, instead of taking differences immediately, we first use the drift-diffusion equation (4.5) to relate $p[i+1]$ to $p[i]$. This is done by assuming that J_p, μ_p, and $E = -\partial \psi/\partial x$ are constant across the width of cell i, then treating (4.5) as a differential equation for p and integrating to yield

$$p[i+1] = p[i]\exp(qEx/kT) + \frac{J_p}{q\mu_p E}(1 - \exp(qEx/kT)) . \qquad (D.5)$$

Only after this do we discretize $E = -\partial \psi/\partial x$, and rearrange to obtain

$$\lambda_{p_1}[i] = (kT/q)\mu_p[i]\frac{\beta[i]}{1 - \exp(-\beta[i])} \qquad (D.6)$$

$$\lambda_{p_2}[i] = (kT/q)\mu_p[i]\frac{\beta[i]}{1 - \exp(\beta[i])} . \qquad (D.7)$$

In the limit of small $\beta[i]$—that is, slow variation of the potential—these forms reduce to (D.3-D.4). Unlike (D.3-D.4), however, the integral forms can be used with more rapidly varying potentials. Use of the Scharfetter-Gummel expressions (D.6-D.7) therefore promotes computational efficiency by allowing the use of a sparser mesh than would be required with the simple difference forms (D.3-D.4).

For electrons, we have

$$J_n[i] = \lambda_{n_1}[i] \cdot n[i] + \lambda_{n_2}[i] \cdot n[i+1] \qquad (D.8)$$

$$\lambda_{n_1}[i] = (kT/q)\mu_n[i]\frac{\beta[i]}{1 - \exp(\beta[i])} \qquad (D.9)$$

$$\lambda_{n_2}[i] = (kT/q)\mu_n[i]\frac{\beta[i]}{1 - \exp(-\beta[i])} \qquad (D.10)$$

where, as before, $\beta[i] \equiv (q/kT)(\psi[i] - \psi[i+1])$.

Appendix E

Poole-Frenkel barrier-lowering for field emission

In Section 4.4 I showed the results of including field-enhanced emission from the traps, based on Poole-Frenkel barrier-lowering. This barrier-lowering was illustrated in Figure 4.10 for a one-dimensional Coulomb potential. For that case, the potential energy for an electron in the presence of a uniform electric field of magnitude E oriented along the $-z$ direction can be written as

$$\xi_{1D}(z) = \frac{-q^2}{4\pi\epsilon|z|} - qEz. \tag{E.1}$$

Here we have simply added the potential due to the applied field to that due to a positive point charge. (We have written z here rather than x, because we will want to use spherical coordinates below. The field would of course still be parallel to the direction of current flow, which was designated as x in the rest of this document.) The potential energy has a local maximum at $z = z_{max}$,

$$z_{max} = \left(\frac{q}{4\pi\epsilon E}\right)^{1/2}, \tag{E.2}$$

whence

$$\Delta\xi_{a_{1D}}(E) = -\xi_{1D}(z_{max}) = -q\left(\frac{qE}{\pi\epsilon}\right)^{1/2}. \tag{E.3}$$

Assuming that all of the emission occurs in the positive z direction results in an enhancement of the emission probability e_n by a factor $\exp[\Delta\xi_{a_{1D}}(E)/kT]$. Martin et al. [39] attribute this result to Frenkel and point out that it overestimates the field effect.

The one-dimensional Coulomb potential is a special case of the three-dimensional potential described by

$$\xi_{3D}(r) = \frac{-q^2}{4\pi\epsilon r} - qEr\cos\theta, \tag{E.4}$$

where r and θ are the usual spherical coordinates such that $r\cos\theta = z$. The radial position of the barrier and the change in the barrier height are now functions of θ, with $E\cos\theta$ replacing E in the expressions above. For the evaluation of the emission enhancement in this case, I relied on the work of Martin *et al.*, whose result [39, Equation 7] I have not checked. They assume that for the hemisphere in which the barrier is not lowered (as for $z < 0$ in Figure 4.10) the emission probability remains unchanged with respect to the zero-field case, and find that the overall emission probability is enhanced by a factor

$$\frac{e_{n3}}{e_{n0}} = \frac{1}{\gamma^2}[e^\gamma(\gamma - 1) + 1] + \frac{1}{2}, \tag{E.5}$$

where e_{n3} is the overall emission probability in the presence of the field, e_{n0} is the overall emission probability in the absence of the field, and

$$\gamma \equiv (qE/\pi\epsilon)^{1/2}q/kT. \tag{E.6}$$

In Section 4.4 I also showed what would happen if we assumed a three-dimensional square-well potential of radius $r_0 = 50$ Å. Here again I relied on the result shown by Martin *et al.* [39, Equation 9]:

$$\frac{e_{n3}}{e_{n0}} = \frac{1}{2\gamma}(e^\gamma - 1) + \frac{1}{2} \tag{E.7}$$

where

$$\gamma \equiv qEr_0/kT. \tag{E.8}$$

(Martin *et al.* use F to denote the field, and $\epsilon_r\epsilon_0$ to denote the permittivity. Their paper is about field emission from non-Coulombic traps; the results I have quoted are taken from their introductory overview.)

Our formulation (4.14) is equivalent to

$$\frac{e_{n3}}{e_{n0}} = \exp[\Delta\xi_a(E)/kT], \tag{E.9}$$

which means that, for the three-dimensional Coulomb and square-well potentials, the change in ionization energy $\Delta\xi_a(E)$ that enters (4.14) is an average obtained by equating (E.9) with (E.5) or (E.7) respectively. For the one-dimensional Coulomb potential, $\Delta\xi_a(E)$ in (4.14) is just $\Delta\xi_{a_{1D}}(E)$ from (E.3) above.

In Section 4.4 we saw the effect on the distribution of filled traps and on the J-V characteristics of assuming in turn each of these three forms for the potential due to the trap. In the presence of velocity saturation in the SCL regime, none of the three gives particularly good agreement with experiment for the shape of the J-V curve in that regime. Because of the redistribution of space charge as discussed in Section 4.4, all three forms would result in higher critical voltages than would be expected in the absence of field emission. (This effect is illustrated in Figure 6.1.) Of the forms considered, the 3-D Coulomb potential is in principle the most likely to correspond to the actual physics, but the assumption that it does is still fairly arbitrary. For these reasons, and because the convergence of the model is much worse with field emission than without it, and because we can achieve approximately the same effect on the critical voltage by simply assuming a linear velocity-field relationship, field emission was not included in the calculations for Figure 6.3 or in those for Chapters 7 and 8.

Appendix F

Carrier concentrations in a reverse-biased p-n junction

Textbooks typically plot the carrier concentrations in a reverse-biased p-n junction under the assumption that no generation or recombination occurs inside the depletion region. Such generation does occur, of course, and can lead to a substantial dark current. In this appendix we calculate the steady-state carrier concentration profiles for a reverse-biased junction in the presence of Shockley-Read-Hall carrier generation. The profiles exhibit plateaus which can be explained with a simple current-continuity argument. This analysis of the p-n junction also sheds light on the n-SI-n problem.

Carrier concentration profiles for a symmetric p-n junction operating at 10 V reverse bias are shown in Figure F.1. Here we have taken $N_a = N_d = 5 \times 10^{16}$ cm^{-3} and $\tau_{n_0} = \tau_{p_0} = 1 \times 10^{-10}$ s, and assumed constant electron and hole mobilities of 2000 and 400 cm^2/V-s respectively. For comparison, we also show the concentrations as they would be in the absence of carrier generation.

In the presence of SRH generation, plateaus appear in the carrier concentration profiles. The presence of these plateaus makes sense if we consider that, in steady state, any carriers generated inside the depletion region must be removed by a drift current. If the carrier concentrations are held at very low values, then $np \ll n_i^2$ and the generation rate is large; at the same time, since the carriers are scarce, only a small drift current can flow. Thus, if we started from a condition of no generation and then turned on the generation mechanism, carriers would accumulate in the depletion region until the populations were large enough to hold down the net generation rate to a value that could be balanced by the drift current.
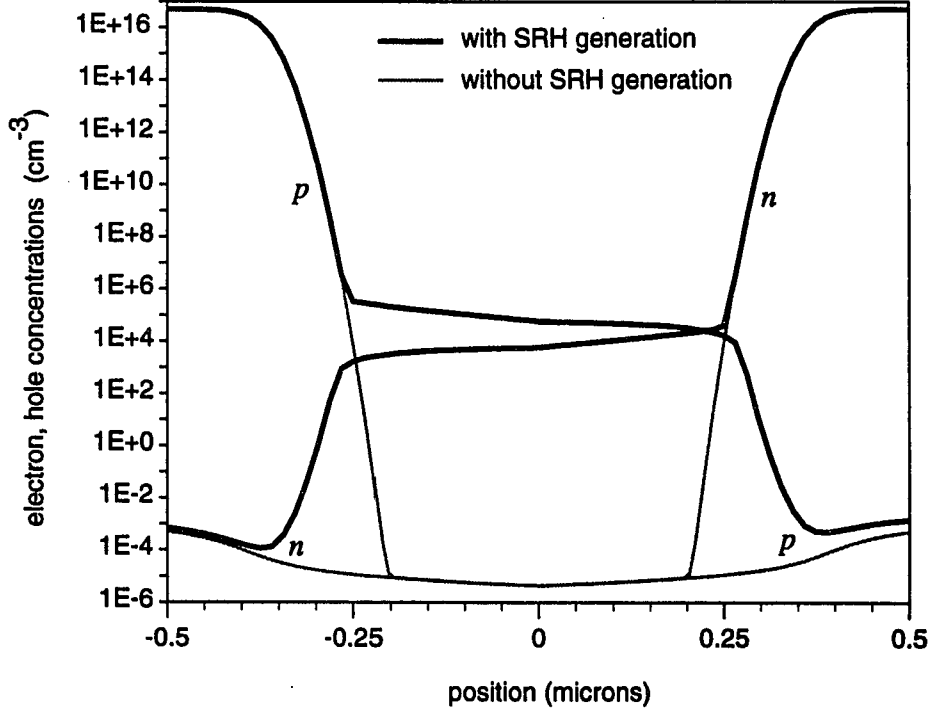
Figure F.1:   Carrier concentrations in a reverse-biased p-n junction, with and without SRH generation.

Since the carrier concentrations in the depletion region are small compared to the intrinsic concentration, we have

$$R_0 = \frac{np - n_i^2}{\tau_{p0}(n + n_i) + \tau_{n0}(p + n_i)} \approx -\frac{n_i}{2\tau} \tag{F.1}$$

if $\tau_{n0} = \tau_{p0} = \tau$. Thus the steady-state electron and hole current densities vary linearly across the depletion region, since (taking the electrons as the example)

$$\frac{1}{q}\frac{\partial J_n}{\partial x} = R - G = R_0 = -\frac{n_i}{2\tau} = \text{constant}. \tag{F.2}$$

For a symmetric junction of total depletion width W, in the plane of the junction we will have

$$J_n = -q\frac{W}{2} \cdot \frac{n_i}{2\tau} = qn\mu_n E_{max} \tag{F.3}$$

where we have neglected diffusion current on the grounds that the carrier concentrations are small. E_{max} is the field in the junction plane,

$$E_{max} = -\frac{qN_aW}{2\epsilon} \ ,$$ (F.4)

so that the electron concentration in the junction plane is

$$n = \frac{\epsilon}{qN_a\mu_n} \cdot \frac{n_i}{2\tau}$$ (F.5)

or 4.2×10^3 cm^{-3} for the case corresponding to Figure F.1. The numerical calculation yields 5.8×10^3 cm^{-3}.

Appendix G

Construction of design curves

In Chapters 7 and 8 are plots showing the critical voltage calculated in the numerical model, as a function of various parameters. This appendix shows in a bit more detail how those plots were constructed, and, we hope, addresses any confusion that might arise about what they mean. We use as examples one curve each from Figures 7.7 and 7.8.

The plots shown here will also give the reader an indication of the sensitivity of the design curves to the definition of the critical voltage. (Recall that in this work we have defined it as the voltage for which $J = 1 \text{ A/cm}^2$.)

Each curve in Figures 7.1–7.8 represents a family of J-V characteristics. For example, the $L = 2$ μm curve of Figure 7.7 condenses information from the family of J-V characteristics shown in Figure G.1. The curves in Figure G.1 differ from each other only in the trap density N_t used for the SI layer. For each trap density, the J-V curve is traced out by successively increasing the voltage, starting from a zero-bias solution of the Poisson equation. The critical voltage for each curve is the voltage at which it crosses the 1 A/cm^2 line, determined as follows:

For the lower trap densities (0.5 and 1×10^{16} cm^{-3} in Figure G.1), the trap-filled limit is encountered before avalanche breakdown can occur, and the calculation would trace out a smooth J-V characteristic through and beyond the steep section of the curve. This is a what we call reversible trap filling. For the construction of design curves, we stop the calculation as soon as the current density exceeds 1 A/cm^2, and use an external filter to determine the voltage at 1 A/cm^2 by linear interpolation.

For the higher trap densities (2.5×10^{16} cm^{-3} and above in Figure G.1), a larger voltage is required to fill the traps, and avalanche breakdown occurs before the trap-filled limit is reached. In these cases the full J-V characteristics
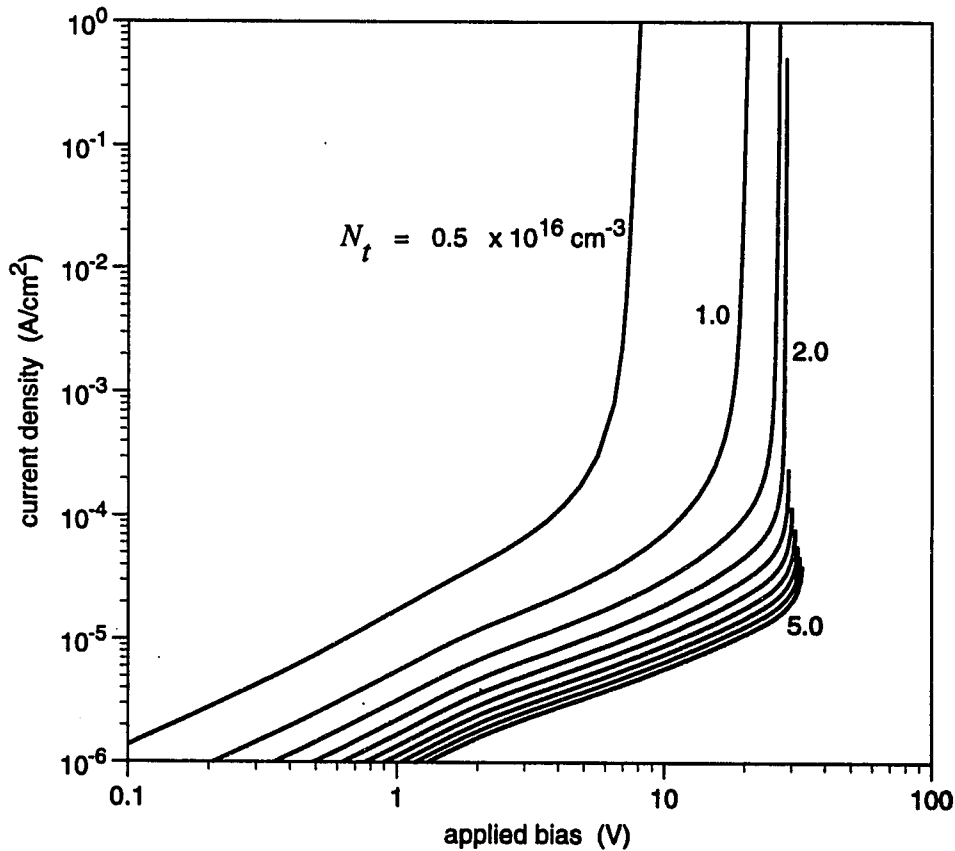
Figure G.1:   Numerical J-V characteristics for $L = 2$ μm, for trap densities from 0.5 to 5.0 $\times 10^{16}$ cm^{-3} in increments of 0.5 $\times 10^{16}$ cm^{-3}.

would exhibit the multiple-valued behavior shown in Figure 5.8. For Figure G.1 and for the construction of design curves, we have stopped the calculation at the turning point, and used the voltage at the turning point as the critical voltage—corresponding to what would be observed in voltage-controlled operation with a low-impedance source. This is indicated in Figure G.1 by curves that end below 1 A/cm^2, and constitutes a prediction of destructive breakdown.

For intermediate trap densities (1.5 and 2 $\times 10^{16}$ cm^{-3} in Figure G.1), we have a phenomenon that I call avalanche-assisted trap filling. Here the steep

portion of the curve is a result of trap filling at the anode side of the layer due to increased electron injection from a lowered barrier on the cathode side. That is, impact ionization produces holes which accumulate at the cathode side of the layer and thereby allow more electron injection—and thus more trap filling—for the same bias. Avalanche breakdown can still be reached at the top of the trap-filled regime, as illustrated by the $N_t = 2.0 \times 10^{16}$ cm^{-3} curve in Figure G.1. In these cases, stable operating points can (at least in principle) exist on a very steep section of the curve just below avalanche breakdown; here the prediction of reversible vs. destructive behavior is sensitive to the criterion chosen for the critical voltage.

For $N_t = 1.5 \times 10^{16}$ cm^{-3} or less (still for our 2-μm example), we predict reversible behavior up to 1 A/cm^2, while for $N_t = 2 \times 10^{16}$ cm^{-3} or more we predict destructive breakdown. The open circle on the 2-μm curve in Figure 7.7 is drawn between these two values of N_t, to indicate the transition from one type of behavior to the other. (In order to locate the transition more precisely, Figure 7.7 actually contains data points from more J-V curves than are shown in Figure G.1.)

All of the curves shown in Figures 7.1–7.8 were constructed in this way. As another example, we show in Figure G.2 the family of J-V characteristics whose critical voltages are summarized by the $N_t = 1 \times 10^{16}$ cm^{-3} curve of Figure 7.8. Note that we again have a regime of avalanche-assisted trap filling for intermediate thicknesses. In this case, for $L = 3$ μm or smaller we predict reversible behavior up to 1 A/cm^2, while for $L = 3.5$ μm or larger we predict destructive breakdown. Again, the open circle on the $N_t = 1 \times 10^{16}$ cm^{-3} curve of Figure 7.8 is drawn between these two values of L, to indicate the transition from one type of behavior to the other. One could of course also think of these transitions in terms of the critical voltages to which they correspond.
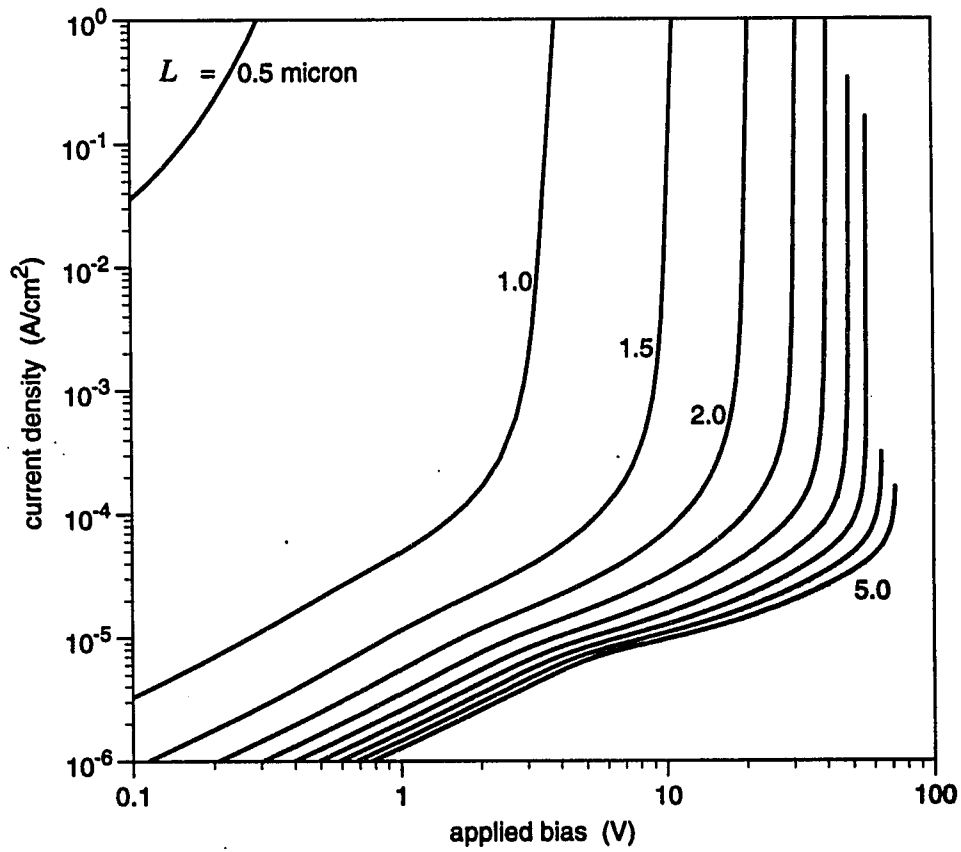
Figure G.2: Numerical J-V characteristics for $N_t = 1 \times 10^{16}$ cm^{-3}, for thicknesses from 0.5 to 5 μm in increments of 0.5 μm.

References

[1] M.A. Lampert and P. Mark. *Current Injection in Solids*. Academic Press, New York, 1970.

[2] U. Koren, T.L. Koch, P.J. Corvini, B.I. Miller, G. Eisenstein, R.S. Tucker, Y.K. Su, and R.J. Capik. High power high speed single mode SIPBH DFB lasers at 1.3 micron. *Journal of Applied Physics*, 64:4785, 1988.

[3] W.H. Cheng, C.B. Su, K.D. Buehring, C.P. Chien, J.W. Ure, D. Perracchione, D. Renner, K.L. Hess, and S.W. Zehr. Low-threshold 1.51 μm InGaAsP buried crescent injection lasers with semi-insulating current confinement layer. *Applied Physics Letters*, 49:1415, 1986.

[4] M.M. Hashemi, J.B. Shealy, P.J. Corvini, S.P. DenBaars, and U.K. Mishra. High performance InP JFETs grown by metalorganic chemical vapor deposition using tertiarybutylphosphine (TBP) as the phosphorus source. *Journal of Electronic Materials*, 23:233, 1994.

[5] G.K. Ippolitova, E.M. Omelyanovskii, N.M. Pavlov, A.Ya. Nashelskii, and S.V. Yakobson. Behavior of the Fe impurity in InP and influence of covalence on the ESR spectra of the Fe^{3+} ion in compounds with the T_d symmetry. *Sov. Phys. Semicond.*, 11:773, 1977.

[6] E.W.A. Young and G.M. Fontijn. Zinc-stimulated outdiffusion of iron in InP. *Applied Physics Letters*, 56:146, 1990.

[7] J. Cheng, S.R. Forrest, B. Tell, D. Wilt, B. Schwartz, and P.D. Wright. Semi-insulating properties of Fe-implanted InP. I. Current-limiting properties of n^+-semi-insulating-n^+ structures. *Journal of Applied Physics*, 58:1780, 1985.

[8] S. Lourdudoss, B. Hammarlund, and O. Kjebon. An investigation of hydride VPE growth and properties of semi-insulating InP:Fe. *Journal of Electronic Materials*, 19:981, 1990.

[9] J.A. Long, V.G. Riggs, and W.D. Johnston, Jr. Growth of Fe-doped semi-insulating InP by MOCVD. *Journal of Crystal Growth*, 69:10, 1984.

[10] K.L. Hess, S.W. Zehr, W.H. Cheng, and D. Perrachione. Semi-insulating InP grown by low pressure MOCVD. *Journal of Electronic Materials*, 16:127, 1987.

[11] K. Nakai, O. Ueda, T. Odagawa, T. Takanohashi, and S. Yamakoshi. Epitaxial growth and characterization of Fe-doped InP by MOCVD. In *Inst. Phys. Conf. Ser. No. 91*, 1988.

[12] R.T. Huang, A. Appelbaum, D. Renner, W. Burke, and S.W. Zehr. Growth and characterization of Fe-doped semi-insulating InP prepared by low-pressure organometallic vapor phase epitaxy with tertiarybutylphosphine. *Journal of Applied Physics*, 69:8139, 1991.

[13] P.J. Corvini, M.M. Hashemi, S.P. DenBaars, and J.E. Bowers. Fe-doped semi-insulating InP grown by atmospheric pressure MOCVD using tertiarybutylphosphine, trimethylindium, and ferrocene. Paper P4, Electronic Materials Conference, Boston, 1992.

[14] W.T. Tsang and J.D. Walker. Pentacarbonyliron doping for semi-insulating InP by chemical beam epitaxy. Paper WP24, Seventh International Conference on Indium Phosphide and Related Materials, 1995.

[15] W.H. Koschel, U. Kaufmann, and S.G. Bishop. Optical and ESR analysis of the Fe acceptor in InP. *Solid State Communications*, 21:1069, 1977.

[16] D.C. Look. Model for Fe^{2+} intracenter-induced photoconductivity in InP:Fe. *Physical Review B*, 20:4160, 1979.

[17] S. Fung, R.J. Nicholas, and R.A. Stradling. A study of the deep acceptor levels of iron in InP. *Journal of Physics C: Solid State Physics*, 12:5145, 1979.

[18] K. Thonke and K. Pressel. Charge-transfer transition of Fe ions in InP. *Physical Review B*, 44:13418, 1991.

[19] K. Pressel, G. Bohnert, A. Dornen, B. Kaufmann, J. Denzel, and K. Thonke. Optical study of spin-flip transitions at Fe^{2+} in InP. *Physical Review B*, 44:9411, 1993.

[20] A. Juhl, A. Hoffmann, D. Bimberg, and H.J. Schulz. Bound-exciton-related fine structure in charge transfer spectra of InP:Fe detected by calorimetric absorption spectroscopy. *Applied Physics Letters*, 50:1292, 1987.

[21] M. Sugawara, O. Aoki, N. Nakai, K. Tanaka, A. Yamaguchi, and K. Nakajima. I-V characteristics of semi-insulating InP epitaxial layers: Application to buried heterostructure lasers. In H. Kukimoto and S. Miyazawa, editors, *Semi-Insulating III-V Materials*, page 597, Tokyo, 1986. Ohmsha.

[22] T. Kitagawa, H. Hasegawa, and H. Ohno. Surface electrical breakdown and leakage current on semi-insulating InP. *Electronics Letters*, 21:299, 1985.

[23] K. Turki, G. Picoli, and J.E. Viallet. Behavior of InP:Fe under high electric field. *Journal of Applied Physics*, 73:8340, 1993.

[24] M. Kurata. *Numerical Analysis for Semiconductor Devices*. D.C. Heath and Co., Lexington, Massachusetts, 1982.

[25] S. Selberherr. *Analysis and Simulation of Semiconductor Devices*. Springer Verlag, Vienna, 1984.

[26] S. Asada, S. Suguo, K. Kasahara, and S. Kumashiro. Analysis of leakage current in buried heterostructure lasers with semiinsulating blocking layers. *IEEE Journal of Quantum Electronics*, 25:1362, 1989.

[27] K. Horio, T. Ikoma, and H. Yanai. Computer-aided analysis of GaAs n-i-n structures with a heavily compensated i-layer. *IEEE Transactions on Electron Devices*, ED-33:1242, 1986.

[28] K. Horio, H. Yanai, and T. Ikoma. Numerical simulation of GaAs MESFET's on the semi-insulating substrate compensated by deep traps. *IEEE Transactions on Electron Devices*, 35:1778, 1988.

[29] K. Horio and H. Yanai. The roles of junctions in conduction properties of GaAs n-i-n structures with a heavily compensated i-layer. In J.J.H.

Miller, editor, *Proceedings of the Seventh Annual International Conference on the Numerical Analysis of Semiconductor Devices and Integrated Circuits*, page 202, Boulder, 1991. Front Range Press.

[30] K. Horio and H. Kusuki. Effects of impact ionization on I-V characteristics of GaAs n-i-n structures including hole trap. *IEEE Electron Device Letters*, 13:541, 1992.

[31] N. Balkan, B.K. Ridley, and A.J. Vickers, editors. *Negative Differential Resistance and Instabilities in 2-D Semiconductors*. Plenum Press, New York, 1993.

[32] G. Bremond, A. Nouailhat, G. Guillot, and B. Cockayne. Deep level spectroscopy in InP:Fe. *Electronics Letters*, 17:55, 1981.

[33] A.M. Hennel. Energy level due to Fe in InP. In *Properties of Indium Phosphide*, page 157. INSPEC, The Institution of Electrical Engineers, London, 1991.

[34] T. Wolf, T. Zinke, A. Krost, H. Scheffler, H. Ullrich, D. Bimberg, and P. Harde. Fe- and Ti-doping of InP grown by metalorganic chemical vapor deposition for the fabrication of thermally stable high-resistivity layers. *Journal of Applied Physics*, 75:3870, 1994.

[35] D.L. Scharfetter and H.K. Gummel. Large-signal analysis of a silicon Read diode oscillator. *IEEE Transactions on Electron Devices*, ED-16:64, 1969.

[36] K. Sadra, C.M. Maziar, and B.G. Streetman. Electron-hole scattering and minority-electron transport in $In_{0.53}Ga_{0.47}As$, InAs, and InP: The role of the split-off band. First International Conference on Indium Phosphide and Related Materials, Norman, Oklahoma, 1989.

[37] A. Rose and M.A. Lampert. *Physical Review*, 113:1227, 1959 or *RCA Review*, 20:57, 1959.

[38] J.P. Ibbetson and U.K. Mishra. Space charge limited transport in non-stoichiometric GaAs—the role of velocity saturation. to be submitted to *Applied Physics Letters*, 1996.

[39] P.A. Martin, B.G. Streetman, and K. Hess. Electric field enhanced emission from non-Coulombic traps in semiconductors. *Journal of Applied Physics*, 52:7409, 1981.

[40] B. Srocka, H. Scheffler, and D. Bimberg. Fe^{2+}-Fe^{3+} level as a recombination center in $In_{0.53}Ga_{0.47}As$. *Physical Review B*, 49:10259, 1994.

[41] L.W. Cook, G.E. Bulman, and G.E. Stillman. Electron and hole impact ionization coefficients in InP determined by photomultiplication measurements. *Applied Physics Letters*, 40:589, 1982.

[42] F. Capasso. Physics of avalanche photodiodes. In W.T. Tsang, editor, *Semiconductors and Semimetals, Volume 22: Lightwave Communications Technology, Part D: Photodetectors*, page 95. Academic Press, Orlando, 1985.

[43] S. Wang. *Fundamentals of Semiconductor Theory and Device Physics*. Prentice Hall, Englewood Cliffs, New Jersey, 1989.

[44] H. Hasegawa, T. Kitagawa, T. Sawada, and H. Ohno. Surface electrical breakdown with white-light emission on semi-insulating GaAs substrates. *Electronics Letters*, 20:561, 1984.

[45] W. Fawcett and D.C. Herbert. High-field transport in indium phosphide. *Electronics letters*, 9:308, 1973.

[46] J.C. Pfister. Note on the interpretation of space charge limited currents with traps. *Phys. Stat. Sol. (a)*, 24:K15, 1974.

[47] C. Manfredotti, C. De Blasi, S. Galassini, G. Micocci, L. Ruggiero, and A. Tepore. Analysis of SCLC curves by a new direct method. *Phys. Stat. Sol. (a)*, 36:569, 1976.

[48] J.W. Roach and H.H. Wieder. Space-charge-limited currents and trapping in semi-insulating InP. *IEEE Electron Device Letters*, EDL-6:356, 1985.

[49] C. Kittel and H. Kroemer. *Thermal Physics*. W. H. Freeman and Company, San Francisco, second edition, 1980.

[50] S. Tiwari. *Compound Semiconductor Device Physics*. Academic Press, San Diego, 1992.

[51] P.R. Tapster, M.S. Skolnick, R.G. Humphreys, P.J. Dean, B. Cockayne, and W.R. MacEwan. Optical and capacitance spectroscopy of InP:Fe. *Journal of Physics C: Solid State Physics*, 14:5069, 1981.

[52] L. Eaves, A.W. Smith, P.J. Williams, B. Cockayne, and W.R. MacEwan. An energy scheme for interpreting deep-level photoconductivity and other recent optical measurement for Fe-doped InP. *Journal of Physics C: Solid State Physics*, 14:5063, 1981.